

2001

Measurement of Bottom Quark Production in Two-Photon Collisions.

Sepehr Saremi

Louisiana State University and Agricultural & Mechanical College

Follow this and additional works at: http://digitalcommons.lsu.edu/gradschool_disstheses

Recommended Citation

Saremi, Sepehr, "Measurement of Bottom Quark Production in Two -Photon Collisions." (2001). *LSU Historical Dissertations and Theses*. 433.

http://digitalcommons.lsu.edu/gradschool_disstheses/433

This Dissertation is brought to you for free and open access by the Graduate School at LSU Digital Commons. It has been accepted for inclusion in LSU Historical Dissertations and Theses by an authorized administrator of LSU Digital Commons. For more information, please contact gcoste1@lsu.edu.

INFORMATION TO USERS

This manuscript has been reproduced from the microfilm master. UMI films the text directly from the original or copy submitted. Thus, some thesis and dissertation copies are in typewriter face, while others may be from any type of computer printer.

The quality of this reproduction is dependent upon the quality of the copy submitted. Broken or indistinct print, colored or poor quality illustrations and photographs, print bleedthrough, substandard margins, and improper alignment can adversely affect reproduction.

In the unlikely event that the author did not send UMI a complete manuscript and there are missing pages, these will be noted. Also, if unauthorized copyright material had to be removed, a note will indicate the deletion.

Oversize materials (e.g., maps, drawings, charts) are reproduced by sectioning the original, beginning at the upper left-hand corner and continuing from left to right in equal sections with small overlaps.

Photographs included in the original manuscript have been reproduced xerographically in this copy. Higher quality 6" x 9" black and white photographic prints are available for any photographs or illustrations appearing in this copy for an additional charge. Contact UMI directly to order.

**ProQuest Information and Learning
300 North Zeeb Road, Ann Arbor, MI 48106-1346 USA
800-521-0600**

UMI[®]

**MEASUREMENT OF BOTTOM QUARK PRODUCTION IN
TWO-PHOTON COLLISIONS**

A Dissertation

**Submitted to the Graduate Faculty of the
Louisiana State University and
Agricultural and Mechanical College
in partial fulfillment of the
requirements for the degree of
Doctor of Philosophy**

in

The Department of Physics and Astronomy

by

Sepehr Saremi

B.S., Louisiana State University, 1995

M.S., Louisiana State University, 1997

December 2001

UMI Number: 3042649

UMI[®]

UMI Microform 3042649

**Copyright 2002 by ProQuest Information and Learning Company.
All rights reserved. This microform edition is protected against
unauthorized copying under Title 17, United States Code.**

**ProQuest Information and Learning Company
300 North Zeeb Road
P.O. Box 1346
Ann Arbor, MI 48106-1346**

*To my dear parents Fatemeh and Majid Saremi,
who have given me encouragement and support.*

ACKNOWLEDGEMENTS

I feel very indebted to my parents for the support that I have received from them throughout my education. As a child they always encouraged me to pursue the highest levels of knowledge. Their financial support for my education was by all means exceptional. I would not have reached this point without them.

At LSU, I was fortunate to meet my thesis advisor, Professor Roger McNeil. He provided me the opportunity to work on the L3 experiment at CERN and introduced me to the field of two-photon physics. It was a pleasure for me to work under his direction and I am grateful to him for his guidance. I would like to thank all of my other physics professors. Unfortunately I will not be able to name them one by one since the list will be long. However, I like to mention Professor William Metcalf, the chairman of the Physics and Astronomy department at LSU. I enjoyed Professor Metcalf's classes as an undergraduate and benefited from his support as a graduate student.

It was a great experience for me to work at CERN. Over there, I had the opportunity to work with many particle physicists. Most notable among them is Dr. Valery Andreev, LSU's post doctoral researcher at CERN. I spent a lot of time working with Dr. Andreev. He was very patient in guiding me and always helped me whenever I needed it. I do not know how to thank him. I also like to express my gratitude to Professor Maria Kienzle and Dr. John Field. I had valuable discussions with these individuals in our weekly two-photon analysis meeting. Their suggestions gave me useful insights regarding my research. In addition, I want to thank all my other

colleagues in the L3 collaboration. The L3 experiment was very successful as a result of the dedicated effort of many excellent physicists and technical staff members. I thank the spokesman, Professor Samuel C. C. Ting for his leadership of the 20 year long experiment.

Finally, I am grateful to all the family members and relatives who gave me emotional support and enthusiasm for reaching my goals. I would like to especially thank my sister and brother-in-law, Setareh and Ali, for the year that I spent with them in Los Angeles.

TABLE OF CONTENTS

ACKNOWLEDGEMENTS	iii
LIST OF TABLES	vii
LIST OF FIGURES	viii
ABSTRACT	xii
CHAPTER	
1 INTRODUCTION	1
1.1 Photon As A Particle	1
1.2 Two Photon Interactions	4
2 QCD AND HEAVY FLAVOR PRODUCTION	14
2.1 Quantum Chromodynamics	14
2.2 Two Photon Production In Storage Rings	18
2.3 QCD And Two Photon Interactions	19
2.4 Heavy Flavor Production In Two Photon Collisions	21
3 THE L3 DETECTOR AT LEP	29
3.1 LEP Collider	29
3.2 Particle Detectors At e^+e^- Colliders	33
3.3 L3 Detector	39
3.3.1 Time Expansion Chamber	42
3.3.2 Electromagnetic Calorimeter	44
3.3.3 Hadron Calorimeter	46
3.3.4 Muon Chamber	48
3.3.5 Luminosity Monitor	52
4 DATA AQUISITION AND SIMULATION	54
4.1 Trigger System	54
4.1.1 Level 1 Trigger	55
4.1.2 Level 2 Trigger	59
4.1.3 Level 3 Trigger	60
4.2 Event Reconstruction	60
4.2.1 Tracks In The TEC	61
4.2.2 Clusters In The Calorimeters	61
4.2.3 Muons In The MUCH	62
4.3 Monte Carlo Simulation	62
4.3.1 Event Generation	63
4.3.2 Detector Simulation	64
4.4 Final Data Structure	65
5 EVENT SELECTION	67
5.1 Hadronic Two-Photon Events	67
5.2 Electron Selection	75

5.3 Muon Selection	89
6 CROSS SECTION MEASUREMENT	99
6.1 Jet Reconstruction	99
6.2 Cross Section Calculation	101
6.2.1 Cut Based Method	101
6.2.2 Fit Based Method	106
6.3 Cross Section Using Electron Fit	108
6.4 Cross Section Using Muon Fit	109
6.5 Systematic Errors	111
6.6 Cut Based Cross Section	116
6.7 Consistency With Charm	118
6.8 Comparison With Theory	118
6.9 Prospects For Other Experiments	121
7 CONCLUSION AND OUTLOOK	125
7.1 The First Measurement Of $e^+e^- \rightarrow e^+e^-b\bar{b}X$	125
7.2 Next Linear Collider	128
7.3 Why Disagreement?	129
BIBLIOGRAPHY	132
APPENDIX A - ADDENDUM TO QCD	135
A.1 Altarelli-Parisi Equation	135
A.2 Splitting Functions	136
A.3 $\{\}_+$ Functions	136
APPENDIX B - SCINTILLATORS	138
B.1 Introduction	138
B.2 Barrel and Endcap Counters	138
B.3 Calibration	139
B.3.1 Calibration Events	139
B.3.2 Barrel	141
B.3.3 Endcap	144
B.4 Efficiency	146
THE L3 COLLABORATION	152
PUBLICATIONS	155
VITA	159

LIST OF TABLES

1.1	Properties of quarks	3
1.2	Properties of leptons	4
1.3	The mediating particles for different forces	4
5.1	Cuts for the electron selection	77
5.2	Cuts for the muon selection	93
6.1	Fit results for the electron tag	108
6.2	Fit results for the muon tag	109
6.3	Systematic uncertainties on $\sigma(e^+e^- \rightarrow e^+e^-b\bar{b}X)$ in percent .	116

LIST OF FIGURES

1.1	The photon fluctuation is depicted in this figure	2
1.2	Typical sizes for different particles	3
1.3	Kinematics of two photon interactions at an e^+e^- collider . .	5
1.4	Cross sections for several processes	8
1.5	The measured cross sections of heavy flavor production in two-photon interactions	10
1.6	The cross section of b quark production in γp interactions as a function of the invariant mass	11
1.7	The $D\theta$ results for b quark production	13
2.1	Two photon strong interactions proceed via three different general type of processes	22
2.2	The direct process and its corrections due to single gluon radiation	23
2.3	The total b quark production cross section as a function of the b quark mass and different values of the renormalization scale	27
2.4	The direct b quark production cross section as a function of the b quark mass for various renormalization schemes	28
3.1	A 3 dimensional view of the LEP accelerator	30
3.2	The different stages for accelerating electrons and positrons for the LEP accelerator	32
3.3	The $r - \phi$ view of the L3 detector	35
3.4	The 3 dimensional view of the L3 detector	39
3.5	The $y - z$ view of the L3 detector	40
3.6	Shower production in the BGO crystals and HC (Hadronic Calorimeter) module of the L3 detector	41
3.7	The 3 dimensional view of the TEC	43
3.8	One inner sector and two outer sectors of the TEC	44

3.9	The $\tau - \phi$ view of the central part of the L3 detector	45
3.10	The side view of a single BGO crystal	46
3.11	The 3 dimensional view of the HCAL	47
3.12	The 3 dimensional view of the muon chamber	49
3.13	The $x - y$ view of one octant of the muon chamber	50
3.14	Within each octant the five P chambers can be aligned through a laser beam	51
3.15	The forward backward muon chamber is mounted on the L3 magnet door	51
3.16	A typical Bhabha event in the luminosity monitor	53
4.1	The schematic view of the L3 trigger system	55
5.1	The Feynman diagram for a b quark semi-leptonic decay	69
5.2	The Feynman diagram for a c quark semi-leptonic decay	69
5.3	The comparison between data and Monte Carlo for the total visible energy	73
5.4	The comparison between data and Monte Carlo for the visible invariant mass, W_{vis}	74
5.5	The $N - 1$ plot of the ratio of the energy of the most energetic cluster in the luminosity monitor to the beam energy	76
5.6	The momentum distribution of the electron candidates start- ing from 0.6 GeV	78
5.7	The Monte Carlo distributions for the momentum of the elec- tron candidates	79
5.8	This plot shows the distributions of the ratio of the transverse energy of the electron (in ECAL) to its transverse momentum (in TEC)	81
5.9	The polar angular distribution of the electron candidate	82
5.10	The electromagnetic shower produced by an electron is com- pared to that of a hadron	83

5.11	This plot shows the distributions of the shower shape variable E_1/E_9 for electrons and non electrons	85
5.12	This plot illustrates the distributions of the shower shape variable E_9/E_{25} for electrons and non electrons	86
5.13	This figure depicts the χ^2 distributions of electrons and non electrons	87
5.14	The angular difference of the azimuthal angle of the projection of the TEC track at the ECAL and its corresponding shower position in the ECAL	88
5.15	Distribution of the distance of closest approach of the TEC track to the beam line in the $r - \phi$ plane	90
5.16	An event with an electron candidate viewed in the xz plane .	91
5.17	An event with an electron candidate viewed in the xy plane .	92
5.18	The momentum of the muon candidates	94
5.19	The comparison between the data and Monte Carlo for the angular distribution of the muon candidate	96
5.20	The xz view of an event with a muon candidate	97
5.21	The xy view of an event with a muon candidate	98
6.1	A typical Monte Carlo $e^+e^- \rightarrow q\bar{q}$ event display	100
6.2	Comparison between data and Monte Carlo for the number of jets	102
6.3	The angular distributions of jets for the data and Monte Carlo	103
6.4	The distribution of the transverse momentum, P_t , of the electron candidate with respect to the closest jet	110
6.5	The distribution of the transverse momentum, P_t , of the muon candidate with respect to the closest jet	112
6.6	The distribution of the transverse momentum of the electron candidate with respect to the closest jet	117
6.7	The comparison between theory and experiment for bottom and charm production in two-photon collisions	120

6.8	The distribution of the momentum of the electron candidate .	122
6.9	The distribution of the momentum of the electron candidate .	123
7.1	The comparison between the L3 measurement result and theoretical predictions for b quark production	127
7.2	A scheme of the next linear e^+e^- collider	130
B.1	The distribution of the corrected time for all the barrel counters before the calibration in year 2000	143
B.2	The distribution of the corrected time for all the barrel counters after the calibration	145
B.3	The corrected time distribution of all the endcap counters before the year 2000 calibration	147
B.4	This plot shows the corrected time distribution of all the endcap counters after the year 2000 calibration	148
B.5	Efficiencies of two typical barrel counters, 23 and 26	150
B.6	Efficiencies of barrel counters 24 and 25 from 1995 to 2000 . .	151

ABSTRACT

The cross section for bottom quark production in two-photon collisions, $\sigma(e^+e^- \rightarrow e^+e^-b\bar{b}X)$, is measured for the first time. The measurement is performed with the L3 detector at the Large Electron Positron (LEP) collider at the European Center for Nuclear and Particle Physics (CERN). The data corresponds to 410 pb⁻¹ taken at center-of-mass energies from 189 GeV to 202 GeV. Hadrons containing a bottom quark are identified by detecting electrons or muons from their semi-leptonic decays. The measured cross section is in excess of the Next to Leading Order QCD prediction by a factor of three.

CHAPTER 1

INTRODUCTION

“All the fifty years of conscious brooding have brought me no closer to the answer to the question: “what are light quanta?” Of course today every rascal thinks he knows the answer, but he is deluding himself.”

A. Einstein, 1951

1.1 Photon As A Particle

The above statement from one of the greatest physicists of the 20th century reveals the extent to which scientists have been intrigued by the photon or light quanta. In fact the discovery of the photon laid the foundation for one of the greatest achievements of modern physics, quantum mechanics. Prior to the advent of quantum mechanics, light was thought to behave as an electromagnetic wave described by Maxwell equations. The linearity of these classical equations predicts no interaction between different electromagnetic waves. In other words, these waves can pass through each other without any interaction.

However, the classical picture of light waves changed in 1905. In that year, Albert Einstein was able to explain the photoelectric effect by assuming the quantization of light. According to this scheme, light waves are composed of particles that are called photons (γ). The quantum mechanical description of the photon and other subatomic particles was complemented again by quantum field theory. Quantum field theory provides the framework for describing particle interactions. According to field theory, photons can fluctuate into a pair of particle-antiparticle (e.g. electron and positron) or to a

particle with the same quantum numbers (Figure 1.1). This characteristic enables two photons to interact with each other. Therefore photon-photon interactions can be considered one of many areas in particle physics, a branch of physics which deals with elementary particles and their interactions. The physics of elementary particles is also called high energy physics.

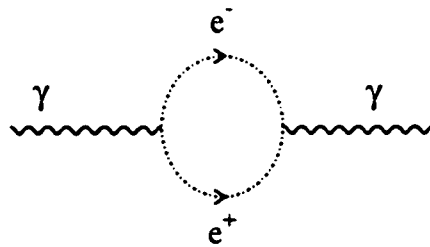


Figure 1.1: The photon fluctuation is depicted in this figure.

All the elementary particles can be classified into two groups of fermions and bosons. Fermions are particles which have half integer spin ($J = 1/2, 3/2, \dots$) and bosons are particles with integer spin ($J = 0, 1, \dots$). The elementary building blocks of matter are fermions and can be classified into two groups of quarks (Table 1.1) and leptons (Table 1.2). Quarks and leptons behave as point like particles. There are three different families of quarks and leptons. Each quark family consists of two different type (*flavor*) quarks, while a lepton family is composed of a lepton and its corresponding neutrino.

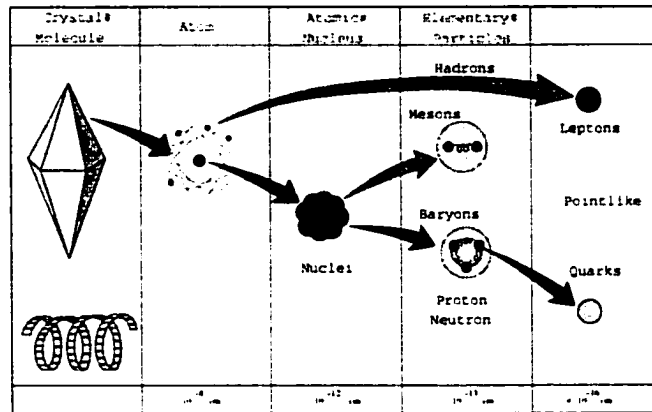


Figure 1.2: Typical sizes for different particles.

Single quarks do not exist in nature. They are only produced in bound states called *hadrons*. Hadrons are further divided into *mesons* and *baryons* referring to the bound states of quark-anti quark or three quarks respectively. Figure 1.2 illustrates the typical sizes of different particles.

Table 1.1: Properties of quarks. The mass is in units of GeV/c^2 . The charge is a fraction of the electron charge, e .

Quark	Mass	Charge
u	0.001-0.005	+2/3
d	0.003-0.009	-1/3
c	1.15-1.35	+2/3
s	0.075-0.170	-1/3
t	169-180	+2/3
b	4.0-4.4	-1/3

The particles that mediate the forces between quarks and leptons are bosons. There are four different forces: electromagnetism, weak, strong and gravitation. Each of these forces has its own mediating bosons. (Table 1.3).

Table 1.2: Properties of leptons. The mass is in units of MeV/c^2 . The charge is a fraction of the electron charge, e .

Lepton	Mass	Charge
e	0.511	+1
ν_e	$< 3 \times 10^{-6}$	0
μ	106	+1
ν_μ	< 0.19	0
τ	1777	+1
ν_τ	< 18.2	0

The production of b (bottom) quark in two photon interaction is discussed in this thesis. The experimental results are compared with theoretical predictions.

Table 1.3: The mediating particles for different forces.

Force	Boson
electromagnetism	photon (γ)
weak	W^\pm, Z^0
strong	8 gluons (g)
gravitation	graviton (G)

1.2 Two Photon Interactions

Two photons can interact with each other through quantum fluctuations. These reveal the structure of the photon. In order to study two photon interactions one needs a continuous source of photons colliding with each other. This can be achieved at an e^+e^- colliding beam accelerator, also called an e^+e^- collider. A large number of electrons¹, called hereafter a beam,

¹Electron will refer to both electron and positron hereafter.

circulates in a storage ring (colliding beam accelerator). The accelerating electrons will emit photons while circulating in the storage ring. This enables us to study the collision of two photons at the interaction point². A typical two photon interaction at an e^+e^- collider can be denoted by $e^+e^- \rightarrow e^+e^- X$ where X is the final state of $\gamma\gamma$ interaction. The number of the emitted photons follows that of bremsstrahlung photons and is proportional to $1/E_\gamma$. The kinematics of this process can be seen in Figure 1.3.

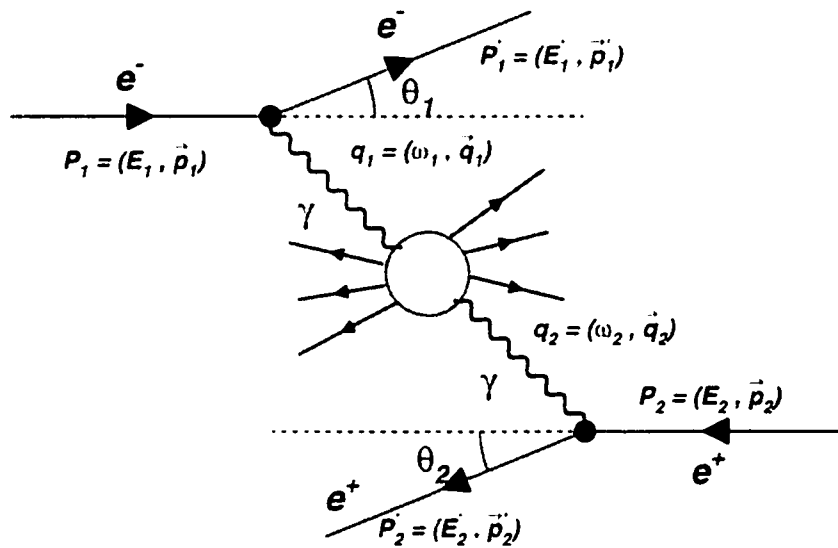


Figure 1.3: Kinematics of two photon interactions at an e^+e^- collider.

Due to the conservation of four momentum, the radiating electrons will be scattered. Their deflection is a measure of the four momentum transferred to the photon (q_1 and q_2). The square of the sum of four momenta of two photons is equal to the center of mass energy of the $\gamma\gamma$ system. One can calculate the squared mass of each radiated photon:

²the point where the beams of electrons and positrons cross each other.

$$q_i^2 = (p_i - p'_i)^2 \approx -2E_i E'_i (1 - \cos \theta_i) \quad (1.1)$$

The above quantity is always negative which is an indication that the radiated photons are virtual (the squared mass of a real photon is zero). It is customary to introduce the following variable as a measure of the *virtuality* of the photon:

$$Q_i^2 = -q_i^2 \quad (1.2)$$

The scattering angle of one or both electrons can be utilized for experimental classification of two photon interactions. There can be three different configurations as follows:

1. **Double-Tag:** In this case, both scattered electrons can be detected in the detector (*tag*). Therefore, the Q^2 value of both photons can be measured directly. In the double-tag scenario, the kinematics of the two photon interaction can be fully reconstructed from the scattered electrons.
2. **Single-Tag:** This is the case where the scattering angle of just one electron can be measured experimentally. The other electron will be undetected due to its small scattering angle. In this configuration one of the photons will have a small virtuality and it is usually called a *quasi-real photon*. Therefore, the single-tag topology can be regarded as the scattering of a virtual photon from a real photon. This type of interaction has provided much information regarding the structure of quasi real photons. The L3 detector (see chapter 3) has the ability to

detect scattering angles as small as 5 mrad. Anything below this angle will be undetected.

3. **Untag:** If both electrons are undetected the interaction will be classified as untagged. In this category the virtualities of both photons are small and they can be estimated only through Monte Carlo simulations.

The energy of the each of the electrons in e^+e^- colliders is called the beam energy, E_{beam} . Another useful quantity, \sqrt{s} , is the total energy of two colliding electrons measured in their center of mass frame. For e^+e^- storage rings, $\sqrt{s} = 2E_{beam}$. An analogous quantity in two photon physics is the two photon invariant mass, $W_{\gamma\gamma}$. This variable can be calculated as follows:

$$W_{\gamma\gamma}^2 = (q_1 + q_2)^2 = (E_1 + E_2)^2 - (\vec{P}_1 + \vec{P}_2)^2 \quad (1.3)$$

where (E_1, \vec{P}_1) and (E_2, \vec{P}_2) refer to the energy and three-momenta of the two scattered electrons. However, it is not possible to calculate the $W_{\gamma\gamma}$ for single-tag and untag final states using the scattered electrons. Under these conditions, $W_{\gamma\gamma}$ can be determined from the final state particles. We then refer to this as the visible invariant mass (W_{vis}) which is defined as follows:

$$W_{vis}^2 = (\sum E_i)^2 - (\sum \vec{P}_i)^2 \quad (1.4)$$

Different types of interactions can happen at e^+e^- colliders. The probability of each of these processes can be quantified by their cross section, σ . The cross section for two photon interactions, $\sigma(e^+e^- \rightarrow e^+e^-X)$ is proportional to $\ln^2(s/m_{electron}^2)$. For other processes such as one-photon annihilation $e^+e^- \rightarrow X$, the cross section decreases as $1/s$ (except for resonance regions).

Therefore, two photon processes become more dominant as we go to higher energies. The dependence of the cross section on \sqrt{s} is depicted in Figure 1.4 for various interactions at e^+e^- colliders. This thesis reports a measurement at the LEP accelerator which was upgraded (LEP2) in 1995.

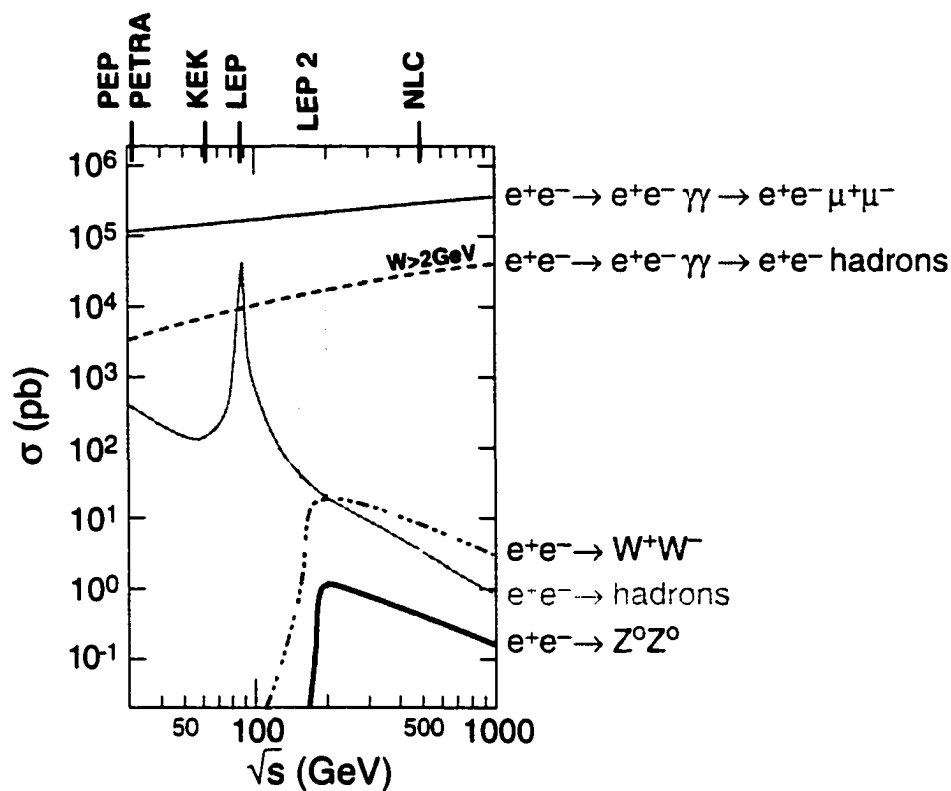


Figure 1.4: Cross sections for several processes. It is evident that two photon interactions are the dominant source of hadron production.

In this thesis, the measurement of the cross section for bottom quark production in two photon collisions is reported. The measurement is done by identifying hadrons containing a b quark. Hadrons containing a heavy flavor quark (c or b) can decay semi-leptonically. This form of decay produces an

isolated lepton which can be tagged experimentally³. Thus the heavy quarks are identified by the tagged leptons. Heavy flavor production in two photon collisions provides useful information on the distributions of quark flavors and gluon in the photon⁴.

The production of b quarks in $\gamma\gamma$ collisions has not been measured. This is because in order to select b hadrons one has to overcome a huge background from c quarks. The c production is higher by two orders of magnitude⁵. In (Figure 1.5) one can see the results of measurements of charm production in $\gamma\gamma$ collisions by different experiments. These measurements were performed at various center-of-mass energies and by different techniques. Most of the experiments have identified charm particles by their semi-leptonic decay or by a D^* (a charmed meson) tag. The earlier measurements have a large uncertainty due to small statistics. The curves in the plot are from Quantum Chromodynamics (QCD) calculations (see chapter 2). It is evident from the plot that the measurements for charm production are in very good agreement with theory. Consequently, we can claim confidently that the mechanisms for charm production in $\gamma\gamma$ physics are well understood.

Another very important test of QCD for $\gamma\gamma$ physics is the measurement of the cross section for bottom ($b\bar{b}$) production. Up to now, this has not been done by experiments. However, the $b\bar{b}$ cross section has been measured in other type of interactions which involve hadrons:

³In this analysis we tag e 's or μ 's.

⁴For a theoretical description refer to the next chapter.

⁵Refer to equation 2.13.

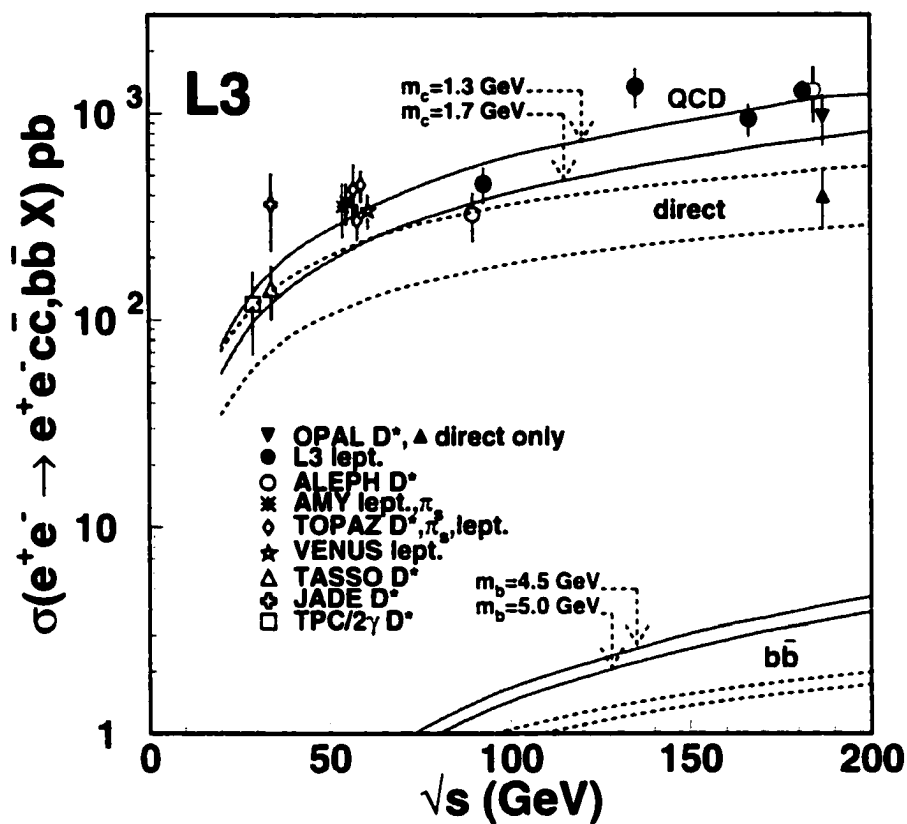


Figure 1.5: The measured cross sections of heavy flavor production in two photon interactions. The dashed lines correspond to the direct process contribution and the solid line represents the QCD prediction for the sum of the direct and resolved processes calculated to next to leading order (NLO). The measurements of charm production cross section agree with NLO QCD predictions. The $b\bar{b}$ cross section was not measured before this thesis. A detailed explanation of NLO QCD, direct and resolved processes can be found in the following chapter.

- γp : The HERA⁶ accelerator provides two high energy beams of positrons (e^+) and protons (p). Since e^+ radiate high energy photons, HERA can be considered as a γp collider. The H1 and ZEUS collaborations at HERA have studied the b quark production in γp interactions [1]. Their measured cross section are almost a factor of three higher than theory prediction (Figure 1.6).

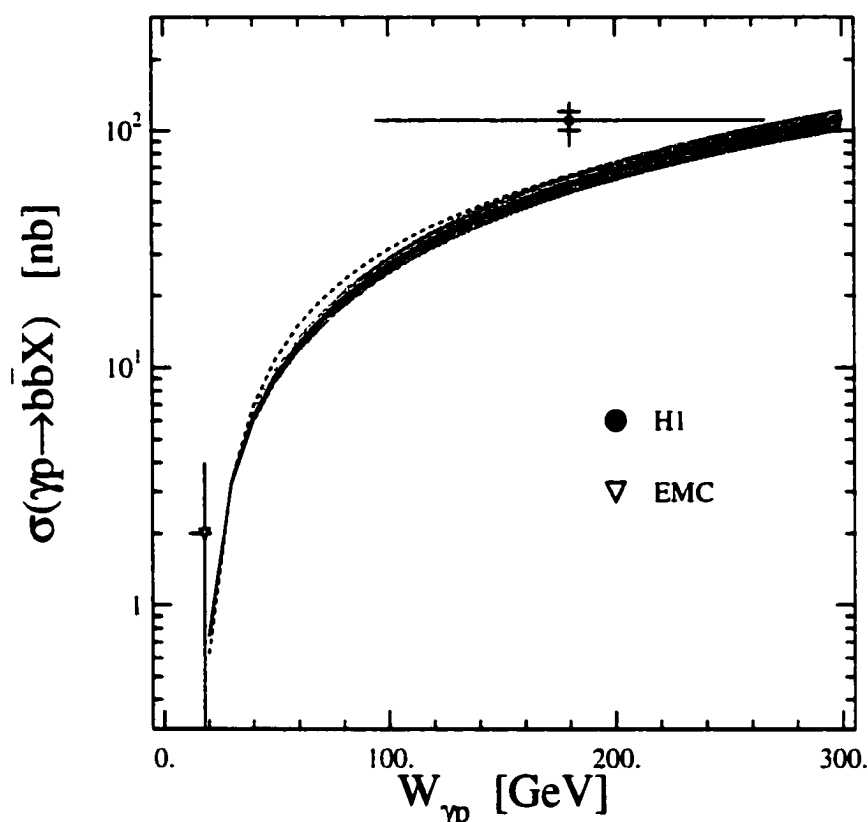


Figure 1.6: The cross section of b quark production in γp interactions as a function of the invariant mass. The horizontal error bar represents the range of the measurement and the shaded area corresponds to the theoretical uncertainty.

⁶Located at DESY lab in Germany.

- $p\bar{p}$: The TEVATRON accelerator at Fermilab is a proton-antiproton collider. The two Tevatron experiments, CDF and $D\bar{0}$ have provided a wealth of knowledge on hadron-hadron interactions. Both experiments have studied the b quark production. The measured cross section by both experiments is higher than the theoretical value. Figure 1.7 compares the $D\bar{0}$ results with the theoretical prediction [2].

Thus, a higher value for the b quark production cross section have been measured in γp and $p\bar{p}$ interactions, consistent with each other. It would be very interesting to compare the theoretical and experimental results for the b quark production cross section in $\gamma\gamma$ collisions. This measurement will be able to confirm or reject the $b\bar{b}$ enigma in hadron collisions. Moreover it is also a good test for QCD in $\gamma\gamma$ physics. Our final result attests to the fact that photons still continue to surprise physicists.

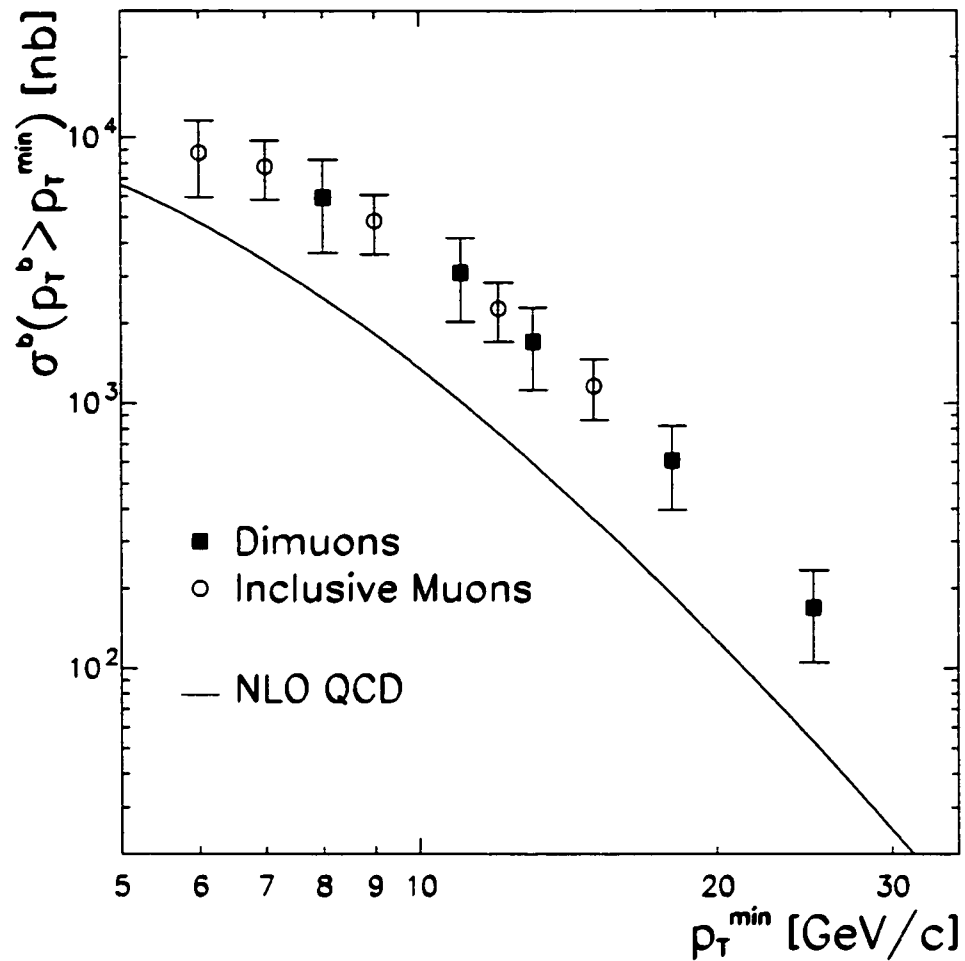


Figure 1.7: The $D\bar{0}$ results for b quark production. The b quarks are identified by their semi-leptonic decay to μ . The cross section is plotted as a function of the transverse momentum of the muon. The dimuon points refer to a sample in which both b and \bar{b} decay to a μ .

CHAPTER 2

QCD AND HEAVY FLAVOR PRODUCTION

2.1 Quantum Chromodynamics

The different interactions among quarks and leptons are successfully described by the Standard Model of particle physics. The Standard Model can be considered as a complete quantum field theory. Similar to any field theory, the standard model can be fully described by its Lagrangian (\mathcal{L}). The Lagrangian for the interaction of quarks and leptons with photons, W^\pm , Z^0 and gluons is ¹:

$$\begin{aligned}
 \mathcal{L} = & \sum_{f=\nu_e, e, u, d} eQ_f(\bar{f}\gamma^\mu f)A^\mu \\
 & + \frac{g_2}{\cos\theta_w} \sum_{f=\nu_e, e, u, d} [\bar{f}_L\gamma^\mu f_L(T_f^3 - Q_f\sin^2\theta_w) \\
 & \quad + \bar{f}_R\gamma^\mu f_R(-Q_f\sin^2\theta_w)]Z_\mu \\
 & + \frac{g_2}{\sqrt{2}}[(\bar{u}_L\gamma^\mu d_L + \bar{\nu}_e\gamma^\mu e_L)W_\mu^+ + h.c.] \\
 & + \frac{g_3}{2} \sum_{q=u, d} \bar{q}_\alpha\gamma^\mu\lambda_{\alpha\beta}^a q_\beta G_\mu^a
 \end{aligned} \tag{2.1}$$

According to the Standard Model, local gauge invariances are responsible for the existence of various interactions. Each interaction emerges as a result of the invariance of the Lagrangian under some transformation of the fields. The strong force is a consequence of invariance under $SU(3)$ group transformations in color space, where color is a concept associated with quarks. The color charge of quarks is responsible for their strong interaction. Each quark flavor is supposed to have one of three possible colors: red, blue or

¹In this formula only the first families of particles are included.

green. Antiquarks are anti-red, anti-blue or anti-green. Gluons, which carry the strong force, possess one color and one anti-color charge, such that color is conserved at each quark-quark-gluon vertex. For example, a blue quark can turn into a red quark by emitting a blue-anti-red gluon. Only colored particles can emit or absorb a gluon. Leptons and other gauge bosons are colorless. The gauge theory of strong interactions is called Quantum Chromodynamics or QCD. Unlike photons which carry no electric charge, gluons carry color charge. Therefore, gluons can interact with each other.

The last term in Eq. 2.1 is the QCD part of the standard model Lagrangian which deals with quark-gluon-quark vertices in the Feynman diagrams. In this term, G^a 's are the eight gluons and λ^a 's are 3×3 matrices which are the $SU(3)$ generators. The quark flavors are described by three component fields (q_α). The g_3 factor is related to the strong coupling constant (α_s) through:

$$\alpha_s = \frac{g_3^2}{4\pi} \quad (2.2)$$

The value of α_s depends on the momentum transfer of the interaction. The same feature holds for other coupling constants as well. For this reason the coupling constants are referred to as running coupling constants. α_s decreases with increasing energy. The values at high energies can be calculated relatively precisely. QCD is a perturbative field theory and its calculations are more reliable as we go to higher energies. However, any QCD Feynman diagram should include the effect of virtual fluctuations on the vertices and propagators. In many cases there are big contributions from these higher order corrections which lead to divergences in calculating physical quantities.

A popular way for canceling these divergences is through renormalization. Renormalization is the procedure in which the effects of the fluctuations can be absorbed into changes in the couplings of the theory. The renormalization prescription requires one to introduce some scale parameters. The two most important of these scales are Λ_{QCD} and μ . Λ_{QCD} is a momentum cut off scale while μ is the renormalization scale for which physics at time scales $\Delta t \ll 1/\mu$ are removed from perturbative calculations. The effect of the small time physics is accounted for by adjusting the value of the strong coupling, so that its value depends on the scale that is used: $\alpha_s = \alpha_s(\mu)$. The μ dependence of $\alpha_s(\mu)$ is given by a differential equation, called the renormalization group equation:

$$\frac{d\alpha_s(\mu)}{d \ln(\mu^2)} = -\beta_0 \alpha_s^2(\mu) - \beta_1 \alpha_s^3(\mu) + O(\alpha_s^4(\mu)) \quad (2.3)$$

where the functions β_0 and β_1 are defined by Eq. 2.4 in which N_f is the number of quark flavors.

$$\begin{aligned} \beta_0 &= \frac{33 - 2N_f}{12\pi} \\ \beta_1 &= \frac{153 - 19N_f}{24\pi^2} \end{aligned} \quad (2.4)$$

The following relationship is derived for the value of α_s as a function of momentum transfer q^2 :

$$\alpha_s(q^2) = \frac{4\pi}{(11 - \frac{2}{3}N_f(q^2)) \ln(q^2/\Lambda_{\text{QCD}}^2)} \quad (2.5)$$

Since the gluons carry color charge, the force between colored quarks does not decrease with distance and the density of force lines remains constant

as the quarks get further apart. Consequently the strong force between quarks increases with distance and the potential contains a term Kr that describes this behavior. This feature leads to color *confinement*. Confinement means that quarks and gluons can not exist in isolation. Quarks are always confined in colorless hadrons, which can be constructed in the following two configurations:

- **Baryon:** a composition of three quarks (one red, one blue and one green) and
- **Meson:** a quark-anti quark pair (with symmetrical superposition of color-anti color).

Due to confinement, quarks can not be studied directly. After their production, quarks *fragment* into hadrons. Fragmentation or hadronization is the process in which a colored quark or gluon transforms into a colorless hadron. This transition involves the creation of additional quark-anti quark pairs. The production of these secondary hadrons is due to vacuum polarization and the increase of the color force with the distance. Experimentalists identify their desired quarks from among a spray of hadrons by indirect means. In theoretical calculations, fragmentation is accounted for by means of fragmentation functions. The corresponding function for fragmentation of quark q to hadron h is denoted by $D_q^h(x)$ where $x = E_h/E_q$. These functions contain information about the way in which quarks turn into hadrons, which is clearly a non-perturbative phenomenon. As a result, the fragmentation functions can not be calculated from perturbation theory. Logically

one expects the fragmentation function for heavy quarks to be concentrated at large values of x since a heavy quark needs to lose only a small fraction of its energy in order to materialize a number of light quarks. Thus a good estimate for the fragmentation function of a very heavy quark, Q , is:

$$D_Q^h(x) \sim \delta(1-x) \quad (2.6)$$

2.2 Two Photon Production In Storage Rings

Two photon interactions are studied at e^+e^- colliders where the accelerating electrons (positrons) emit photons. The frequency and the flux of these photons can be computed precisely through the Equivalent Photon Approximation (EPA) [3] method. This method, which is valid for photons with small virtualities, predicts the following formula for the number of radiated photons:

$$N(x_i) = \frac{\alpha}{2\pi} [1 + (1-x_i)^2] \ln \frac{Q_{i\max}^2}{Q_{i\min}^2} - 2m_e^2 x_i^2 \left[\frac{1}{Q_{i\min}^2} - \frac{1}{Q_{i\max}^2} \right] \quad (2.7)$$

in this equation, the limits on the photon virtualities Q_i^2 and the scaled photon energies $x_i = E_\gamma/E_{beam}$ are determined by the experimental (anti-)tagging conditions on the energies E_i of the scattered electrons. Then the minimum and maximum values of x_i can be calculated by $x_{i\min} = 1 - E_i^{\max}/E_{beam}$ and $x_{i\max} = 1 - E_i^{\min}/E_{beam}$.

The two photon luminosity function ($\mathcal{L}_{\gamma\gamma}$) can be determined by the convolution of the two EPA distributions for the incoming electrons and positrons:

$$\mathcal{L}_{\gamma\gamma}(\tau) = \frac{1}{\tau} \int N(x_1) N(x_2 = \tau/x_1) \frac{dx_1}{x_1} \quad (2.8)$$

$\mathcal{L}_{\gamma\gamma}$ relates the directly measured $e^+e^- \rightarrow e^+e^-X$ cross section, $\sigma_{e^+e^-}(\sqrt{s})$, to the $\gamma\gamma \rightarrow X$ cross section, $\sigma_{\gamma\gamma}(W_{\gamma\gamma})$, of two real photons:

$$\sigma_{e^+e^-}(\sqrt{s}) = \int_{\tau_{\min}}^1 d\tau \sigma_{\gamma\gamma}(W_{\gamma\gamma}) \mathcal{L}_{\gamma\gamma}(\tau) \quad (2.9)$$

2.3 QCD And Two Photon Interactions

Photons couple to the hadron's constituents. Thus two photon interactions provide a good environment for QCD studies.

To first approximation, a photon is believed to be a fundamental pointlike particle (bare photon). Nevertheless, it can also fluctuate into other hadrons which have the same quantum numbers ($J^{PC} = 1^{--}$). These other hadrons are the ρ , ω and ϕ vector mesons. The model that describes photon interactions through this transition is called the Vector Meson Dominance Model or VDM. The inclusion of other higher mass vector mesons like J/ψ or Υ will result in the General Vector Dominance or GVD model. However, the contributions from heavier hadrons is small since VDM predicts that photon fluctuates predominantly to a ρ .

Through their direct couplings to quarks, photons can fluctuate into a quark-anti-quark pair or even a bundle of quarks, anti quarks and gluons. The later state is referred to as the *resolved photon*². The $\gamma \leftrightarrow |q\bar{q}\rangle$ fluctuations may have different virtualities. A quantity that characterizes this virtuality is p_{\perp}^2 , where p_{\perp} is the transverse momentum of the q or \bar{q} with respect to the photon direction. Additional states may arise due to gluon radiation by quarks or gluon coupling to quark-anti quark pairs ($\gamma \leftrightarrow |q\bar{q}g\rangle, |q\bar{q}gg\rangle, |q\bar{q}q\bar{q}\rangle$),

²Some also use the term anomalous to refer to the resolved photon.

etc.). When the virtuality is small the fluctuation is long lived. Under this condition there would be enough time for a cloud of soft gluons to develop around the $q\bar{q}$ pair and produce a vector meson. Therefore VDM describes soft interactions (low p_{\perp}) sufficiently well.

Based on the above considerations, the wave function of the physical photon can be written as Eq. 2.10³ [4]. In this equation c_V^2 , c_q^2 and c_l^2 can be viewed as the probability for the transitions $\gamma \rightarrow V, q, l$. Since leptons do not participate in strong interactions, the last term of Eq. 2.10 can be neglected.

$$|\gamma\rangle = c_{bare}|\gamma_{bare}\rangle + \sum_{V=\rho,\omega,\phi,J/\psi,\Upsilon} c_V|V\rangle + \sum_{q=u,d,s,c,b} c_q|q\bar{q}\rangle + \sum_{l=e,\mu,\tau} c_l|l^+l^-\rangle \quad (2.10)$$

The strong interaction between two photons can yield the following six different categories:

1. **VDM×VDM:** These events are explained by the fluctuation of both photons into vector mesons and subsequent interaction of these hadrons.
2. **VDM×Direct:** Where one bare photon interacts with the quarks of the other VDM photon.
3. **VDM×Resolved:** This is a category in which the quarks of one VDM photon interact with that of the other resolved photon.
4. **Direct×Direct:** In this process the photons act as point-like particles and they couple to each other directly.
5. **Direct×Resolved:** In these events a photon interacts with a gluon content of another photon.

³In this representation the contributions from the t quark are neglected.

6. **Resolved×Resolved:** This type of event proceeds when a gluon component of one photon interacts with that of another photon.

In reality there is no sharp distinction between these different classes. The following three (Figure 2.1) more general categories include all the above scenarios:

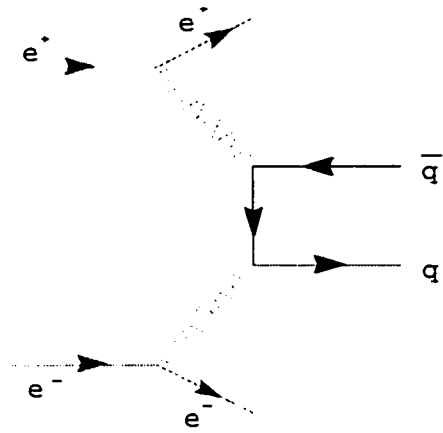
- **Direct:** This process refers to class 4.
- **Single resolved:** Which includes classes 2 and 5.
- **Double resolved:** This category incorporates classes 1, 3 and 6.

2.4 Heavy Flavor Production In Two Photon Collisions

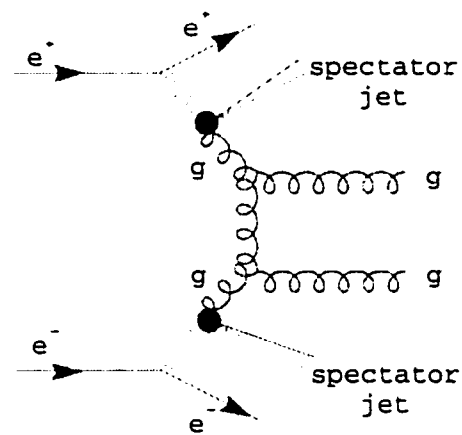
At LEP energies, the contribution from the double resolved process is negligible. At these energies the direct and single resolved processes are predicted to have comparable contributions. The cross section for the direct production of quark Q at the Born level is given by:

$$\sigma_0(\gamma\gamma \rightarrow Q\bar{Q}) = \frac{4\pi\alpha^2 e_Q^4 N_c}{W_{\gamma\gamma}} \left[\left(1 + \frac{4m_Q^2}{W_{\gamma\gamma}} - \frac{8m_Q^4}{W_{\gamma\gamma}^2}\right) \log \frac{1+\beta}{1-\beta} - \beta \left(1 + \frac{4m_Q^2}{W_{\gamma\gamma}}\right) \right] \quad (2.11)$$

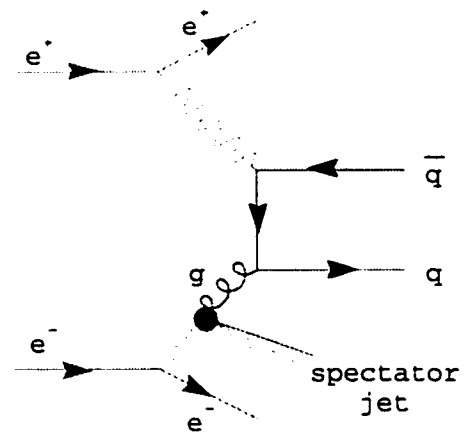
where $W_{\gamma\gamma}$ denotes the total $\gamma\gamma$ energy squared as defined in Eq. 1.3 and $\beta = (1 - 4m_Q^2/W_{\gamma\gamma})^{1/2}$ is the velocity of the heavy quark. It is evident from Eq. 2.11 that the direct production cross section at the Born level is only dependent on the mass of the quark, m_Q . However, QCD calculations can be accompanied by higher order corrections. These corrections are due to the real or virtual gluon emission by quarks. As an example, the direct process



Direct



Double Resolved



Single Resolved

Figure 2.1: Two photon strong interactions proceed via three different general type of processes.

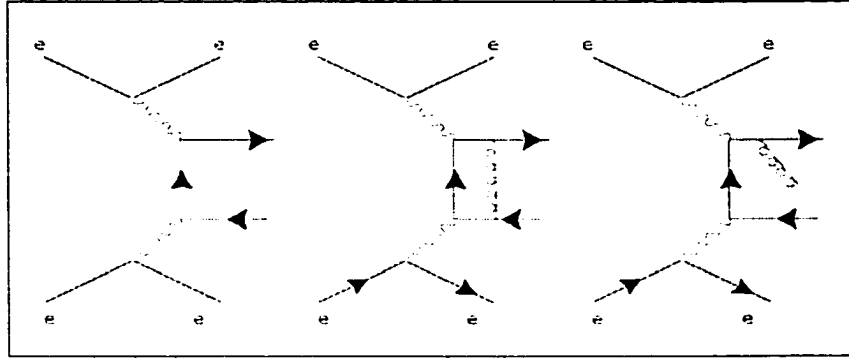


Figure 2.2: The direct process and its corrections due to single gluon radiation.

and its corresponding real and virtual gluon emissions are depicted in Figure 2.2.

A QCD process which does not include these corrections is referred to as Leading Order (LO)⁴. The processes with one gluon radiation are considered to be Next to Leading Order (NLO). The cross section for the direct production at NLO is modified as follows:

$$\sigma(\gamma\gamma \rightarrow Q\bar{Q}(g)) = \frac{4\pi\alpha^2 e_Q^4 N_c}{W_{\gamma\gamma}} \beta \left\{ 1 + \frac{4\alpha_s}{3\pi} \left[\frac{\pi^2}{2\beta} - \left(5 - \frac{\pi^2}{4} \right) + O(\beta) \right] \right\} \quad (2.12)$$

Eq. 2.12 shows the dependency of the cross section on α_s , in addition to m_Q . This dependency is due to the existence of a quark-gluon vertex in the process. From the measurement of the direct production cross section the values of m_Q and α_s can be extracted. Eq. 2.12 can be written in the more convenient form of Eq. 2.13 where $c_{\gamma\gamma}^{(0)}$ and $c_{\gamma\gamma}^{(1)}$ are functions which depend only on the ratio $W_{\gamma\gamma}/4m_Q^2$.

⁴The leading order process is equivalent to Born level.

$$\sigma(\gamma\gamma \rightarrow Q\bar{Q}(g)) = \frac{\alpha^2 e_Q^4}{m_Q^2} (c_{\gamma\gamma}^{(0)} + 4\pi\alpha_s c_{\gamma\gamma}^{(1)}) \quad (2.13)$$

As can be seen from Eq. 2.13, the NLO direct cross section is related to the electric charge and mass of the heavy quark by e_Q^4/m_Q^2 . The existence of this factor predicts the cross section for b quark production to be two orders of magnitude smaller than that for c quark production.

In contrast to the direct process, the resolved interaction depends on the quark and gluon distributions in the photon. The quark distributions of the photon obey a set of inhomogenous evolution equations:

$$\frac{\partial q_i^\gamma(x, Q^2)}{\partial \ln Q^2} = \sum_j \int_x^1 \frac{dy}{y} q_j^\gamma(y, Q^2) \frac{\alpha_s}{2\pi} P_{ij}\left(\frac{x}{y}\right) + 3e_i^2 \frac{\alpha}{2\pi} (x^2 + (1-x)^2) \quad (2.14)$$

The first term in Eq. 2.14 is the standard *Altarelli-Parisi*⁵ evolution equation which holds for any hadron (e.g. proton). The second term comes from $\gamma \rightarrow q\bar{q}$, and is unique for the photon evolution equations. The functions P_{ij} represent the probabilities for the parton⁶ transitions $i \rightarrow j$ and are called splitting functions⁷. Eq. 2.14 allow us to calculate how the quark distributions of photon change with Q^2 . The solutions are derived by using a non-perturbative input at $Q^2 = Q_0^2$. $Q_0 = 0.6$ GeV and a deep inelastic factorization scheme yields a set of Parton Distribution Functions (PDF) which define the *SaSID* photon structure function [5].

The NLO cross section for $\gamma g \rightarrow Q\bar{Q}$ is given as follows:

$$\sigma(\gamma g \rightarrow Q\bar{Q}(g)) = \frac{2\pi\alpha\alpha_s e_Q^2}{W_{\gamma g}} \beta \left[1 + \frac{\alpha_s}{\pi} \left(-\frac{1}{12} \frac{\pi^2}{\beta} + 3 \log^2 8 \beta^2 \right) \right]$$

⁵Altarelli-Parisi equation is described in Appendix A.

⁶Parton is a general term which applies to the constituents of a hadron.

⁷The mathematical description of these functions can be found in Appendix A.

$$-15\log 8\beta^2 - 3\log 4\beta^2 \log \frac{\mu^2}{m_Q^2} + O(\beta)] \quad (2.15)$$

The cross section for the double resolved process at the LO is:

$$\sigma(gg \rightarrow Q\bar{Q}) = \frac{\pi\alpha_s^2}{3s} \left[\left(1 + \frac{4m_Q^2}{s} + \frac{m_Q^4}{s^2}\right) \log \frac{1+\beta}{1-\beta} - \frac{\beta}{4} \left(7 + \frac{31m_Q^2}{s}\right) \right] \quad (2.16)$$

At LEP energies the contribution from the double resolved is much smaller than the direct and single resolved contributions [6]. Furthermore, the analysis of heavy quark production in hadron collisions has demonstrated that higher order QCD corrections can not change the double resolved contribution significantly.

The NLO QCD calculations can be carried through two different procedures that are referred to as *massive* and *massless*. In NLO calculations, terms $\propto \alpha_s \ln(p_\perp^2/m^2)$ arise from collinear emission of gluons by heavy quarks at large transverse momentum (p_\perp) or from almost collinear branching of gluons or photons into heavy quark pairs. These terms might cause the divergence of the perturbation series [7]. In the massive approach, the prediction is limited to a rather small range of $p_\perp \sim m_Q$. On the other hand, the massless approach deals with making predictions at large p_\perp ($p_\perp \gg m_Q$). This method treats the heavy quarks as massless partons. The dependence on the heavy quark mass is then obtained through the fragmentation function of the parton evolved at NLO accuracy from an initial scale $\mu_0 \sim m_Q$ to $\mu \sim p_\perp$. Universal input fragmentation functions can be calculated within perturbative QCD. For this reason they are referred to as Perturbative Fragmentation Functions (PFF). For example a PFF calculated at NLO is⁸:

⁸For a description of $\{ \}_+$ refer to Appendix A.

$$D_Q^Q(x, \mu_0) = \delta(1-x) + \frac{\alpha_s(\mu_0)}{2\pi} C_F \left\{ \frac{1+x^2}{1-x} \left[\log \frac{\mu_0^2}{m_Q^2} - 2 \log(1-x) - 1 \right] \right\}_+ \quad (2.17)$$

where in this equation $C_F = 4/3$. By using the Altarelli-Parisi evolution equations one can find the PFF's at any desired scale $\mu \sim p_\perp$. The important feature of this method can now be realized. The almost singular logarithmic term $\ln(p_\perp^2/m^2)$ splits into two parts. The first part is $\propto \ln(p_\perp^2/\mu^2)$ with no dependence on m and can be eliminated by choosing $\mu \sim p_\perp$. The second part is $\propto \ln(\mu^2/m^2)$ and is absorbed into the PFF's. Due to the high mass of the b quark we have applied the massive method for b quark while the other quarks are discussed in the massless framework.

From previous discussions it became evident that the b quark production cross section at any specific \sqrt{s} depends on m_b and μ . The variation of the cross section with \sqrt{s} is illustrated by Figure 1.5 in which $\mu = m_b$. Fig. 2.3 depicts theoretical predictions of $\sigma(e^+e^- \rightarrow e^+e^-b\bar{b}X)$ at $\sqrt{s} = 194$ GeV as a function of m_b for various values of μ . These theoretical calculations assume a minimum $\gamma\gamma$ invariant mass of $W_{\gamma\gamma} = 10.6$ GeV. This is the minimum energy needed for producing a pair of the lightest B mesons. At the nominal value of $m_b = 4.5$ GeV, the change of the cross section is between 10%-20% when μ is varied from m_b to $2m_b$ and to $m_b/2$ respectively. The sensitivity to the renormalization scale is more pronounced at lower values of m_b . The source of this deviation is the dependence of the resolved process on μ (see Eq. 2.15).

The direct process on the other hand does not change considerably with the variation of μ . As mentioned earlier, this process is primarily dependent

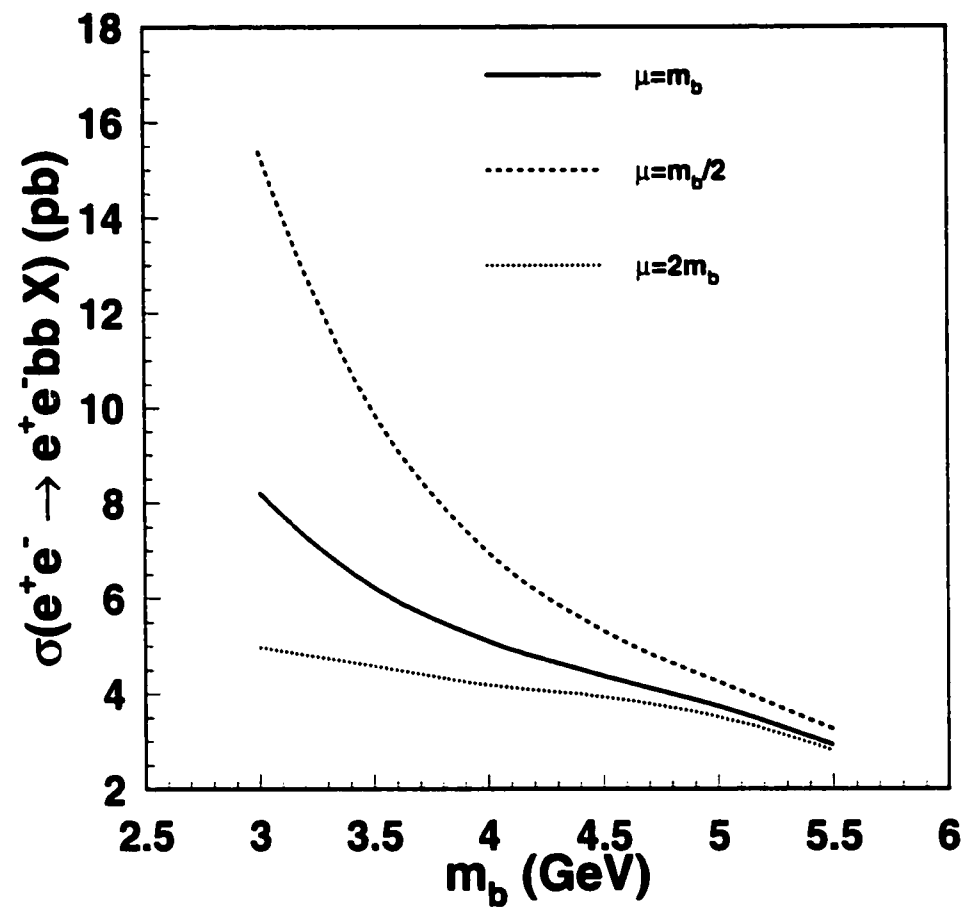


Figure 2.3: The total b quark production cross section as a function of the b quark mass and different values of the renormalization scale.

on m_b and α_s . Figure 2.4 illustrates how the cross section for the direct process remains almost the same for the three different values of μ .

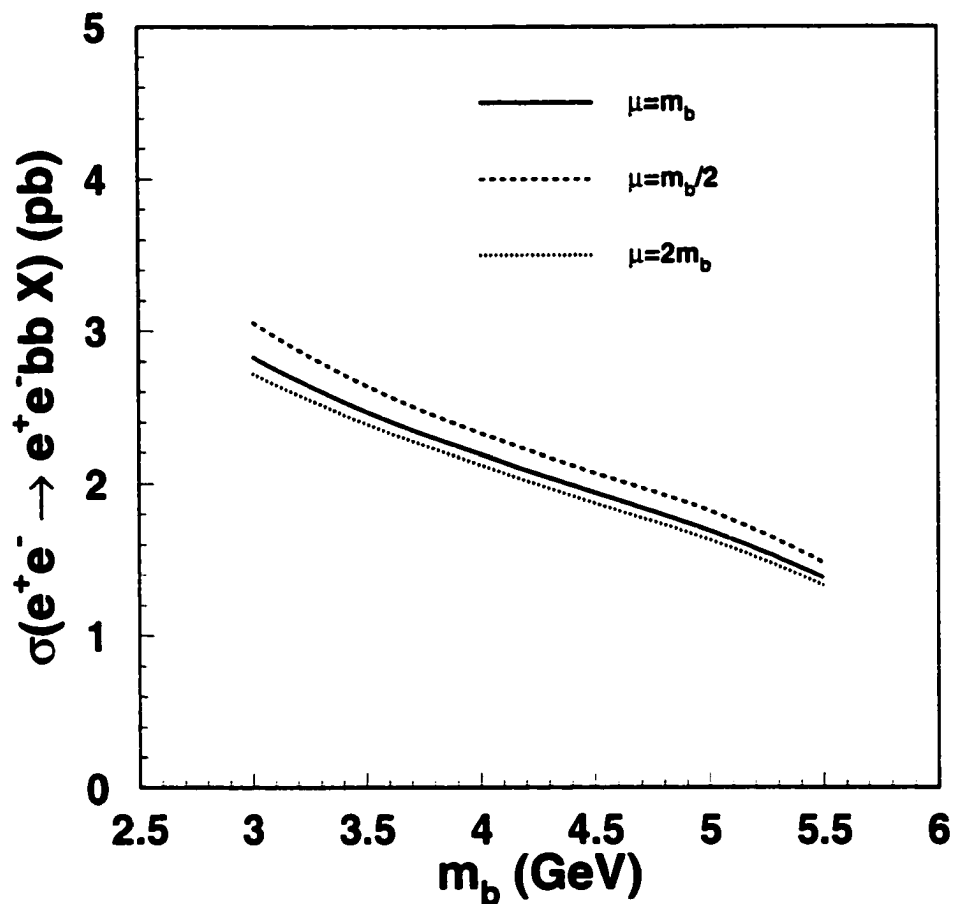


Figure 2.4: The direct b quark production cross section as a function of the b quark mass for various renormalization schemes.

CHAPTER 3

THE L3 DETECTOR AT LEP

3.1 LEP Collider

Particle accelerators can be classified into two groups: fixed target accelerators and storage rings. The beam in a fixed target accelerator is accelerated to its operating energy and then directed at a target which is at rest. The beam in a storage ring, on the other hand, is accelerated to the desired energy and maintained in the ring for as long as possible. In these machines, two beams of counter circulating particles are made to collide head on. Colliding beam machines are able to provide higher center-of-mass energies than fixed target accelerators. This is because s is equal to $4E^2$ for colliding beam machines while it is $2m_xE$ for fixed target experiments (where E and m_x are the beam energy and the target particle mass respectively).

In 1976 physicists at CERN¹ proposed the construction of a large e^+e^- collider. This storage ring is called LEP (Large Electron Positron) [8] and has a 26.7 km circumference. It lies at a depth of 50-150 meters underground at the French-Swiss border (Figure 3.1). The construction of LEP started in early 1980's and it was the largest civil engineering project in Europe. The construction was finished in 1989 and the experiments started taking data in the same year.

The LEP design foresaw operating the accelerator at different beam energies. From September 1989 to October 1995, LEP was operating at the Z^0 resonance region ($\sqrt{s} = 91$ GeV). This period is referred to as LEP1.

¹European Laboratory for Nuclear and Particle Physics



Figure 3.1: A 3 dimensional view of the LEP accelerator. The locations of the four experiments are also shown.

The LEP1 data provided numerous precise measurements for the Z^0 boson. After LEP1, the LEP2 era started in November of 1995. At first, LEP started running at ($\sqrt{s} = 130 - 140$ GeV). This increase in energy was achieved by installing additional accelerating cavities in the LEP machine. The beam energy was increased again in 1996 when LEP was running at W^+W^- threshold ($\sqrt{s} = 161 - 172$ GeV). From 1997 to 2000, LEP ran at even higher energies: $\sqrt{s} = 183, 189, 200 - 208$ GeV. The last period of data was taken at 200 - 208 GeV which is above the design value of LEP. LEP was shut down at 8:00 am of November 2nd of 2000.

The acceleration of electron and positron beams in LEP is achieved through five stages (Figure 3.2). After producing electrons and positrons, they are injected into two linear accelerators of 200 MeV and 600 MeV followed by an Electron Positron Accumulator (EPA). In the next stage, electrons and positrons will be injected into the CERN Proton Synchrotron (PS) where they reach an energy of 3.5 GeV. The PS stage is followed by Super Proton Synchrotron (SPS) which operates at 20 GeV. Finally, the SPS will inject electrons and positrons into LEP where they will be accelerated further to the desired energy before collision.

The LEP machine utilizes RF (Radio Frequency) cavities to accelerate particles. The operating frequency of the RF system is 352.21 MHz. The e^+ and e^- are bent in a circular orbit by a set of dipole magnets. The bending field of these dipoles is relatively low (about 0.1 T) so as to increase the bending radius and thereby reduce the synchrotron radiation. The beam focusing is done by using quadrupole magnets. The LEP vacuum chamber

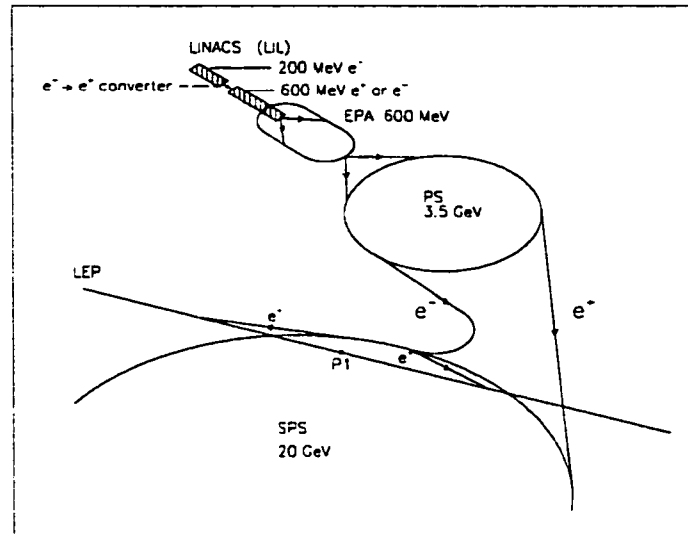


Figure 3.2: The different stages for accelerating electrons and positrons for the LEP accelerator.

must be pumped down to very low pressures in order to minimize the particle losses due to collision with the gas molecules. The pressure in the vacuum chamber is around 10^{-9} Torr while LEP is running.

The e^- 's and e^+ 's are grouped into bunches while they are circulating in the LEP machine. The LEP machine is designed to operate with two bunches of e^- 's and two bunches of e^+ 's (2×2). It can also operate by increasing the number of bunches to four (4×4). Each bunch contains around 10^{12} particles. The bunches cross each other at four equidistant points on the LEP circumference. Four different experiments are located at these points and are called: ALEPH [9], DELPHI [10], L3 [11] and OPAL [12]. Most of the time bunches cross each other without any collision. In the case of a detected interaction, the detector will record all the details of the final state

onto a computer tape. Each recorded interaction is called an *event*. The collection of events is called a *data sample*. The data sample contains events from all possible interactions. It is the job of physicist to select the events of interest and analyze them.

The cross section for any interaction is measured by counting the number of events of that process. However, in order to derive the cross section the intensity of the colliding beams should be measured quantitatively. A useful measure of this intensity is the *luminosity*, L . If two bunches containing n_1 and n_2 particles collide with frequency f , then the luminosity is:

$$L = f \frac{n_1 n_2}{4\pi\sigma_x\sigma_y} \quad (3.1)$$

where σ_x and σ_y characterize the Gaussian beam profiles in the horizontal and vertical directions respectively. The number of events of a particular process and luminosity are related by the following equation. In this equation \mathcal{L} refers to the integrated luminosity, $\int L dt$.

$$N_{events} = \sigma \cdot \mathcal{L} \quad (3.2)$$

where σ is the cross section for the process. Experimentally, \mathcal{L} is measured by using $e^+e^- \rightarrow e^+e^-$ scattering events called *Bhabha*. The cross section of this process is very well understood theoretically and experimentally. Bhabhas are very easy to distinguish and count. Therefore they are very suitable for luminosity measurements.

3.2 Particle Detectors At e^+e^- Colliders

In most e^+e^- as well as $p\bar{p}$ experiments, both beams have the same energy. Under this condition the center of mass energy of the collision will not be

boosted in any particular direction and there will be no preferred direction for the final state particles. Usually the z axis is defined as the beam axis. In terms of polar coordinates, θ is the angle from the positive z axis while ϕ is the angle in the $x - y$ plane measured counterclockwise from the positive x axis. The detectors for these final states try to cover the entire azimuthal (ϕ) range. They also try to include as much as possible of the polar (θ) range. Coverage of the entire θ range is not possible due to the existence of the beam pipe which passes through the detector. Nonetheless, some subdetectors cover θ values as small as a couple mrad.

All collider experiments follow basically the same arrangement for their subdetectors (Figure 3.3).

The subdetector closest to the interaction point is devoted to vertex and track measurements. Most of the unstable particles have a very short life time and decay very close to the beam pipe. For this reason, a vertex detector is the innermost subdetector that the final state particles pass through. Outside of the vertex detector lies the track measurement subdetector. For charged particles, this portion of the detector uses ionization in a gas by the particle to make signals which can be reconstructed into tracks. The tracking system is in a uniform magnetic field so that charged particles make helical tracks. The curvature of the tracks enables the measurements of momentum and sign of the charge of the particle. Neutral particles do not ionize and therefore one can not measure their momentum in the tracking subdetector.

Another main task for any physics analysis is the energy measurement. The energy measurement process is destructive and the specialized subde-

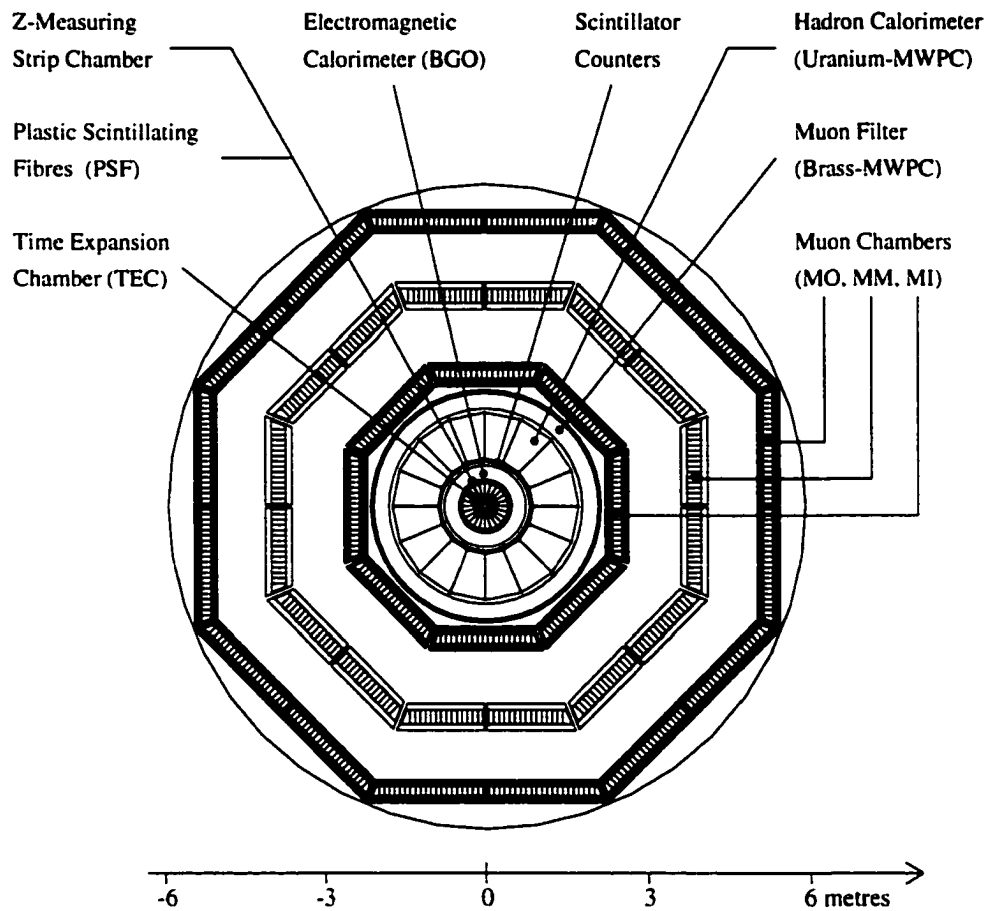


Figure 3.3: The $r-\phi$ view of the L3 detector. The center of all the subdetectors is the interaction point. The three layer muon chamber is the outmost part of the detector.

tectors for energy measurements are called *calorimeters*. Particles lose their energy in the calorimeters through various interactions. The interactions can be either electromagnetic or hadronic (strong) eventually producing a shower of low energy secondary particles. Electromagnetic and hadronic calorimeters are designed to take advantage of the characteristics of these interactions. The parent particles will be destroyed after interacting in these calorimeters. Except for neutrinos and energetic muons, particles will be stopped in one of the calorimeters. Due to the destructive nature of energy measurement, the calorimeter subdetectors always lie after the tracking section. The energy measurement in calorimeters is statistical in nature. The number of secondary particles (N) in the showers is proportional to the energy of the incident particle. This number also determines the resolution on the energy measurement. A higher number of particles in a shower corresponds to a smaller statistical fluctuation (\sqrt{N}) and hence a better energy resolution. In other words, the energy resolution σ_E/E of calorimeters improves with increasing energy.

Electromagnetic calorimeters are devoted to the measurement of electrons and photons. These particles interact only electromagnetically. High energy electrons lose their energy mainly through the bremsstrahlung process while the main mechanism for high energy photons is e^+e^- pair production². The produced particles (γ , e^+ , e^-) will also lose their energies through bremsstrahlung, pair production and ionization (just for e^+ and e^-). This chain of energy loss will continue until the electrons' or photons' energies

²Other processes like Compton scattering and ionization are negligible above 10 MeV.

are below the critical energy³. The final result will be a spray of electrons and photons which is referred to as an electromagnetic shower. The electromagnetic calorimeters are often made of scintillating materials which can measure the energy by the scintillating light produced from the charged particles passing through them. This is based on the fact that the amount of the scintillating light is proportional to the energy deposited in the calorimeter. A useful quantity when dealing with electromagnetic calorimeters is the radiation length, X_0 . The radiation length is the mean distance over which the energy of a high energy electron is reduced by a factor e (by bremsstrahlung).

Hadron calorimeters measure the energy of the hadrons. Hadrons have strong interactions in dense material. In these interactions secondary hadrons are produced and they will continue to interact inside the calorimeter. The final cascade of these particles is called a hadronic shower. Like the electromagnetic calorimeter, hadron calorimeters measure the energy through the energy loss by particles in the shower. The scale for the spatial development of hadronic showers is given by a quantity called nuclear interaction length, λ . The nuclear interaction length is given very roughly by $\lambda \sim 35A^{1/3} (\text{gm/cm}^2)/\rho$ where A is the atomic mass and ρ is the density. Therefore, materials with higher density have a smaller λ . This feature explains why dense, high Z materials are best suited for constructing hadronic calorimeters. The depth of the electromagnetic and hadronic calorimeters depend on the values of X_0 and λ . Logically, the depth of the electromagnetic calorimeter should not exceed 1λ . This is to ensure that hadrons pass through the electro-

³For electron this is the energy at which the energy loss by ionization is equal to the energy loss by radiation. For photon it is the pair production threshold.

magnetic calorimeters without hadronic interactions. The electromagnetic calorimeter should be many X_0 thick to contain the secondary particles from the electromagnetic shower. Also it should be noted that some fraction of a hadronic shower is electromagnetic in nature due to π^0 production and subsequent decay of π^0 to photons. On the other hand, the hadronic calorimeter must be several λ thick to ensure the secondary particles in the hadronic shower are completely contained and measured.

Among the produced particles, muons need a special attention for detection. As a member of the lepton family, muons do not participate in the strong interactions and as a result they will traverse the electromagnetic and hadronic calorimeters losing energy only by ionization and radiation. In addition, since they are almost 200 times heavier than electrons their radiative energy loss is much smaller⁴. As a result the muons will pass through the calorimeters losing a relatively constant energy by ionization and emerging intact. In order to detect muons, most collider detectors contain a specialized subdetector for muons. This section of the detector is usually positioned after both calorimeters. The location of the muon subdetector at the outer most layer of the detector enables physicists to distinguish a muon track from that of other particles. This is because muons are the only particles which can have a track in the tracking chamber matched to a track in the muon chamber. Muon subdetectors measure the momentum of the muons through track reconstruction in a magnetic field. Gas ionization is often utilized for muon track measurements.

⁴The energy loss due to radiation is proportional to m^{-2} where m is the mass of the radiating particle.

3.3 L3 Detector

The L3 collaboration at LEP consists of around 400 scientists from more than 50 different institutes. Louisiana State University (LSU) joined the L3 experiment in 1994. The LSU group includes Prof. Roger McNeil, Dr. Valery Andreev and Sepehr Saremi. Another LSU student (Alan Stone), did his thesis on L3 and completed in 1999. The L3 detector is shown in Figure 3.4.

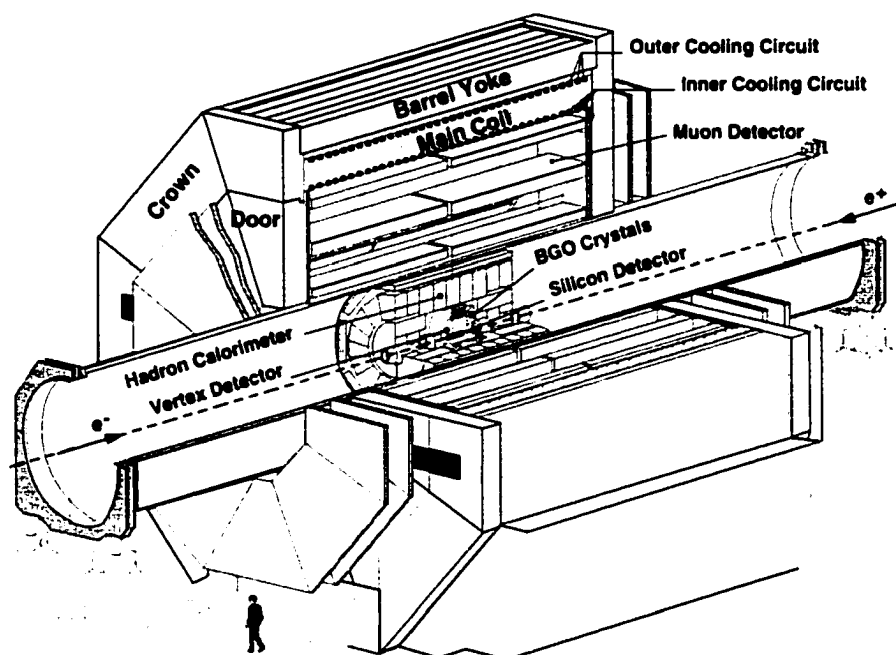


Figure 3.4: The 3 dimensional view of the L3 detector.

L3 subdetectors are in the specified order with equicenters indicated in Figures 3.3 and 3.5. All the subdetectors are installed within a 7800 ton solenoid magnet. The magnet provides a field of 0.5 T parallel to the beam axis. The choice of relatively low field in a large volume optimizes muon mo-

momentum resolution which improves linearly with the field and quadratically with the track length. The L3 detector has dimensions of 14 m and 16 m for length and height respectively (Figure 3.5).

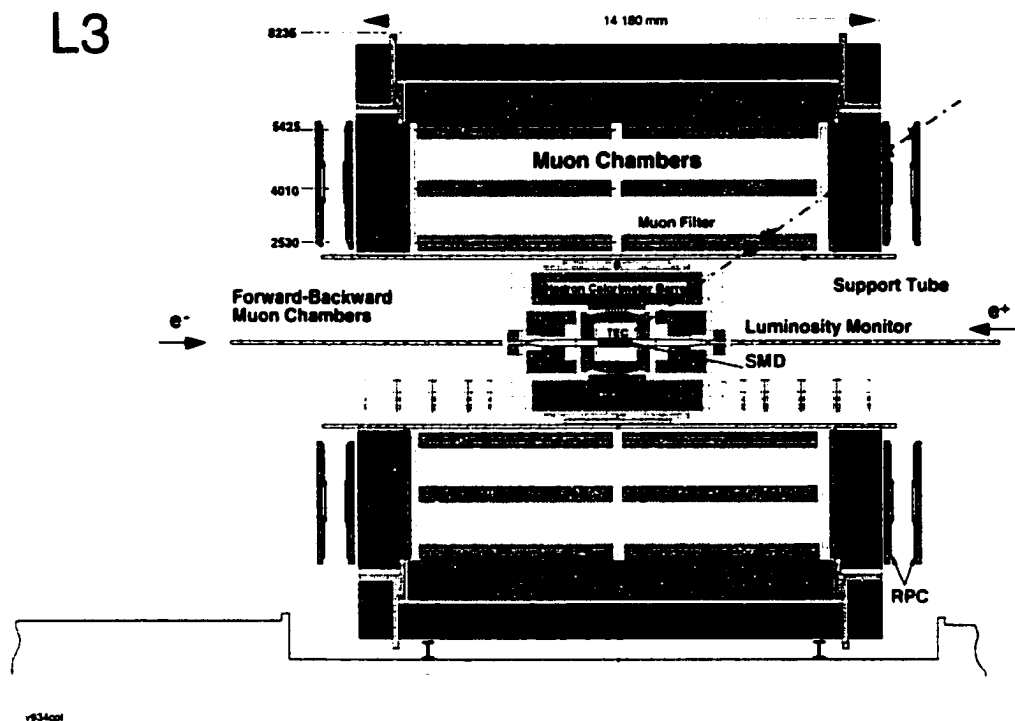


Figure 3.5: The $y - z$ view of the L3 detector.

The entire L3 detector is supported by a 32 m long and 4.45 m diameter steel tube. The central section of the support tube houses the inner subdetectors, arranged as *barrel* elements around the beam pipe and as *end cap* elements in the forward and backward directions. The L3 spatial coordinates are defined in a way that the positive z axis is in the direction of the electron beam and the positive x axis is towards the center of LEP.

The L3 detector uses 24 cm long BGO (bismuth germanium oxide) crys-

tals for its electromagnetic calorimeter. The radiation length of BGO is 1.12 cm which means that the L3's electromagnetic calorimeter extends over more than 21 radiation lengths. Hadron calorimeter in L3 is consisted of depleted Uranium plates sandwiched with proportional chambers (for position measurement). The values of λ for Uranium and BGO are 12.0 cm and 22.0 cm respectively. Thus, the length of the BGO crystals is almost exactly 1λ . For the hadronic calorimeter, the thickness of the modules in the barrel is at least 6λ (including the electromagnetic calorimeter). Figure 3.6 illustrates the shower production in the L3 calorimeters.

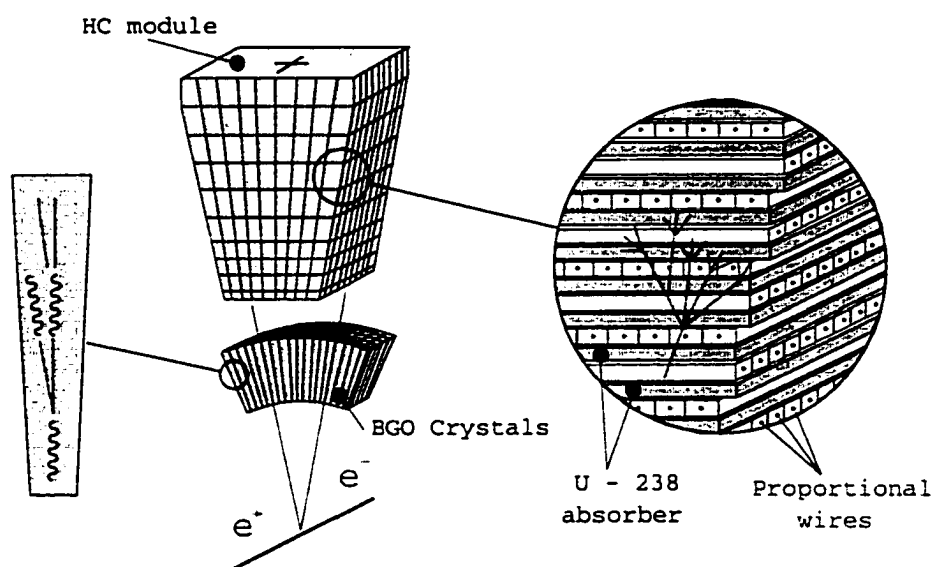


Figure 3.6: Shower production in the BGO crystals and HC (Hadronic Calorimeter) module of the L3 detector.

In what follows a few of the L3 subdetectors important for this thesis work will be discussed.

3.3.1 Time Expansion Chamber

The Time Expansion Chamber (TEC) [13] is one of the innermost sub-detectors in L3 (Figure 3.7) and is designed to fulfill the following tasks:

- precise measurement of the location and direction of the tracks of charged particles,
- determination of the charge and transverse momentum of particles up to 50 GeV/c (essential for Z^0 precision measurements),
- reconstruction of the impact point for the charged particles at the entrance to the electromagnetic calorimeter,
- determination of the track multiplicity originating from the interaction point at the trigger level⁵,
- the reconstruction of the primary vertex and the secondary vertices for particles with lifetimes greater than 10^{-13} s.

The inner and outer chambers are divided into 12 and 24 sectors in ϕ respectively. Figure 3.8 depicts one inner section of the TEC and its corresponding two outer sectors. Each inner sector contains 8 anode wires while each outer sector consists of 54 anode wires. All wires have a positive high voltage. Each of these anode wires is 98.2 cm long and is parallel to the beam line. A charged particle is able to produce at maximum 62 hits while passing radially out through the inner and outer TEC sections. The TEC is filled with a gas mixture of 80% CO₂ and 20% iC₄H₁₀ (isobutane) at a pressure of 1.2 bar. When charged particles pass through the TEC they ionize the gas.

⁵For a more rigorous discussion of the L3 trigger system refer to the following chapter.

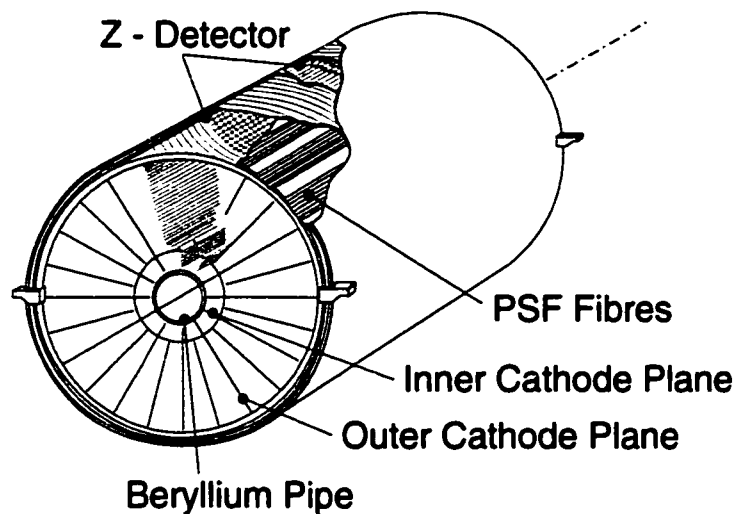


Figure 3.7: The 3 dimensional view of the TEC.

The electrons then drift towards the nearest anode wire at a velocity of $6 \mu\text{m/ns}$ and produce a signal or a hit. The combination of hits produced by any charged particle enables the reconstruction of track of that particle. A reconstructed track provides further information. For example, the momentum of the particle can be calculated by measuring the curvature of its track in the L3 magnetic field. Another useful quantity measured in the TEC is DCA (distance of closest approach of the track projection to the beam line in the $r - \phi$ plane).

The resolution on any track measurement in the TEC depends on the number of hits and the position resolution of a single hit. For a track with polar angle between 35° and 145° , all 62 wires are traversed and the transverse momentum resolution is given by $\sigma_{P_t}/P_t = (0.018)P_t$. Below a polar angle of 35° , the tracks do not traverse the entire TEC radially, and the

number of hits decreases with decreasing polar angle θ which corresponds to a worse resolution for lower values of θ . The total lever arm available for coordinate measurements in the chamber is 37 cm radially. The charge identification of 50 GeV/c particles with 95% confidence level requires 50 coordinate measurements. This is accomplished by two concentric cylindrical drift chambers on common end plates (Figure 3.8).

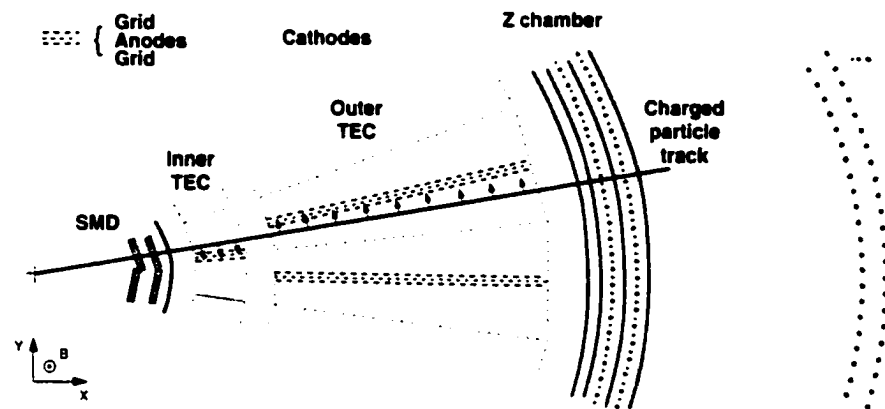


Figure 3.8: One inner sector and two outer sectors of the TEC. Charged particles passing through the chambers ionize the gas. Then the produced electrons drift to the anode wires.

3.3.2 Electromagnetic Calorimeter

The electromagnetic calorimeter (ECAL) is able to measure the energy of the electrons and photons with excellent energy resolution over a wide energy range from 100 MeV to 100 GeV. It surrounds the TEC and consists of about 11000 BGO (Bismuth Germanium Oxide) scintillating crystals. The crystals point to the interaction region and are divided up into the following two sections (Figure 3.9):

- **barrel:** This part contains 7680 crystals which are arranged in two symmetrical half barrels and cover a polar angular range of $42^\circ < \theta < 138^\circ$.
- **endcap:** The two endcaps extend the polar angle coverage to $11^\circ < \theta < 38^\circ$ and $142^\circ < \theta < 169^\circ$.

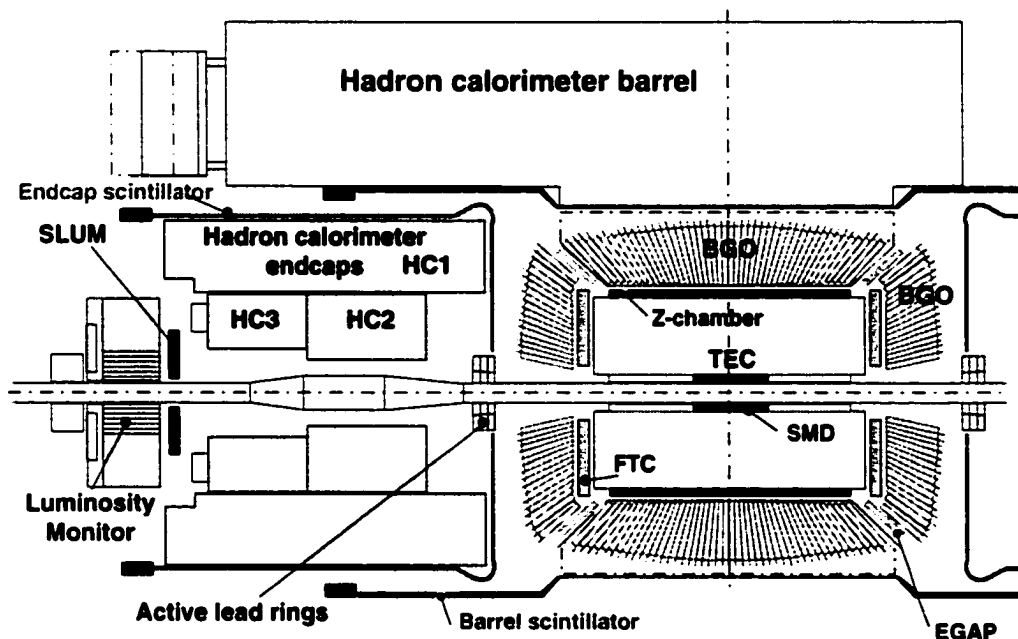


Figure 3.9: The $r - \phi$ view of the central part of the L3 detector.

Each BGO crystal in the ECAL is 24 cm long and is a truncated pyramid about $2 \times 2 \text{ cm}^2$ at the inner and $3 \times 3 \text{ cm}^2$ at the outer end. Due to presence of high magnetic field and lack of space, conventional photomultiplier tubes can not be used for detecting the scintillation light. Instead two 1.5 cm^2 photodiodes are glued to the rear face of each crystal (Figure 3.10). These crystals are insensitive to the magnetic field and have a quantum efficiency

of 70%. The output pulse rise time is 300 ns (corresponding to the BGO light decay time).

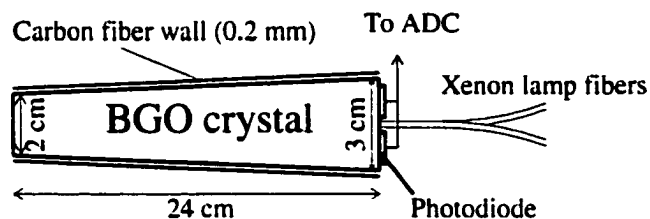


Figure 3.10: The side view of a single BGO crystal.

For each crystal there is one analog to digital converter (ADC) channel with the following two goals:

- accurate measurements of signals over a wide range of 100 MeV to 100 GeV,
- to have a short memory time so that the tails from large signals do not mimic small signals in later beam crossings.

For L3, the energy resolution of the ECAL is about 5% at 100 MeV and is below 1% for energies above 2 GeV. The measured spatial resolution above 2 GeV is better than 2 mm.

3.3.3 Hadron Calorimeter

The hadron calorimeter (HCAL) [14] in the L3 detector is constructed from 5 mm thick depleted Uranium absorber plates interspersed with proportional wire chambers. The small nuclear interaction length of Uranium

(12.0 cm) makes it suitable for hadron calorimetry. The HCAL has 7968 proportional wire chambers and a total of 371764 wires. The proportional wire chambers use a mixture of 80%Ar + 20%CO₂ for their gas. The HCAL has two parts: barrel and endcap. The barrel part covers the central region, $35^\circ < \theta < 145^\circ$. The endcaps cover the polar angle regions $5.5^\circ < \theta < 35^\circ$ and $145^\circ < \theta < 174.5^\circ$. The barrel has a modular structure consisting of 9 rings with each ring containing 16 modules (Figure 3.11). The barrel is 4.725 m long, has an outer radius of 1.795 m and an inner radius of 0.885 m for the three inner rings and 0.979 m for the outer rings.

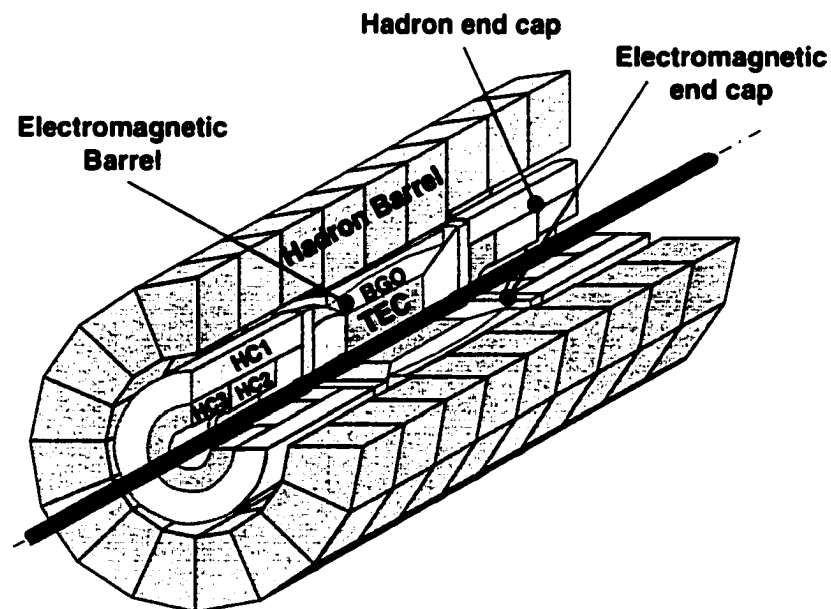


Figure 3.11: The 3 dimensional view of the HCAL.

Usually the visible energy in the HCAL is smaller than the energy of the primary hadron. One reason for this is the existence of particles which can escape the calorimeter carrying away energy. The main source of these particles are μ 's from π decay and ν 's. Therefore, the energy resolution of hadron calorimeters are slightly worse than the electromagnetic ones. In L3, the HCAL has a resolution of better than 10% for the total energy measurement of hadronic events from Z^0 decay. The fine segmentation of HCAL allows an angular resolution of about 2.5° for the measurement of the axis of the *jets* ⁶.

3.3.4 Muon Chamber

The muon chamber (MUCH) [15] occupies a volume of 1000 m^3 . It consists of two 86 ton ferris wheels with each having eight independent units or octants (Figure 3.12).

The muon chamber measures the momentum of the muons through drift chambers. Each octant is made of five precision (P) drift chambers. There are two chambers (MO) in the outer layer, each with 16 signal wires, two chambers in the middle layer (MM), each with 24 signal wires, and one inner chamber (MI), with 16 signal wires. There are also six drift chambers at the top and bottom covers of the MI and MO chambers of each octant. These six drift chambers measure the z coordinate of the μ 's and are called the Z chambers.

Each P chamber contains about 320 signal wires and a total of 3000 wires (including field shaping and cathode wires). As muons pass through the P chambers they ionize the gas (Figure 3.13) and produce electrons that drift

⁶Jets are defined in chapter 6.

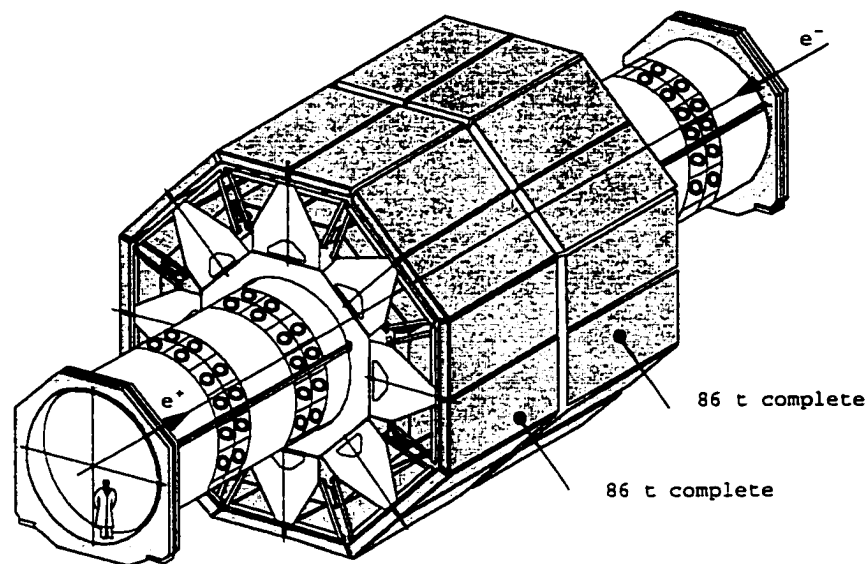


Figure 3.12: The 3 dimensional view of the muon chamber.

to the signal wires in the P chambers. It is very critical to have alignment between chambers of each octant. Systematic errors in the internal octant alignment are kept below $30 \mu\text{m}$. This is achieved through complex mechanical and optical measurements using a laser beam (Figure 3.14). The three layers of the P chambers cover $44^\circ < \theta < 136^\circ$ in polar angle. This coverage has been extended by adding forward and backward muon chambers [16] which are mounted on the magnet doors (Figure 3.15). Including these chambers extend the polar angular coverage to $22^\circ < \theta < 44^\circ$ and $136^\circ < \theta < 158^\circ$. The L3 muon system can measure the momentum of the μ 's with a resolution of $\sigma_p/p = 2\%$ at 50 GeV in the central region. This resolution provides a dimuon mass resolution of 1.4% for $Z^0 \rightarrow \mu^+ \mu^-$.

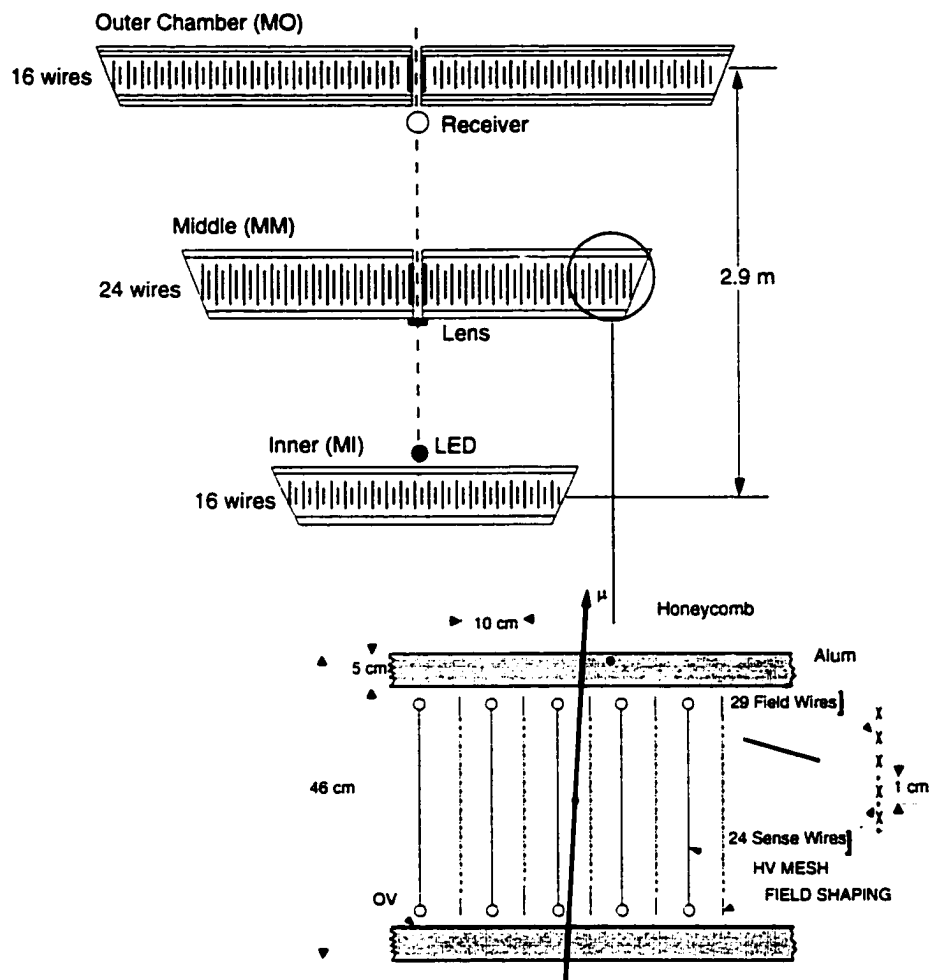


Figure 3.13: The $x - y$ view of one octant of the muon chamber. The five precision chambers can be seen in this figure. MI, MM and MO sample μ tracks 16, 24 and 16 times respectively.

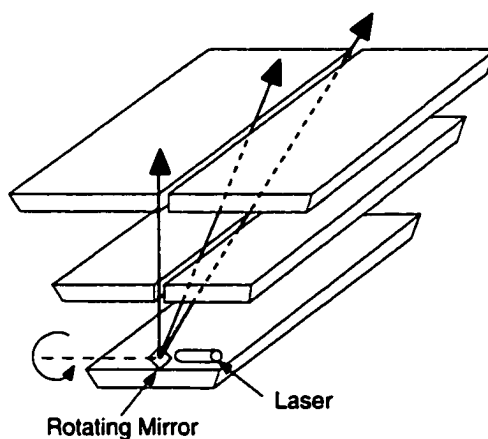


Figure 3.14: Within each octant the five P chambers can be aligned through a laser beam.

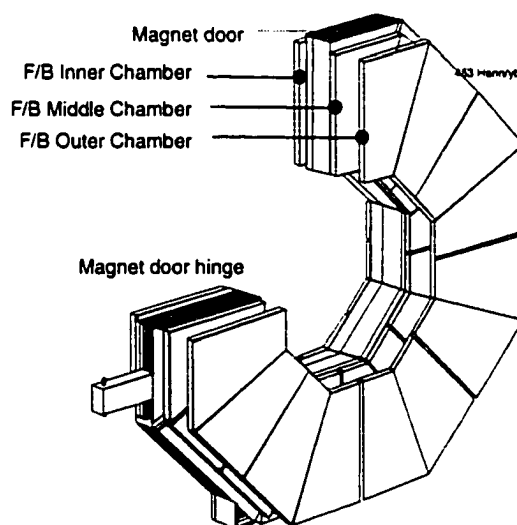


Figure 3.15: The forward backward muon chamber is mounted on the L3 magnet door.

3.3.5 Luminosity Monitor

The main goal of the luminosity monitor [17] is to measure the luminosity \mathcal{L} . As mentioned in section 3.1, $e^+e^- \rightarrow e^+e^-$ Bhabha events are used for this measurement. Since the final state in Bhabha events are a back to back e^- and e^+ , the luminosity monitor should be able to measure electromagnetic showers with great precision. The L3 luminosity monitor consists of two electromagnetic calorimeters and two sets of proportional wire chambers. They are situated symmetrically around the beam pipe, on either side of the interaction point (Figure 3.9). The calorimeter on each side is a finely segmented and azimuthally symmetric array of 304 BGO crystals. The polar angular coverage of the luminosity monitor is $24.93 < \theta < 69.94$ mrad; and on the other side defined by $\pi - \theta$.

The luminosity monitor can be used for other particle measurements as well. As an electromagnetic calorimeter it can measure the energy as well as the angle of electrons and photons in the very forward or backward region of the detector. This can be very crucial for some physics analyses. A good example for one of those analyses is the measurement of the photon structure function when one of the scattered electrons is tagged in the luminosity monitor. In this case the energy and scattering angle of the tagged electron can yield the virtuality of the probing photon.

The Bhabha events are easy to distinguish in the luminosity monitor. They are back to back two particle events with each particle depositing almost E_{beam} energy in each of the luminosity monitors. A typical Bhabha event is depicted in (Figure 3.16). The energy resolution of the calorimeters is about 2% at 45 GeV and the angular resolution is 0.4 mrad in θ and 0.5° in ϕ .

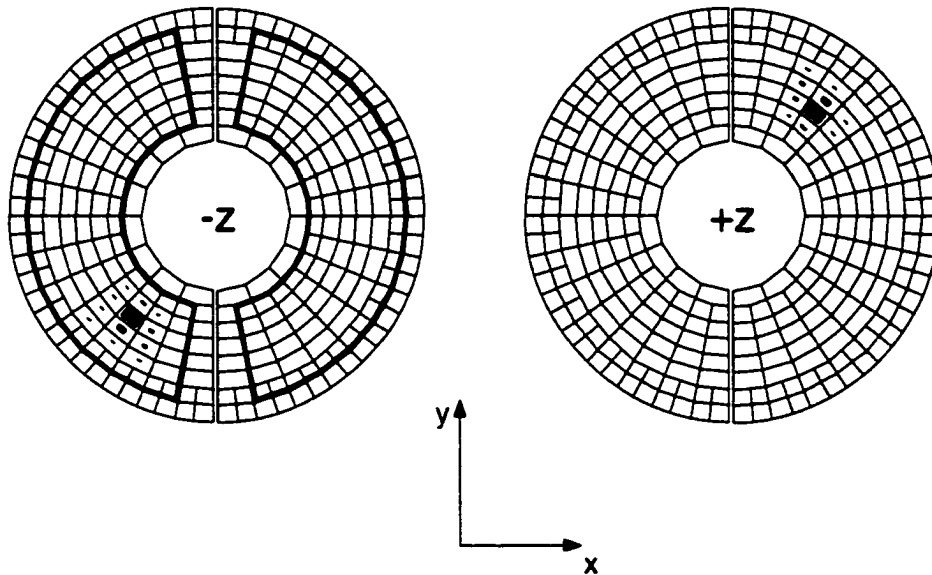


Figure 3.16: A typical Bhabha event in the luminosity monitor. The energy deposit in both calorimeters of the luminosity monitor is shown with black rectangular areas. The size of the black rectangle indicates the energy deposit in that particular BGO crystal.

CHAPTER 4

DATA ACQUISITION AND SIMULATION

4.1 Trigger System

A major challenge for any particle physics experiment is the ability to record all the events of interest. This task is even more critical for collider experiments where there are many beam crossings per second in addition to some non physics backgrounds. These non-physics backgrounds include collisions of beam electrons with gas molecules (beam-gas) or with the beam pipe (beam-wall). At LEP2 energies, the bunches cross each other every $22 \mu\text{s}$ which corresponds to a collision frequency of about 45 kHz. The physics events of interest do not occur at every bunch crossing. Given the LEP luminosity of $10^{31} \text{cm}^{-2} \text{s}^{-1}$, one would expect $e^+e^- \rightarrow e^+e^-\mu^+\mu^-$ two-photon process to occur at a rate of about 100 Hz¹. This rate is still too high for data recording. The identification of events of interest and rate reduction is achieved by implementing a trigger system. In general, a trigger is an electronic signal which indicates the occurrence of an interesting event. After receiving the trigger signal, the on-line software will record the event information from the detector to the data storage system.

The L3 trigger system [18] (Figure 4.1) consists of three levels which can eventually reduce the information rate from 45 kHz to about 3 Hz. The division of the trigger system into different levels increases the speed and efficiency in the decision making process. The level 1 trigger has very loose selection criteria in order to minimize the *dead time*². Once the level 1 accepts

¹Please refer to Fig. 1.4.

²The time during which the detector is unable to record data.

an event, the level 2 starts further checks of the event and in the case of a positive signal (by level 2) the level 3 filters the event. While level 2 (or 3) are processing the signal, their previous trigger level will be reset and ready for filtering the next event. This mechanism reduces the dead time. Each of these trigger levels will be discussed in the following subsections.

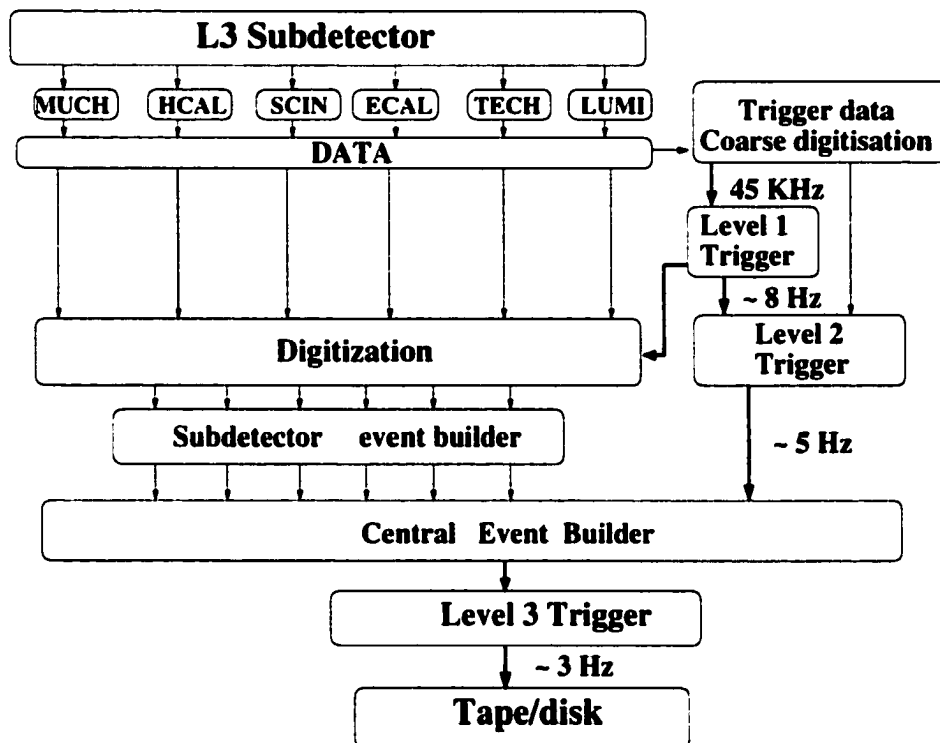


Figure 4.1: The schematic view of the L3 trigger system.

4.1.1 Level 1 Trigger

After each beam crossing all the subdetectors are read by their front end electronics. The electronic signals are sent to the level 1 trigger which will analyze them. In the case of a positive decision, the data will be digitized

and stored in multi event buffers within $500 \mu\text{s}$. For negative decisions, the front end electronics is cleared before the next beam crossing. The rate for positive decisions by level 1 trigger is limited to about 8 Hz which is considerably smaller than the beam crossing rate of 45 kHz. The level 1 arrives at a decision by the logical *OR* of different trigger conditions. The requirements for a positive decision are adjusted to make the efficiency for events of interest high while keeping the level 1 trigger rate less than 8 Hz.

The different subdetectors in L3 contribute trigger signals to the level 1 trigger processor. The requirements for each subtrigger are adjusted to make the overall trigger rate below 8 Hz. The following subtriggers are used:

- **Calorimetric Trigger.**

The level 1 calorimetric trigger [19] is designed to select events with electromagnetic or hadronic energy. The trigger information consists of the energy deposits in the sums of several BGO crystals or hadron calorimeter towers. All the BGO crystals are grouped into 512 blocks (32 in ϕ and 16 in θ) while the HCAL is divided into 2 radial layers with 16×11 and 16×13 blocks. The analog signals from these 896 channels will be digitized and converted into the energy depositions. The digitization takes $8.5 \mu\text{s}$ and $4.8 \mu\text{s}$ for ECAL and HCAL respectively. The event will be triggered if one of the following conditions is met:

- the total calorimetric energy is more than 25 GeV,
- the total calorimetric energy in the barrel region is above 15 GeV,
- the energy in the electromagnetic calorimeter exceeds 25 GeV, or

- the electromagnetic energy in the barrel is at least 8 GeV.

Moreover the event will be accepted under the following criteria:

- a *cluster*³ with at least 6 GeV is found or
- there is a cluster with at least 2.5 GeV that is matched with a track from the TEC trigger or
- there is a single isolated electromagnetic cluster whose energy exceeds 1 GeV (to search for single photon events).

The typical total rate of the calorimeter trigger is 1-2 Hz and the main source of background is electronic noise.

- **Scintillator Trigger.**

The purpose of this trigger is to reject cosmic ray backgrounds and also to select high multiplicity events. There are 30 scintillator counters in the barrel and 32 in the endcap. These counters are shown in Fig. 3.9 and are located between the ECAL and the HCAL. A high multiplicity event should contain at least 5 hits. The mean time of any of the barrel hits should be within 30 ns of beam crossing. This trigger has a typical rate of 0.1 Hz.

- **Muon Trigger.**

This trigger [20] selects events that contain at least one particle which penetrates the muon chambers. If the hits in the muon chambers match

³A cluster is a localized deposit of energy.

any possible track with transverse momentum greater than 1 GeV, the event will be selected. The transverse momentum measurement is performed in either 2 out of 3 of the P-chamber layers or 3 out of 4 of the Z-chambers. The trigger rate is around 10 Hz which is mostly due to cosmic rays coincident with the beam crossing. By requiring one good signal from the scintillator trigger within a narrow time interval about the beam crossing, the trigger rate will be reduced to less than 1 Hz.

- **TEC Trigger.**

This trigger [21] is designed to select events with charged tracks. The minimum transverse momentum for tracks is required to be greater than 150 MeV/c. The selected events should have at least two charged tracks with an *acoplanarity*⁴ of less than 60°. The trigger rate is in the range of 1 to 4 Hz where the fluctuation is due to the variation in beam conditions.

- **Luminosity Trigger.**

This trigger is based on the energy deposition in the two luminosity monitors. Each of the monitors is divided into 16 ϕ sections. The event will be accepted if one of the following conditions is met:

- there are two back-to-back (within ± 1 sector) energy depositions of greater than 15 GeV,

⁴acoplanarity = $\min(|\phi_1 - \phi_2|, \pi - |\phi_1 - \phi_2|)$

- the total energy on one side is greater than 25 GeV, and with more than 5 GeV deposited on the opposite side, or
- the total energy in either side is greater than 30 GeV.

This trigger has a rate of about 1.5 Hz. Since the luminosity monitors are in the vicinity of the beam pipe, the trigger rate can depend on the beam conditions.

4.1.2 Level 2 Trigger

The main function of the level 2 trigger [22] is to reject background from the events selected by the level 1. The level 1 trigger events may contain backgrounds which are caused by electronic noise in the calorimeters, or TEC triggers due to beam-gas, beam-wall interactions, as well as synchrotron radiation. The information from level 1 enters a multi-event buffer in level 2 where they are processed more precisely. The existence of the buffer enables the level 2 trigger to spend more time on each event without increasing the dead time. Events that satisfy more than one level 1 trigger condition will pass the level 2 unhindered. The information in the level 2 trigger is forwarded to an event builder memory regardless of a positive or negative trigger response. In the case of a positive response, the entire data for the event is transferred to the level 3 trigger. For a negative result, the event builder is reset. Usually 20 to 30% of the level 1 triggered events are rejected at level 2 which decreases the total trigger rate (after level 2) to less than 6 Hz.

4.1.3 Level 3 Trigger

The level 3 [23] is the final stage of triggering. The digitized data at this level has finer granularity and a higher resolution. Different algorithms are used to examine the complete digital data for the event. Since the calculations in these algorithms are based on fine digitization, the thresholds can be defined more precisely. Moreover the electronic noise can be further reduced. This allows the requirements of the triggers to be tightened. For example, at this level, tracks from the TEC trigger are required to have deposited at least 100 MeV of energy in the calorimeters. They are also examined for their quality and common vertex. Like level 2, the events which fulfill more than one level 1 trigger condition will pass through. The level 3 trigger reduces 40 to 60% of the events which are passed by the previous level. Consequently the final rate of the entire trigger system will be of 2 to 3 Hz. Therefore, there is a reduction in the number of events that pass through each trigger level. However, the trigger system is designed in a way to minimize the loss of physics events of interest. 94.4% of the desired events for this analysis are triggered at level 1. All these events can be triggered at levels 2 and 3.

The level 3 information will be stored in a memory buffer on the main on-line computer. From this buffer the events are written on tape. Physicists will use these tapes to analyze the data.

4.2 Event Reconstruction

The data on tape are in the form of raw information like drift times for hit wires, etc. The next step is to extract physical quantities from these raw data. The L3 collaboration has developed a special software program called REL3 [24] which transforms the raw digitized detector signals into physical

variables. REL3 reconstructs objects in each subdetector and in some cases it may combine objects from several subdetectors⁵. An example of some of the physical variables which are reconstructed from a few subdetectors are given below.

4.2.1 Tracks In The TEC

The measured drift times for the hit wires are converted into space coordinates. A pattern recognition algorithm then associates the hits to reconstruct tracks in the $r - \phi$ plane. Afterwards a circle is fitted to the track which yields the curvature and the distance of closest approach (DCA) to the vertex. The curvature can provide further information such as the momentum and the sign charge of the particle.

4.2.2 Clusters In The Calorimeters

Particles lose their energy in the calorimeters by producing showers. Due to the segmentation of the ECAL and HCAL, it is possible to form a geometrical object called an ASRC (A Smallest Resolvable Cluster). These clusters are composed of a group of adjacent BGO crystals or HCAL towers which contain the shower. Each ASRC roughly corresponds to a single final state particle. The energy of the ASRC's are derived by converting the ADC (Analog to Digital Converter) signals into the energy values. Each BGO crystal and each HCAL tower must have energies greater than 10 MeV and 9 MeV respectively in order to be included in a cluster. This requirement is imposed to distinguish electronic noise from real energy deposition. In addition to the total energy of ASRC's there are some shower shape variables that

⁵An example of this is combining a reconstructed track in the muon chamber with that of the TEC.

can be calculated. The three most important variables for shower shapes in the ECAL are:

- E_1/E_9 ; which is the ratio of the energy deposited in the central crystal of the cluster to that of its 9 surrounding crystals.
- E_9/E_{25} ; this is the ratio of the energies in the 9 and 25 crystals around the cluster barycenter.
- χ^2 ; this is the statistical χ^2 which is derived by fitting the shower shape with the shape of an electromagnetic cluster.

It will be seen in the following chapters that the above shower shape variables will be extremely useful in distinguishing electrons from other charged particles.

4.2.3 Muons In The MUCH

The MUCH reconstructs muon tracks from the wire hits. A pattern recognition algorithm fits the hits in the MUCH with those in the TEC. A muon track which is matched to a TEC track is called AMUI and it represents a muon produced in the TEC. The DCA of an AMUI is defined the same way as for tracks in the TEC.

4.3 Monte Carlo Simulation

There are two different type of analyses in particle physics experiments. The analysis may be focused on searching for new physics or it can deal with high precision measurements. In the former case, one needs to know exactly what are the signatures of the new particle or the new phenomena while

for the later scenario a precise understanding of the systematic errors are required. Both these tasks require simulation of the process under study as well as the backgrounds. The event simulation is done through the *Monte Carlo* method in the following two steps:

- **event generation**; in this step a theoretical model is used to create events containing different particle types. The event generator will produce the kinematics of the final state particles (number, type and 4-momentum) as well as the cross section according to a theoretical calculation.
- **detector simulation**; which is performed after the events are generated. In this stage the generated particles are propagated through a detailed representation of the detector. The response of each active (chamber or calorimeter) element is simulated.

The simulated events will be written on tapes called Monte Carlo tapes. These tapes will be used in the same way as the data tapes. From this point the REL3 program can be used to reconstruct these Monte Carlo events and produce simulated data events that can be analyzed the same way (using the same program) as the real data.

4.3.1 Event Generation

For this analysis, the PYTHIA 5.7 [25] Monte Carlo is used to simulate two-photon signal events. This event generator is based on the current knowledge of pp and γp hadronic interactions. All the two photon processes

are generated with massless matrix elements⁶. The *SaS1d* photon structure function [5] is used for the resolved process and the two photon luminosity function in the equivalent photon approximation is implemented with a cut off value of $Q^2 < m_\rho^2$ [26].

Background sources to the process studied ($e^+e^- \rightarrow e^+e^-b\bar{b}X$) are $e^+e^- \rightarrow e^+e^-\tau^+\tau^-$, $e^+e^- \rightarrow Z^0/\gamma \rightarrow q\bar{q}$, $e^+e^- \rightarrow \tau^+\tau^-$ and $e^+e^- \rightarrow W^+W^-$. The Monte Carlo generators which are used for these processes are JAMVG [27], PYTHIA [25], KORALZ [28] and KORALW [29] respectively.

4.3.2 Detector Simulation

The general purpose high energy physics detector simulation program available is called GEANT. This software performs the detail simulation of particle interactions inside the detector taking into account the geometry and the materials used in the detector. All the relevant processes such as decays, energy loss, multiple scattering, nuclear interactions, bremsstrahlung, and pair production are simulated. Secondary particles produced in these interactions are also followed through the detector material.

The L3 detector simulation program is called SIL3 and is based on GEANT3 [30]. SIL3 includes the details of each L3 subdetector with a spatial accuracy level of 10-100 μm . The fine tuning of parameters in the simulation was done using results from test beam experiments. Examples of these tuning include the light collection efficiency and electronic noise in the ECAL and Uranium noise in the HCAL according to the experimental spectra. Hits in the central tracking chamber and in the muon chamber are simulated using

⁶Due to the high mass of b quarks, the massive matrix element approach is used for $e^+e^- \rightarrow e^+e^-b\bar{b}X$.

the time-to-distance relation measured in the test beam data [31]. Details of the response, such as multiple hits and δ -rays are included. The scintillator ADC and TDC information are also simulated and pulse heights are corrected for attenuation.

There are imperfections in the real L3 detector such as dead cells, noisy BGO crystals and inefficient wires. These imperfections usually vary with time. In order to do a precise measurement these irregularities must be completely accounted. However, it would be very time consuming to incorporate these imperfections at the detector simulation level. They are taken care of in the reconstruction level of the simulated events; the final outcome is called *real detector simulation*.

4.4 Final Data Structure

Finally, the data and Monte Carlo tapes are used to carry the last stages of the analysis. Physicists try to select their desired events from the data tapes and they will also use the Monte Carlo tapes to study backgrounds, efficiencies, purities and systematic errors. Each analysis requires events of a specific type to be selected and studied. For this reason each physicist will develop a unique code to select his/her events. First, the code is transformed into an executable format. Then, the executable can be used for reading the data (or Monte Carlo) tapes. The selected events are stored in a data structure called *ntuples*. The ntuples contain the physical variables such as the momentum of tracks and the energy of clusters of the selected events. The software which is used for working with ntuples is called PAW (Physics

Analysis Workstation). PAW enables physicists to make distributions of different variables as well as to look for correlations between them.

CHAPTER 5

EVENT SELECTION

5.1 Hadronic Two-Photon Events

The data tapes contain event data structures from all kinds of physics processes. Some of these interactions are mentioned in Figure 1.4. To study any specific interaction requires the physicist to select the events of that process from the data tapes. Usually the selection takes place in different phases. In the first phase, physicists try to select a broad event sample in the form of ntuples. In later stages they try to apply more restrictive conditions in order to select the final events.

In order to measure the b quark production cross section in two photon collisions one selects events of the process:

$$e^+e^- \rightarrow e^+e^-b\bar{b}X$$

However, in order to study the backgrounds, the event selection proceeds through two different stages. In the first stage, events are selected which come from the process:

$$e^+e^- \rightarrow e^+e^-q\bar{q}X$$

These events are called hadronic two photon events since q and \bar{q} will produce hadrons. Our data sample, at this level, contains around one million events. A large fraction of the sample will consist of two-photon production of pairs of u, d and s quarks. Due to the much higher cross section for light

quark production the fraction of c and b quarks will be one and three orders of magnitude smaller respectively. The next step is aimed at identifying one of the quarks as being a heavy quark, Q or \bar{Q} . In this analysis, heavy quarks ($Q = c$ or b) are distinguished by their weak semileptonic decays:

$$b \rightarrow c + l + \nu_l \quad (l = e, \mu)$$

$$c \rightarrow s + l + \nu_l \quad (l = e, \mu)$$

Figures 5.1 and 5.2 show the schematic diagrams for these processes. The semi-leptonic branching ratio of the b quark to electron or muon is 10.86% and 10.95% respectively. In these processes the c and s quarks will fragment into hadrons and produce a spray of secondary particles which is called a *jet*¹. The neutrino, ν_l , will escape the detector undetected. Therefore one would expect a jet and a lepton as the result of a heavy quark semileptonic decay.

The heavy quarks are produced in pairs, so it is sufficient to identify one of them. An attempt to identify both Q 's will reduce the statistics considerably due to the small semileptonic branching ratio (around 10%).

Two-photon events $e^+e^- \rightarrow e^+e^-X$ can be divided into three different classes as explained in section 1.2. This analysis is restricted to the untag condition in which the scattered electrons are not detected. In this condition, the scattering angle of the electrons is very close to the beam pipe and the photons have a small virtuality (Q^2). The photons in this analysis are quasi-real with $\langle Q^2 \rangle \cong 0.015\text{GeV}^2$. The PYTHIA Monte Carlo program does

¹The algorithm for jet reconstruction is discussed in the following chapter.

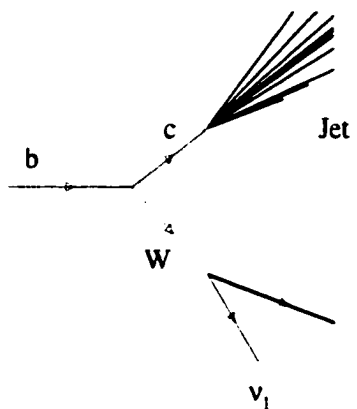


Figure 5.1: The Feynman diagram for a b quark semi-leptonic decay.

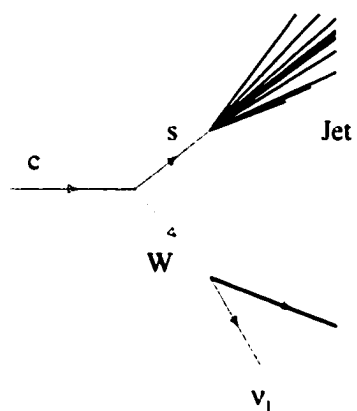


Figure 5.2: The Feynman diagram for a c quark semi-leptonic decay.

not include the single and double tag configurations. PYTHIA generates events with $Q^2 < m_\rho^2$. Consequently, the data event selection was restricted to the untag topology in order to maintain a consistency between data and Monte Carlo.

Any event selection in a particle physics analysis is accomplished by applying a set of constraints to some physical variables. The constraints are chosen based on the physical characteristics of the signal events. Selecting events with a constraint on a variable X is referred to putting a cut on the variable X . Each cut is applied with the aim of separating the desired (signal) from the unwanted (background) events. The most important backgrounds for this analysis are:

- $e^+e^- \rightarrow q\bar{q}$
- $e^+e^- \rightarrow W^+W^-$
- $e^+e^- \rightarrow \tau^+\tau^-$
- $e^+e^- \rightarrow e^+e^-\tau^+\tau^-$

where the first three processes are annihilation events and the last one is a two-photon process. In order to suppress lepton pair production processes such as $e^+e^- \rightarrow e^+e^-l^+l^-$ and $e^+e^- \rightarrow l^+l^-$ ($l = e, \mu, \tau$), only events with more than four good tracks are selected ($N_{trk} > 4$). A good track is defined by the following track quality criteria:

- a transverse momentum, P_t , greater than 100 MeV,
- more than 15 wire hits in the TEC (out of maximum 62 hits),

- and a distance of closest approach to the interaction point in the transverse plane, DCA, smaller than 5 mm.

Hadronic two-photon events in general have less energy visible in the detector than do annihilation events. A good strategy for hadronic two photon event selection is to apply cuts on the visible energy (E_{vis}) and visible mass (W_{vis} , see Eq. 1.4). In addition, the event selection should take into account the untag condition for two-photon events. This requirement is met by putting a cut on the most energetic cluster in the luminosity monitor (E_{Lumi}). The cuts applied on these variables are as follows:

- $E_{vis} < 0.33\sqrt{s}$
- $W_{vis} > 3 \text{ GeV}$
- $E_{Lumi} < 0.4E_{Beam}$

where E_{vis} is the sum of the energies that are measured in the electromagnetic and hadronic calorimeters ($E_{vis} = \sum E_i$). It also includes the energies of the μ 's by measuring them in the muon chambers. A cut on the visible energy is very efficient in distinguishing hadronic two photon events from other type of backgrounds (Figure 5.3 illustrates this point). In this figure all the other cuts (except E_{vis}) are applied. This type of plot is called an $N-1$ distribution where N signifies all the individual cuts. The great advantage of $N-1$ plots are their ability to demonstrate the effect of each cut individually. They are also useful for comparing data and Monte Carlo distributions for different cuts. In this plot the simulated background events are normalized to the data

luminosity. The arrow shows the location of the cut on E_{vis} . At low E_{vis} the data is dominated by two-photon hadronic events with low backgrounds. There are also two visible bumps in this plot. The bump at 1 is due to the $e^+e^- \rightarrow q\bar{q}$ annihilation events where all the center of mass energy of the collision is observed in the detected particles. The peak at 0.6 is due to the back to the Z^0 events. These are events in which one of the incoming electrons emits a photon energetic enough to reduce the center of mass of the collision to that of Z^0 resonance where the cross section is much larger. The peak in the first bin of the Monte Carlo distribution corresponds to the τ pair production in two-photon collisions. The good agreement between the data and the Monte Carlo simulations indicate a good understanding of our detector and backgrounds.

W_{vis} is calculated from the four momentum vectors of the measured particles, tracks and calorimetric clusters including those from the luminosity monitor. These particles are considered to be pions except for unmatched electromagnetic clusters considered as photons. Figure 5.4 shows the comparison between the data and Monte Carlo for this variable at the $N - 1$ level. A cut of 3 GeV is applied since the PYTHIA Monte Carlo only generates events with a two-photon invariant mass greater than 3 GeV. In addition, this cut removes some of the nonphysics backgrounds such as beam-gas interactions.

In the untag configuration, the scattered electrons are very close to the beam pipe and they do not hit the luminosity monitor. Electrons that are tagged in the luminosity monitor, lose most of their energy in this subdetector. In order to separate the untag events, a cut is applied on the energy of

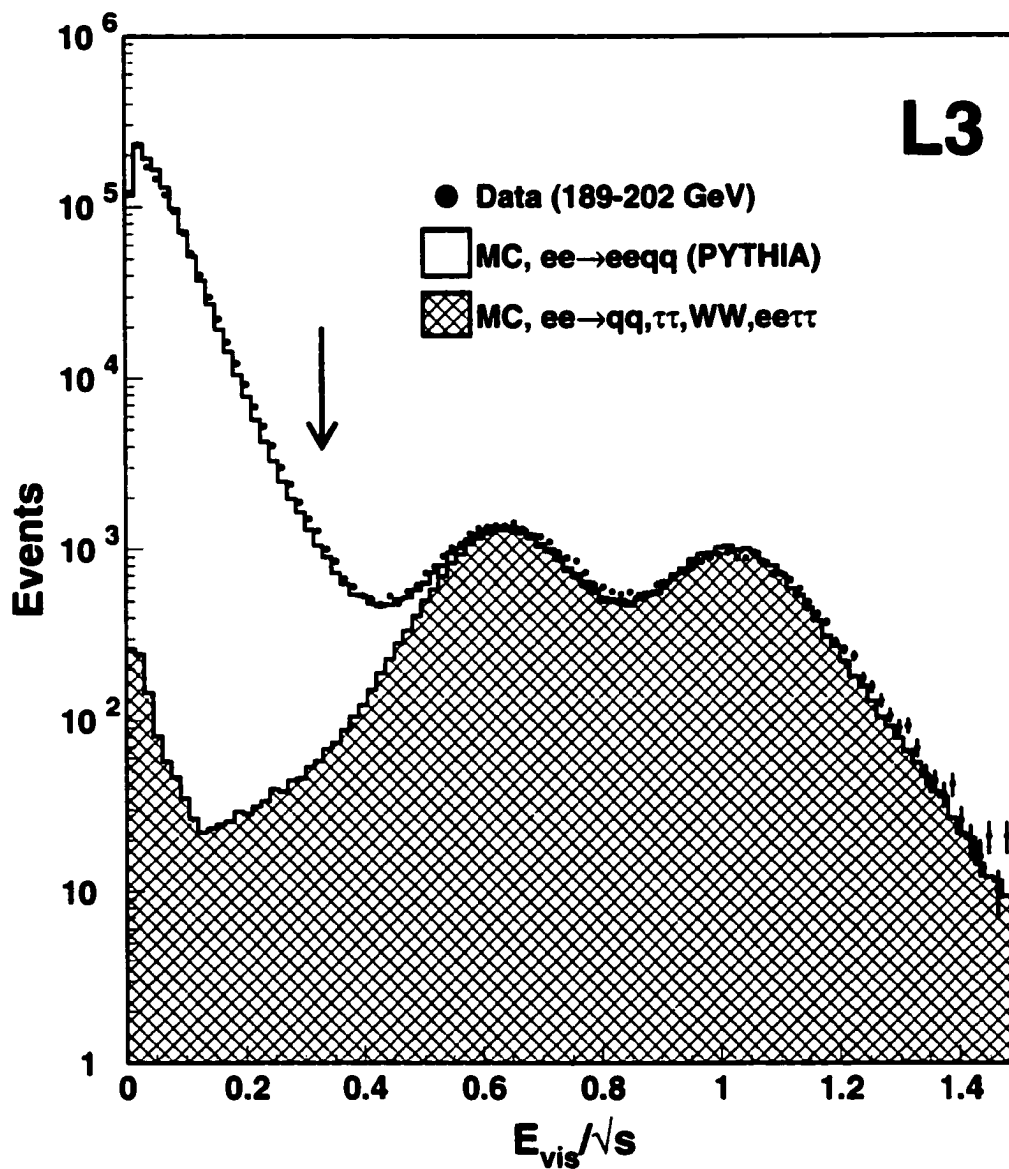


Figure 5.3: The comparison between data and Monte Carlo for the total visible energy. The distribution for signal and background have been scaled to the data luminosity. A cut at $E_{vis} < 0.33\sqrt{s}$ is very effective in removing annihilation events.

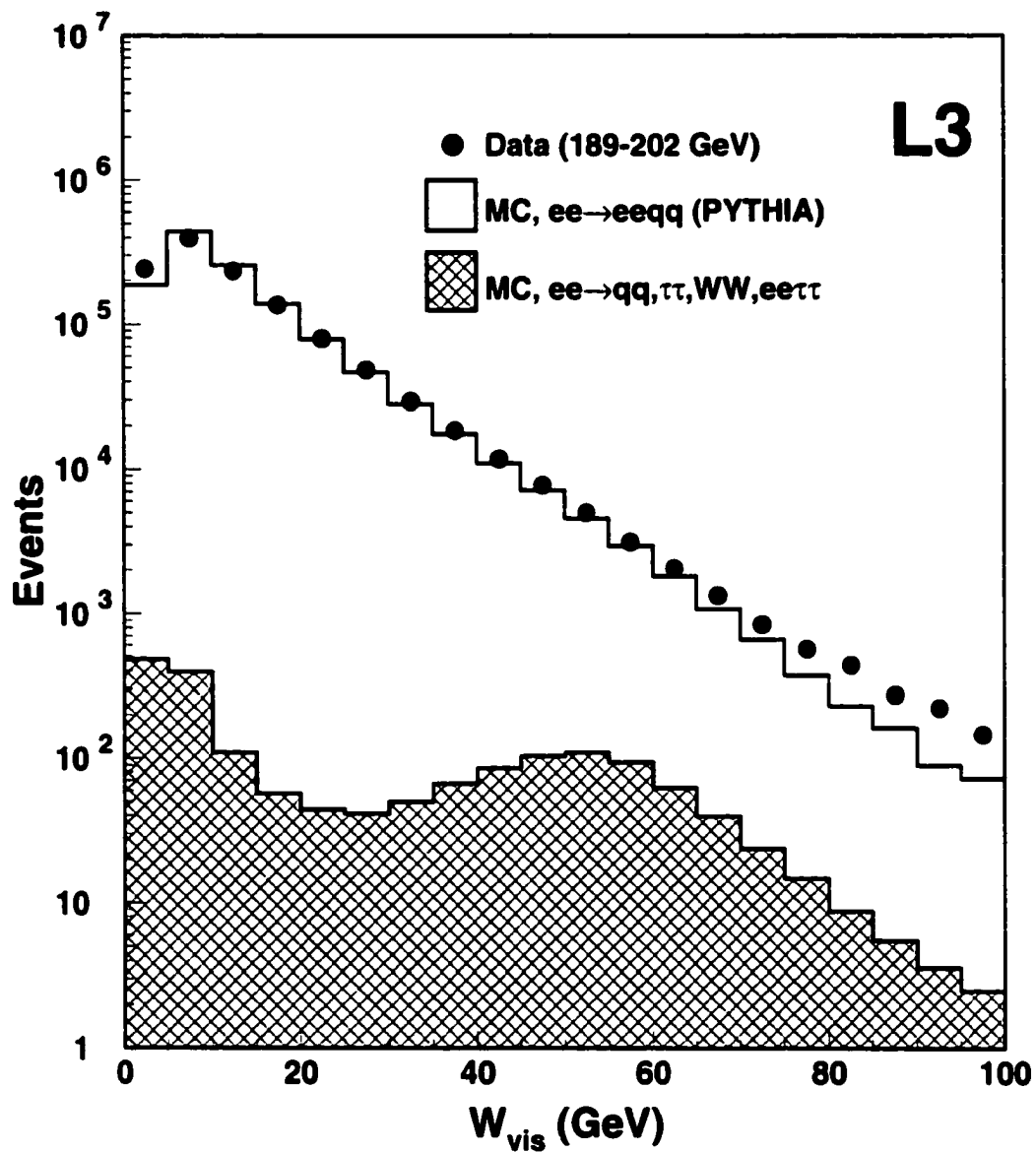


Figure 5.4: The comparison between data and Monte Carlo for the visible invariant mass, W_{vis} . The Monte Carlo distributions for signal and background have been scaled to the data luminosity.

the most energetic cluster in the luminosity monitor. Figure 5.5 shows the ratio of the energy of the most energetic cluster in the luminosity monitor to the beam energy for data and Monte Carlo expectations from PYTHIA and other backgrounds. There is a good agreement between data and Monte Carlo at lower values of E_{Lumi} . However, there is a disagreement as we go to higher values. This is because these higher values of E_{Lumi} correspond to the tagged events that the PYTHIA Monte Carlo is unable to generate. The two bumps in the data at around 0.65 and 0.95 are due to off momentum electrons and single tag two-photon events. Off momentum electrons are those electrons in the beam that are deflected due to the presence of magnetic field. After selecting two-photon events, the next step is to identify a lepton (e or μ) that could be produced from the semi-leptonic decay of a heavy (c or b) quark. The next two sections deal separately with electrons and muons.

5.2 Electron Selection

In this section, the electron selection will be discussed. In general nine different cuts are applied in order to enhance the fraction of the event sample that contains an electron from heavy quark decay. These cuts are listed in Table 5.1 and their effects are described below. The cut thresholds are chosen by minimizing the uncertainty on the cross section. This task is achieved by calculating two quantities called the *purity* and the *efficiency*. They are defined in the following chapter.

Figure 5.6 shows the distribution for the momentum of the electron. In this plot, the charm fraction of the Monte Carlo is scaled to the measured cross section [32]. There is an excess of data at higher momentum values.

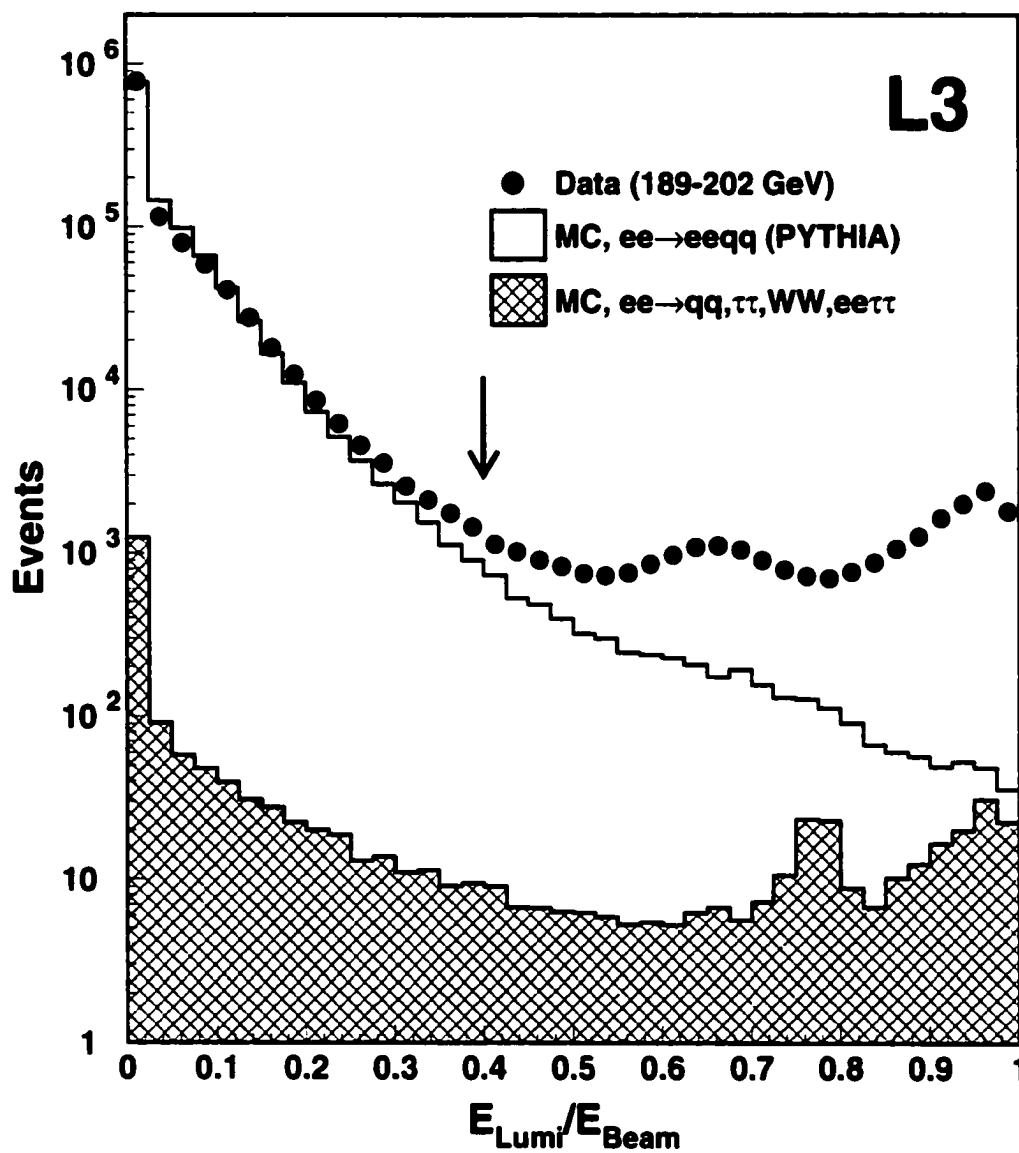


Figure 5.5: The $N - 1$ plot of the ratio of the energy of the most energetic cluster in the luminosity monitor to the beam energy. A cut of $E_{Lumi} < 0.4E_{Beam}$ is aimed at selecting untagged hadronic two photon events. There is a good agreement between data and PYTHIA Monte Carlo below $0.4E_{Beam}$.

Table 5.1: Cuts for the electron selection.

Variable	Cut
p	$> 2 \text{ GeV}$
$ \cos \theta $	< 0.725
$ \Delta\varphi $	$< 20 \text{ mrad}$
χ^2	< 3
$ \text{DCA} $	$< 0.5 \text{ mm}$
E_1/E_9	> 0.5
E_9/E_{25}	> 0.95
E_t/p_t	$> 1 - 2\sigma$
E_t/p_t	$< 1 + 2\sigma$
$M_{e^+e^-}$	$> 0.1 \text{ GeV}$

This discrepancy is due to the bottom fraction in the data since electrons from b decay are more energetic. Therefore in order to enrich the b fraction of the data sample, only electrons with a momentum greater than 2 GeV are selected. Figure 5.7 illustrates how the b fraction increases for higher momentum values.

Electrons will lose all their energy in the ECAL (see chapter 3) by producing electromagnetic showers. Therefore, one expects the ratio of E/P of the electrons to be centered at 1, where E and P are the energy and momentum of the electron measured in the ECAL and TEC respectively. The TEC measures transverse momentum very well by the curvature of the track. The total momentum involves the polar angle that the TEC measures less well. It is more useful to use the transverse momentum (P_t) instead. Therefore instead of E/P , the cut is applied to E_t/P_t where E_t is the transverse component of the energy released in the ECAL. Figure 5.8 shows the distribution of E_t/P_t at the $N - 1$ level. In this plot and the following ones, the data

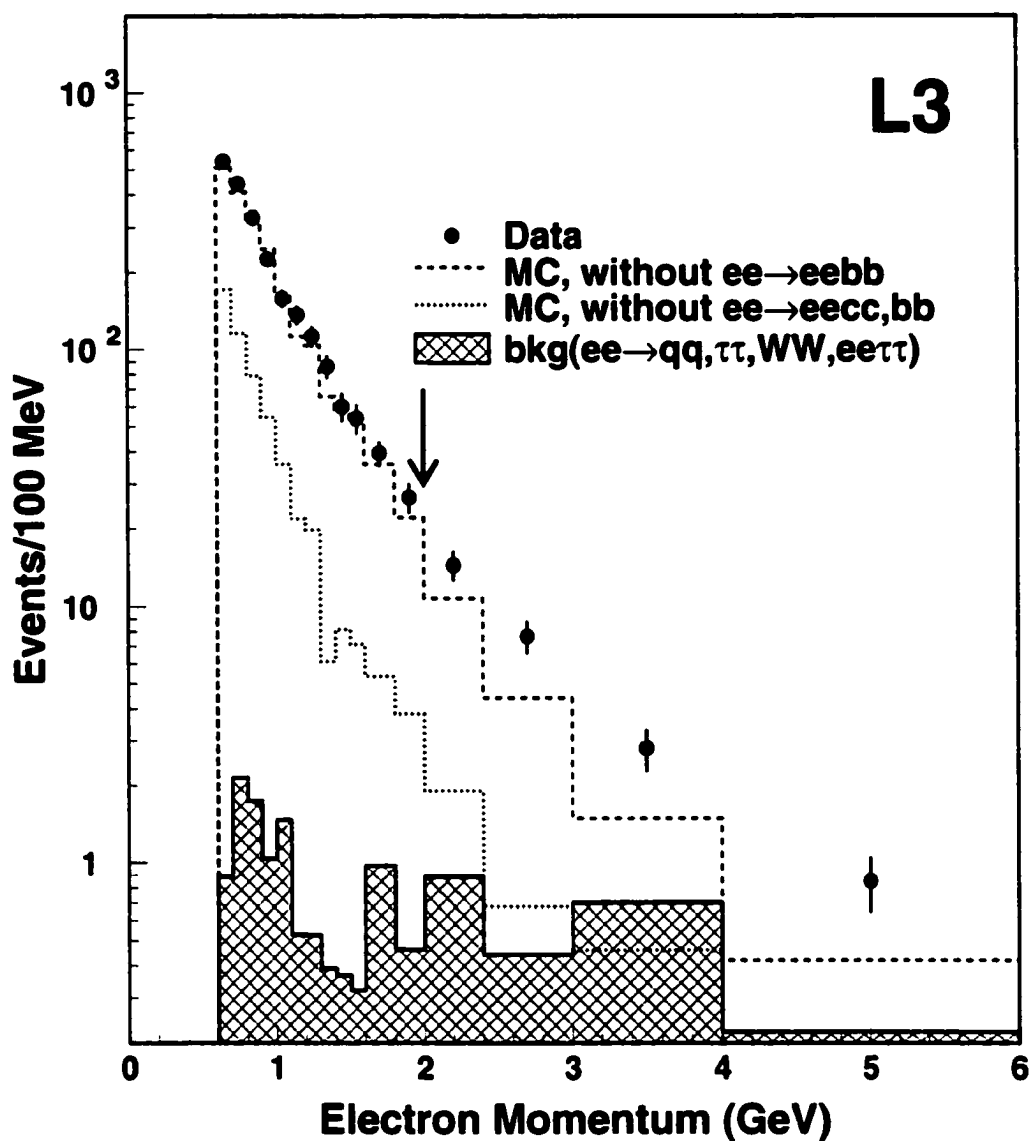


Figure 5.6: The momentum distribution of the electron candidates starting from 0.6 GeV. There is a remarkable agreement between data and Monte Carlo up to 2 GeV. The higher number of data events at higher momentums is due to the bottom fraction.

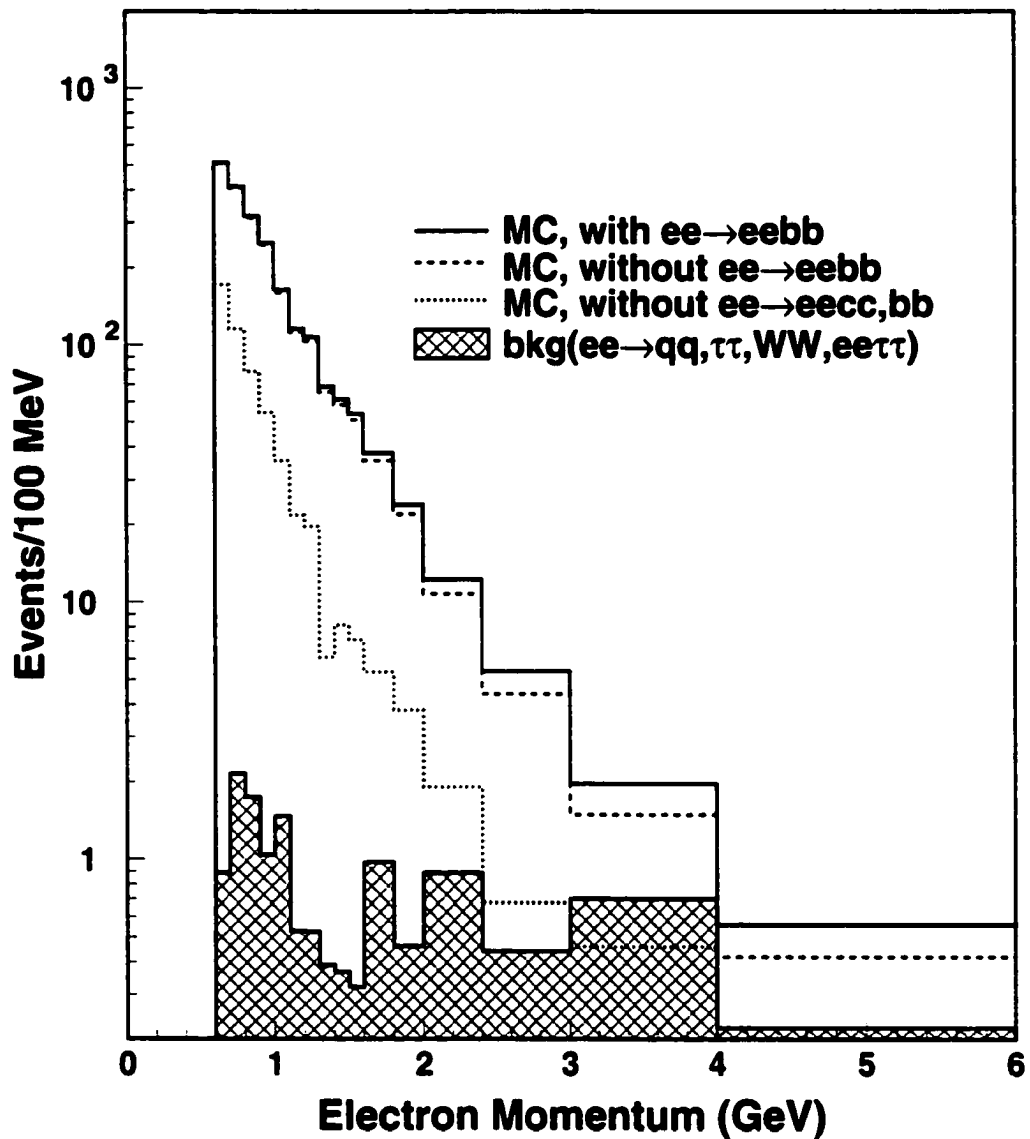


Figure 5.7: The Monte Carlo distributions for the momentum of the electron candidates. The bottom fraction increases for higher momentums.

distribution is compared with the PYTHIA Monte Carlo. The Monte Carlo is scaled to the same number of events in the data and the relative fractions of the different quark flavors are kept as generated in PYTHIA. Therefore, the agreement between data and Monte Carlo may not seem perfect for some distributions. However, the plots can be used to justify the value taken for the particular cut. The peak in Figure 5.8 around 1 is due to electrons. The electron candidates can be separated by requiring E_t/P_t to be greater than $1 - 2\sigma$ and less than $1 + 2\sigma$ where σ is the resolution of this variable. The resolution is slightly different for data and Monte Carlo simulation. The resolution is derived by fitting the electron peak with a Gaussian curve and the width σ is 0.054 and 0.046 for data and Monte Carlo respectively. To reduce systematic errors we used a cut based on σ rather than a specific range on E_t/P_t .

The TEC resolution decreases for polar angles less than 35° . This is because as tracks enter the endcap region they make smaller number of hits in the TEC (shorter track) which in turn increases the uncertainty on their momentum. This analysis is therefore restricted to the fiducial region of $|\cos\theta| < 0.725$. This corresponds to the barrel region of the L3 detector. Figure 5.9 shows the comparison between the data and Monte Carlo for the cosine of the polar angle of the electron candidate. The dip in the bin 0.7 to 0.8 is due to the gap region between the barrel and endcap ECAL. The good agreement indicates that the kinematics of heavy flavor decays are properly simulated by the PYTHIA Monte Carlo.

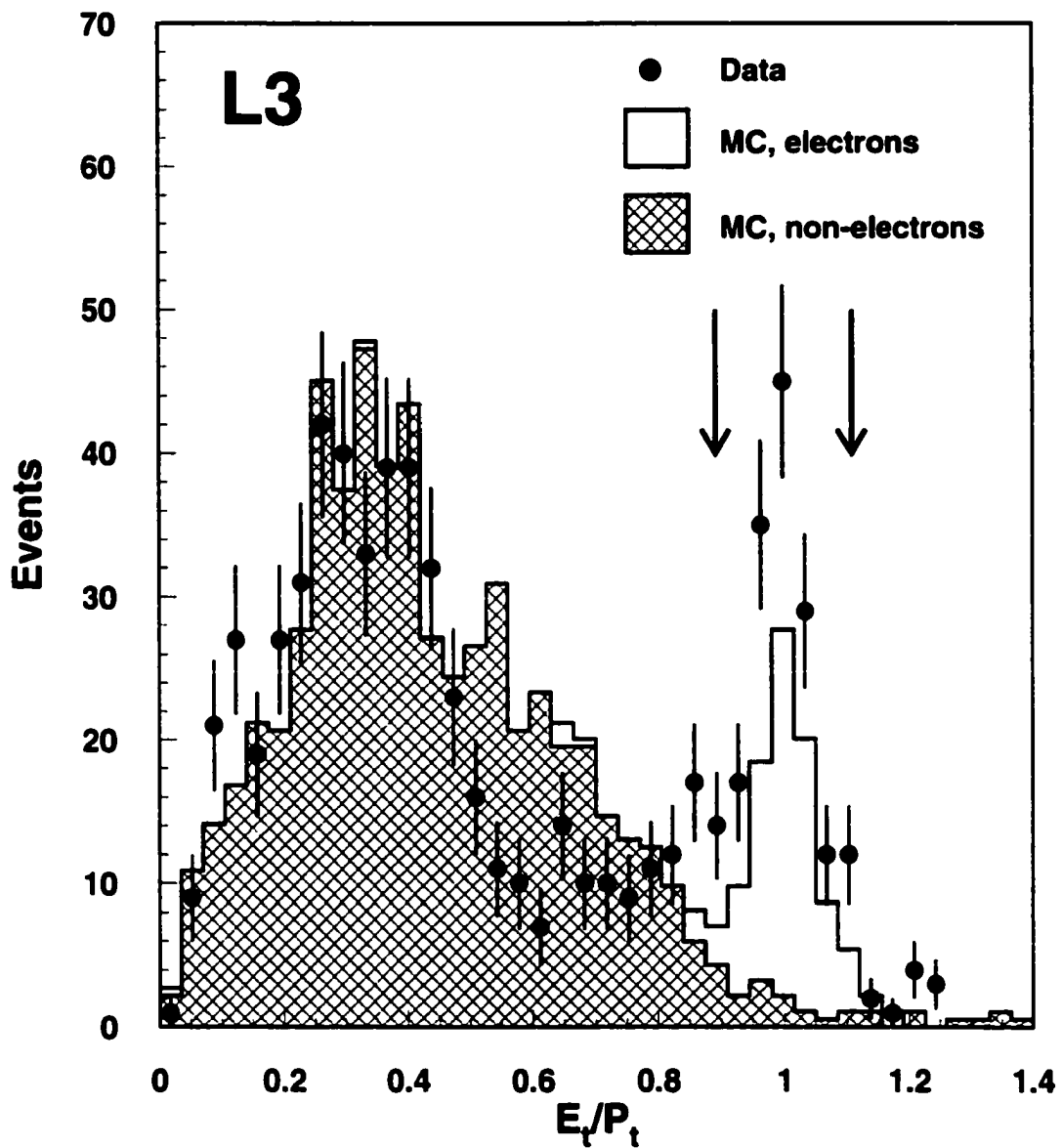


Figure 5.8: This plot shows the distributions of the ratio of the transverse energy of the electron (in ECAL) to its transverse momentum (in TEC). There are two distinctive peaks which are due to electrons and non-electrons. The peak around 1 is produced by electrons. The arrows indicate the cut values for the data.

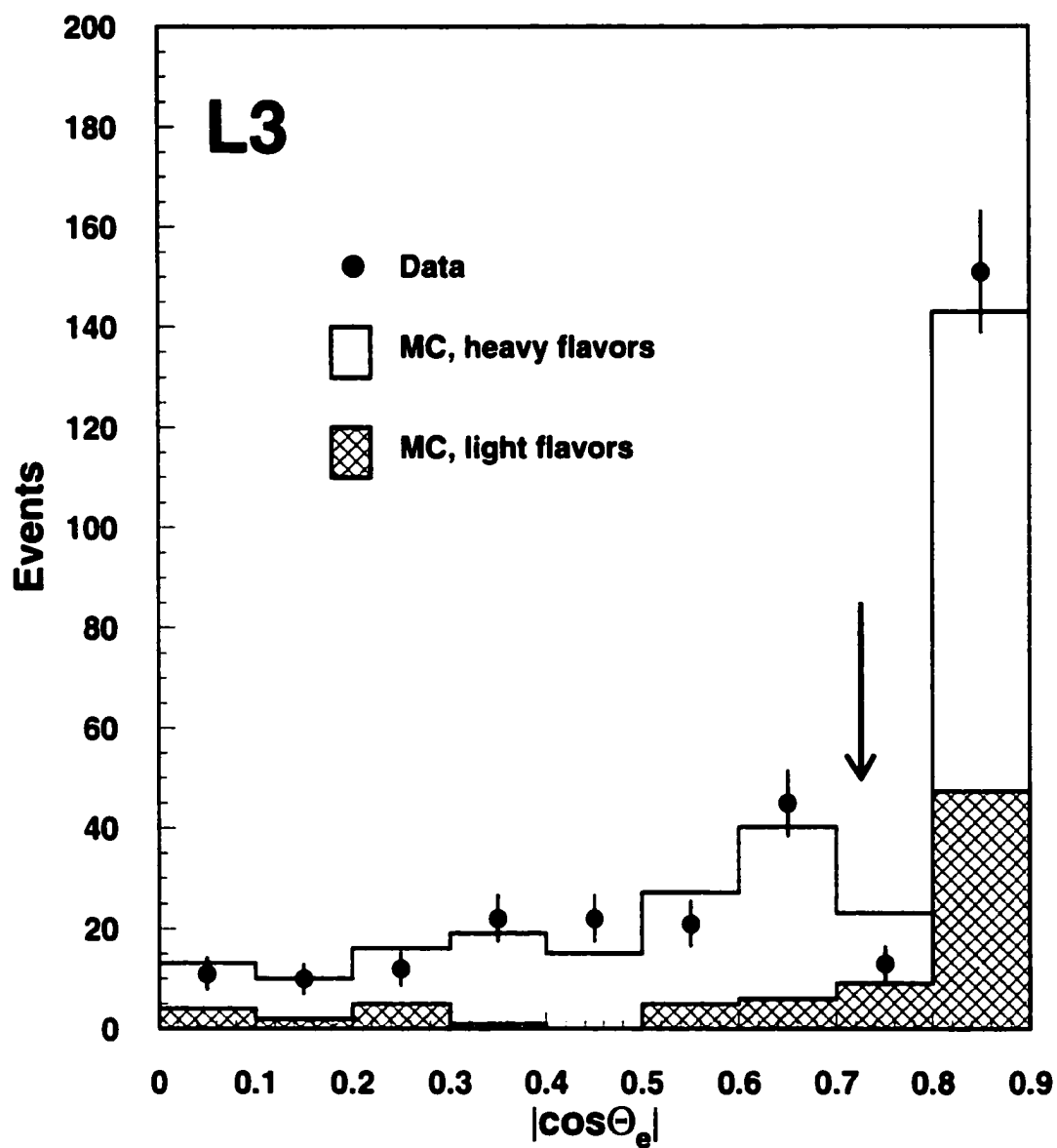


Figure 5.9: The polar angular distribution of the electron candidate. All other cuts have been applied. Electron candidates are selected which have $|\cos\theta| < 0.725$.

The electromagnetic showers produced by electrons and photons are distinctive from those of hadrons or muons. The electron and photon electromagnetic showers are more narrower (Figure 5.10).

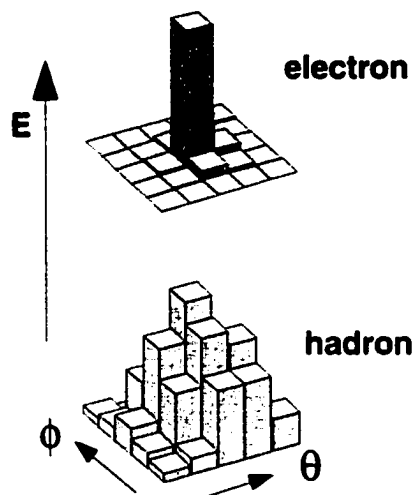


Figure 5.10: The electromagnetic shower produced by an electron is compared to that of a hadron. In this plot each square represents the end face of a BGO crystal and the height of each cube corresponds to the amount of energy deposited in that crystal. A 5×5 crystal array around the cluster barycenter is shown. The showers produced by electrons are narrower.

This qualitative feature is utilized to define some shower shape variables (for the ECAL). These variables are then used to select electrons. Three of these variables were mentioned in chapter 4 (section 4.2.2): E_1/E_9 , E_9/E_{25} and χ^2 . E_1/E_9 is the ratio of the energy deposited in the central crystal to that of the 9 crystals around the cluster barycenter. Similarly, E_9/E_{25} is the ratio of energies in the 9 and 25 crystals around the cluster barycenter. Since electron showers are more confined, one would expect that the values of E_1/E_9 and

E_9/E_{25} be closer to 1 for electrons than for hadrons. One can also produce a statistical analysis of the deposits in the crystals for a shower and produce a χ^2 fit to the shape expected for an electron with that energy. The χ^2 for electromagnetic showers would be lower than for non-electrons.

Figures 5.11-5.13 show the distributions of these three shower shape variables.

The electron selection process is based on information from both the TEC and the ECAL. The electron candidates from heavy flavor decays produce a track in the TEC and subsequently make a shower in the ECAL. Therefore, these electron candidates should have a TEC track which is matched to an ECAL shower. The variable which is a measure of difference in the azimuthal angles of the shower barycenter and the track impact point at the ECAL is called the matching accuracy. Pions are produced copiously in two-photon interactions. Neutral pions will decay to photons, $\pi^0 \rightarrow \gamma\gamma$. It is possible that a photon from a π^0 decay will overlap with a π^\pm . In this case the photon electromagnetic shower and the charged pion's track can mimic an electron candidate from a heavy flavor decay. This background can be reduced by applying a cut on the matching accuracy (Figure 5.14).

Another background comes from conversion of high energy photons in the material of the beam pipe and inner tracking detector. These photons can produce electrons as a result of $\gamma \rightarrow e^+e^-$. The fraction of the electrons from a heavy flavor decay can be increased by reducing this background. A cut on the distance of closest approach (DCA) of the electron track to the interaction point in the $r - \phi$ plane, increases this fraction. Figure 5.15

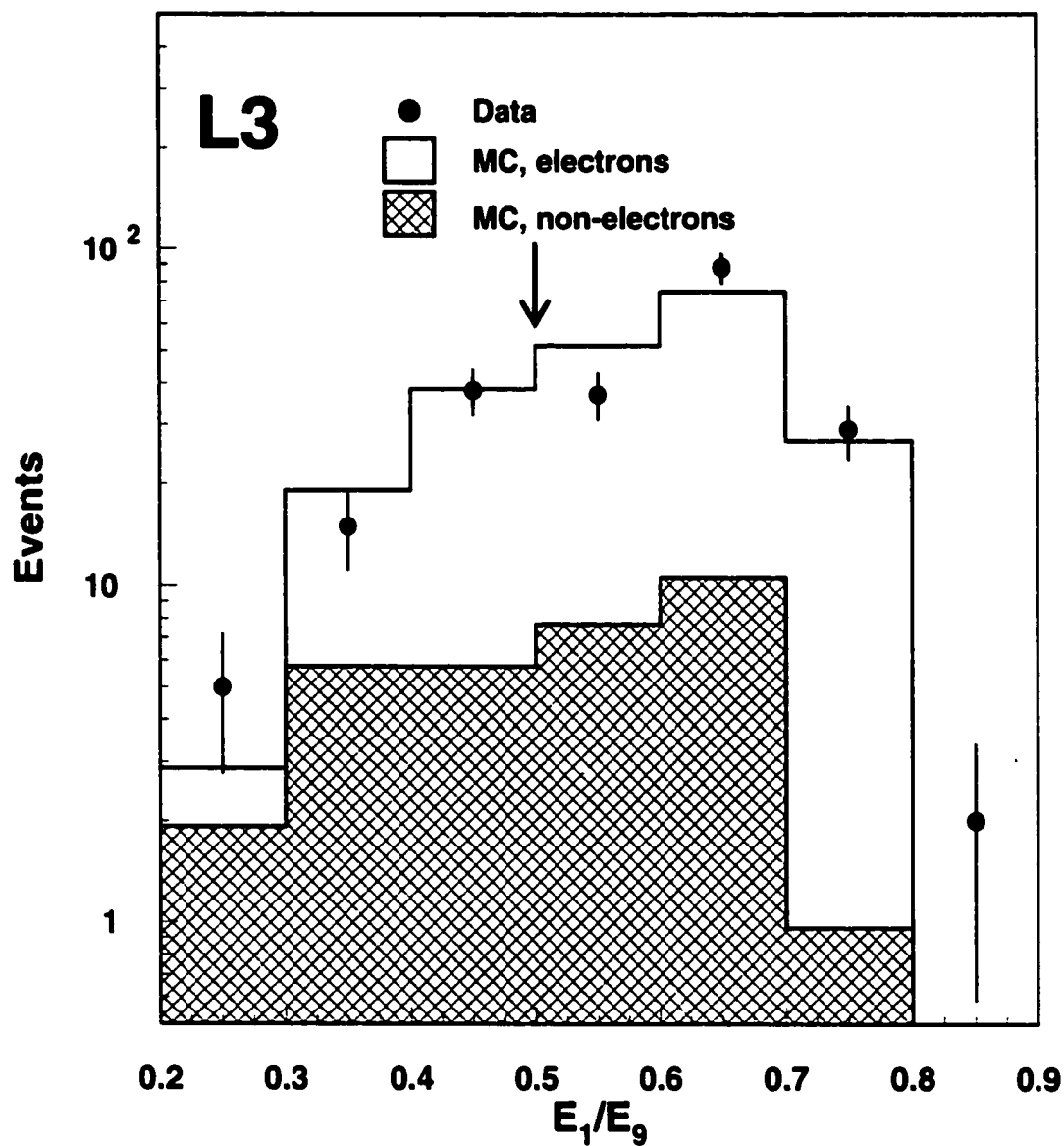


Figure 5.11: This plot shows the distributions of the shower shape variable E_1/E_9 for electrons and non electrons. The electron fraction of the sample increases for higher values of E_1/E_9 .

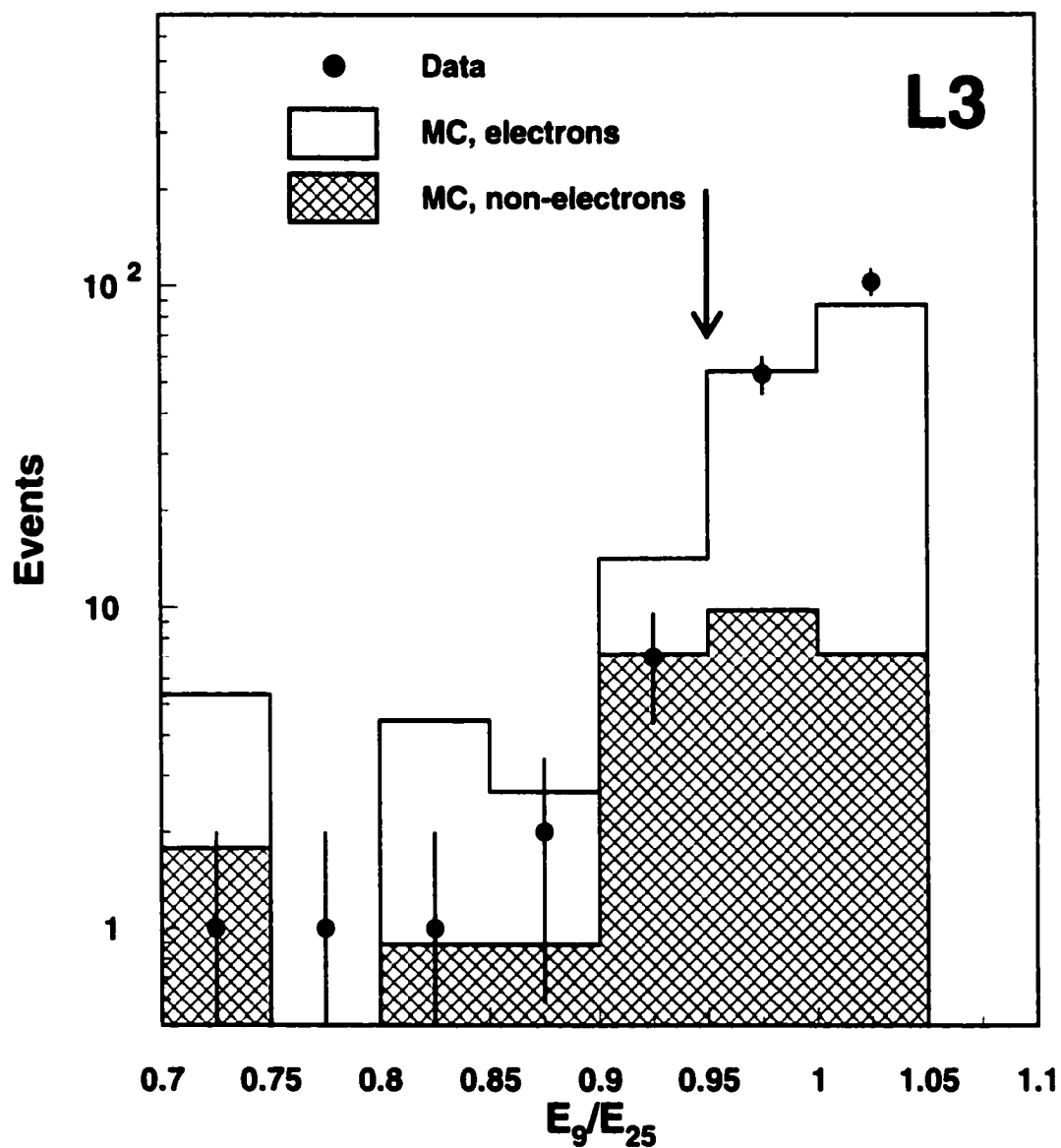


Figure 5.12: This plot illustrates the distributions of the shower shape variable E_9/E_{25} for electrons and non electrons. A cut is applied at 0.95 in order to increase the electron fraction in the data sample.

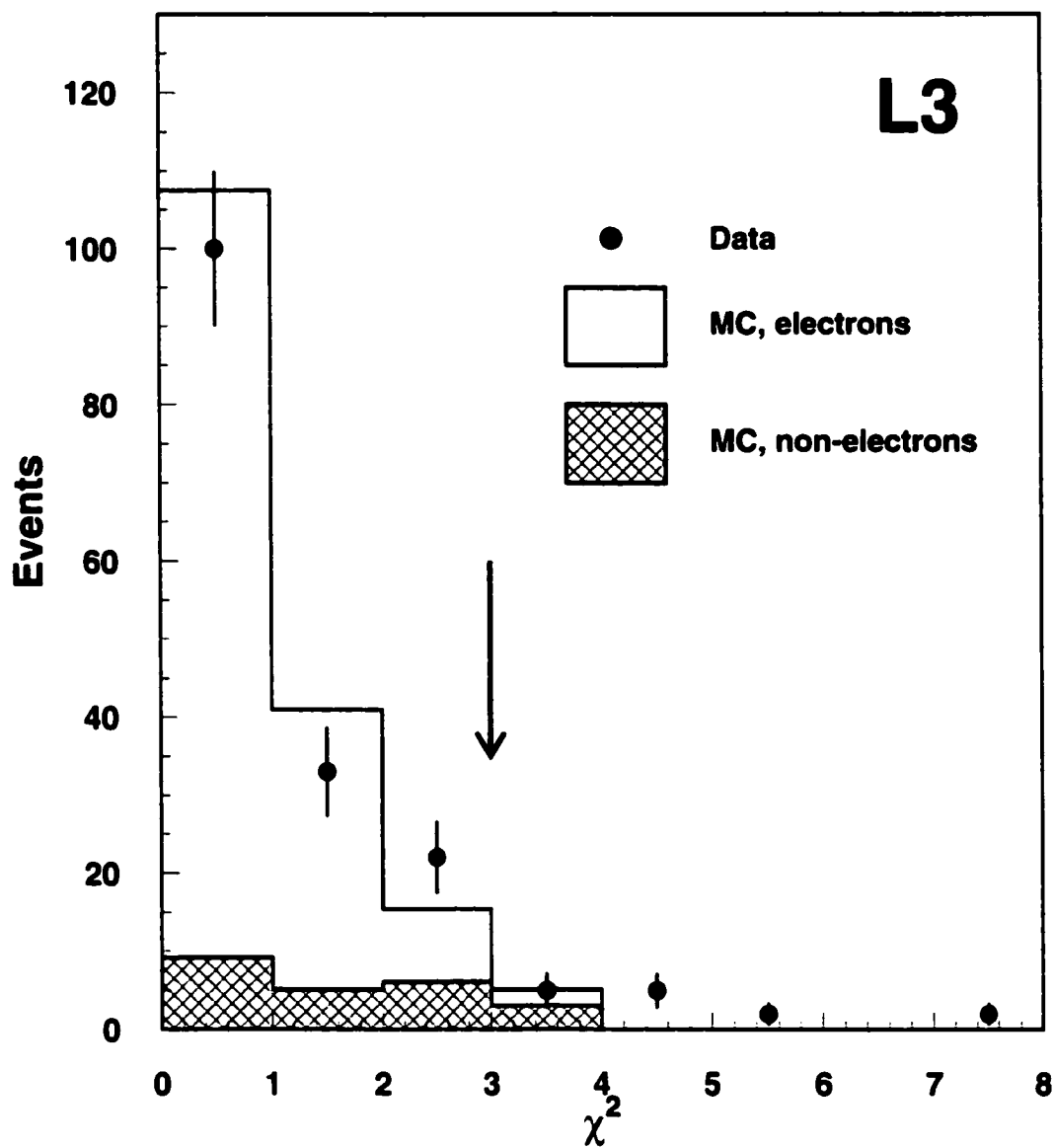


Figure 5.13: This figure depicts the χ^2 distributions of electrons and non electrons. The χ^2 is calculated by comparing the shower shape with that of an electromagnetic shower. Electrons have a smaller χ^2 .

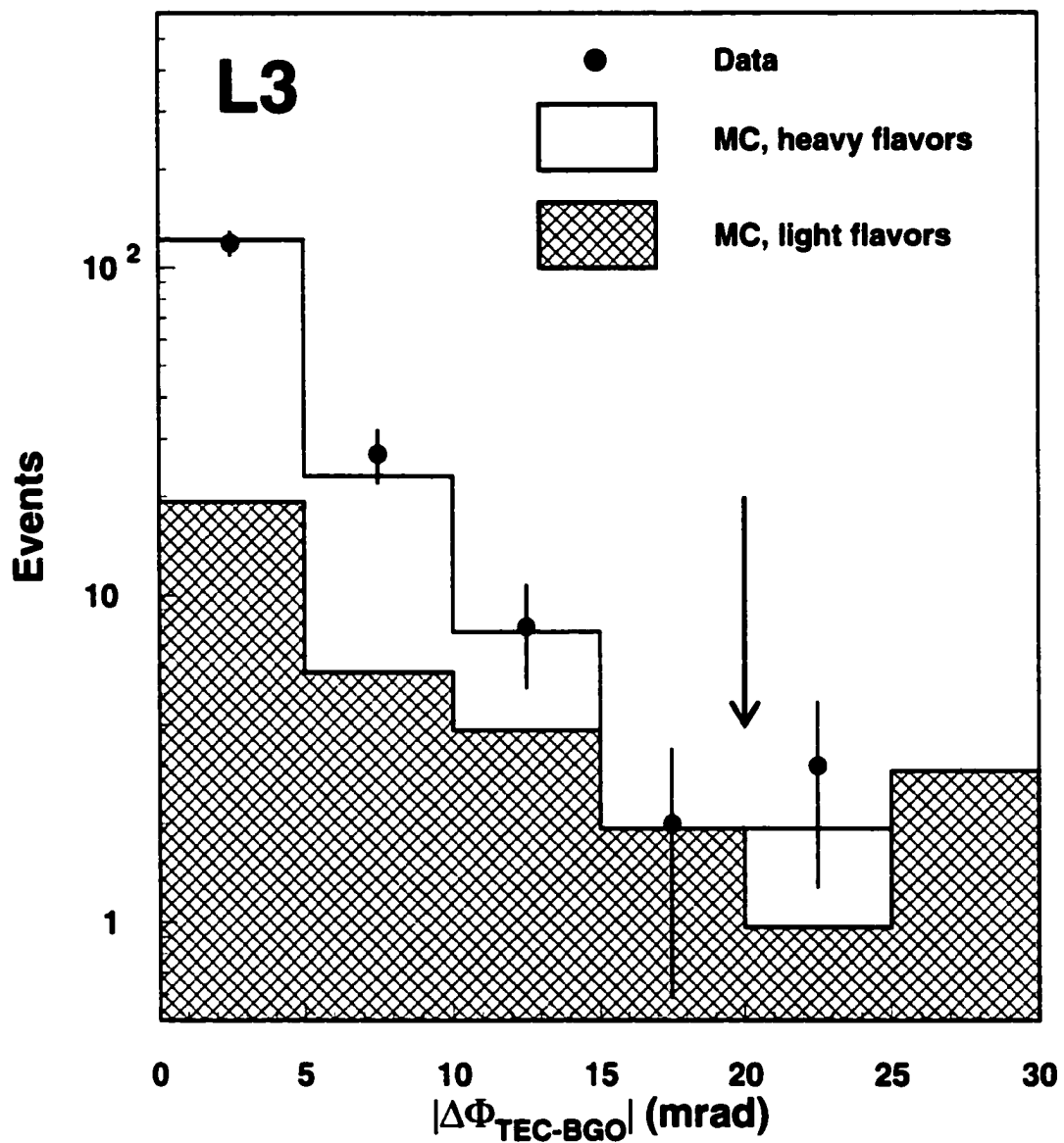


Figure 5.14: The angular difference of the azimuthal angle of the projection of the TEC track at the ECAL and its corresponding shower position in the ECAL. A cut is applied on this variable to select candidates with good matching accuracy.

depicts the distribution of this variable.

In order to further reduce the electrons from photon conversions, a cut can be applied on the invariant mass of the electron candidate and its closest track ($M_{e^+e^-}$). If the electron candidate comes from a photon conversion, its closest track will be its antiparticle and their invariant mass will be very small since photons have no mass. Therefore by selecting events with higher $M_{e^+e^-}$, one can reduce the fraction of these electrons even further.

After applying all these cuts, 156 events remain. The background from annihilation processes and two-photon production of tau pairs is estimated to be 4.7%. One of the candidate events which satisfies all the above cuts is depicted in Figure 5.16 (xz plane). Figure 5.17 is the same event shown in the xy plane. The electron candidate in this event has a momentum of 5.1 GeV and a polar angle of 1.925 rad (it can be seen in the lower right part of Figure 5.16). The event has a small transverse imbalance which is caused primarily by the undetected neutrino. The longitudinal imbalance is higher which is typical for two-photon events since the two photons usually have different energies. The high momentum of this electron candidate along with the high visible mass of the event make it likely to be from a b quark decay.

5.3 Muon Selection

In order to select muon candidates, three different cuts are utilized. These cuts and their thresholds are listed in Table 5.2.

The muon candidates are detected in the muon chambers. Muon chambers are the outermost portion of the L3 detector. Therefore muon candidates have to pass through all the other subdetectors in order to be detected. Only

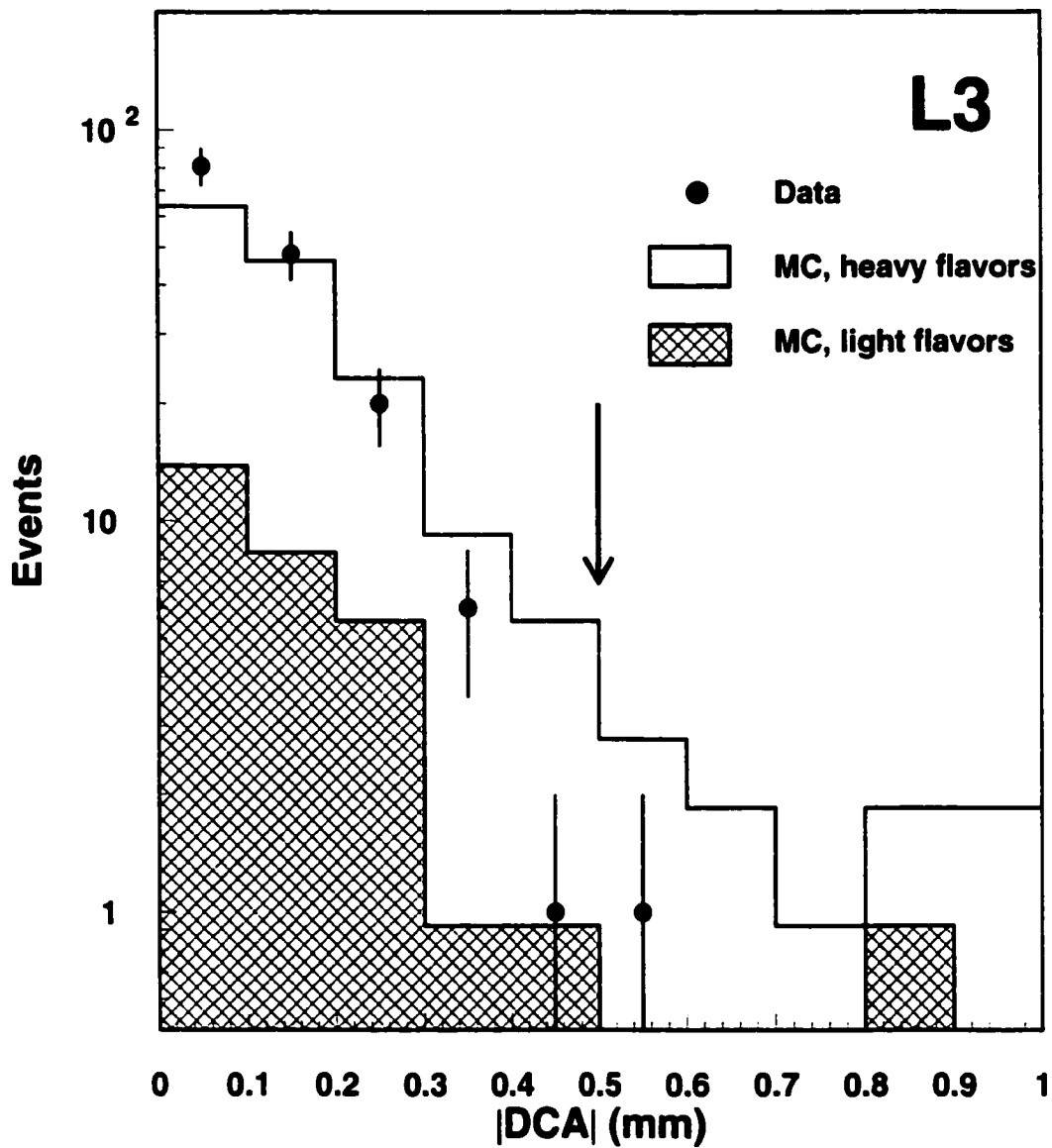


Figure 5.15: Distribution of the distance of closest approach of the TEC track to the beam line in the $r - \phi$ plane. The contributions from heavy and light flavor quarks are shown.

Run # 777104 Event # 1256 Total Energy : 37.66 GeV

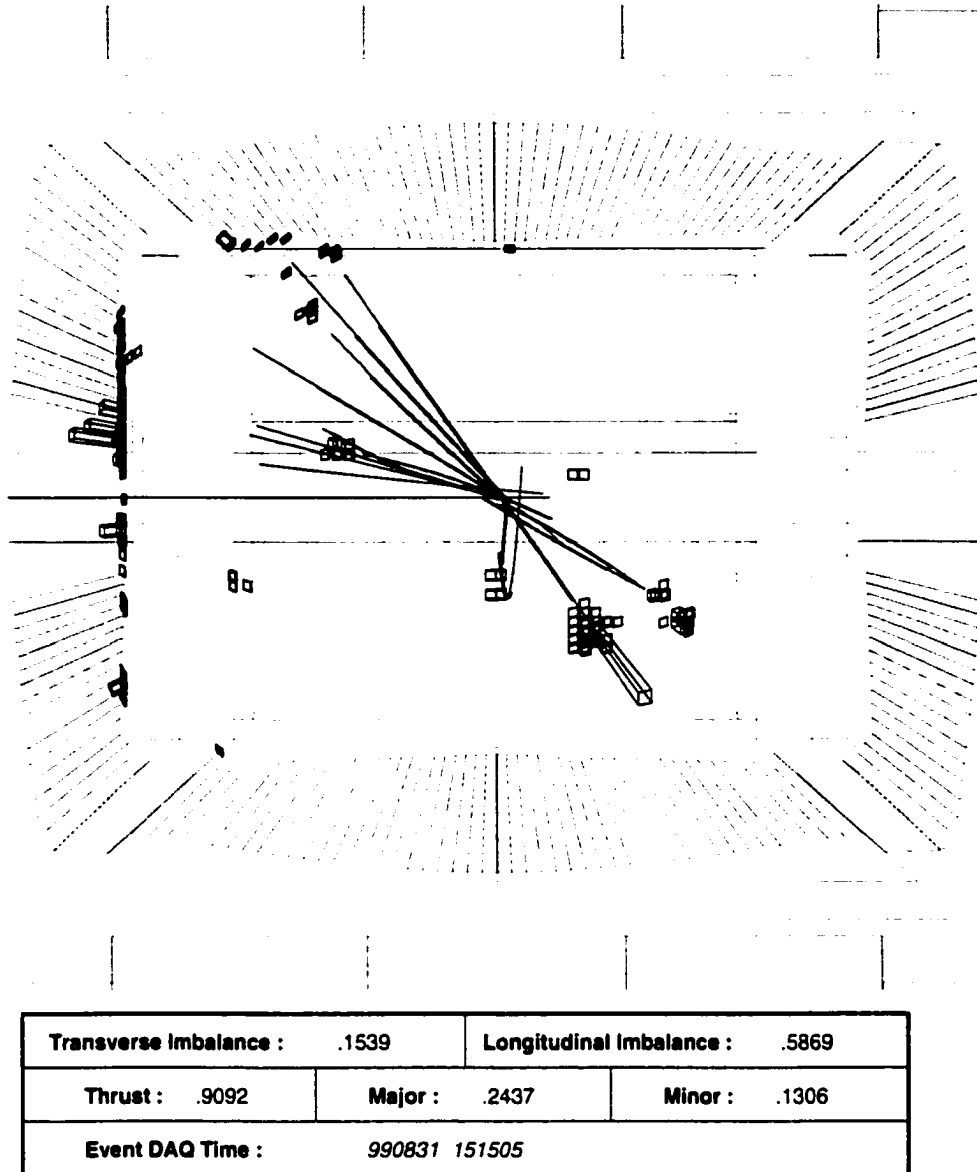


Figure 5.16: An event with an electron candidate viewed in the xz plane. The electron candidate is the larger tower in the lower right hand corner.

Run # 777104 Event # 1256 Total Energy : 37.66 GeV

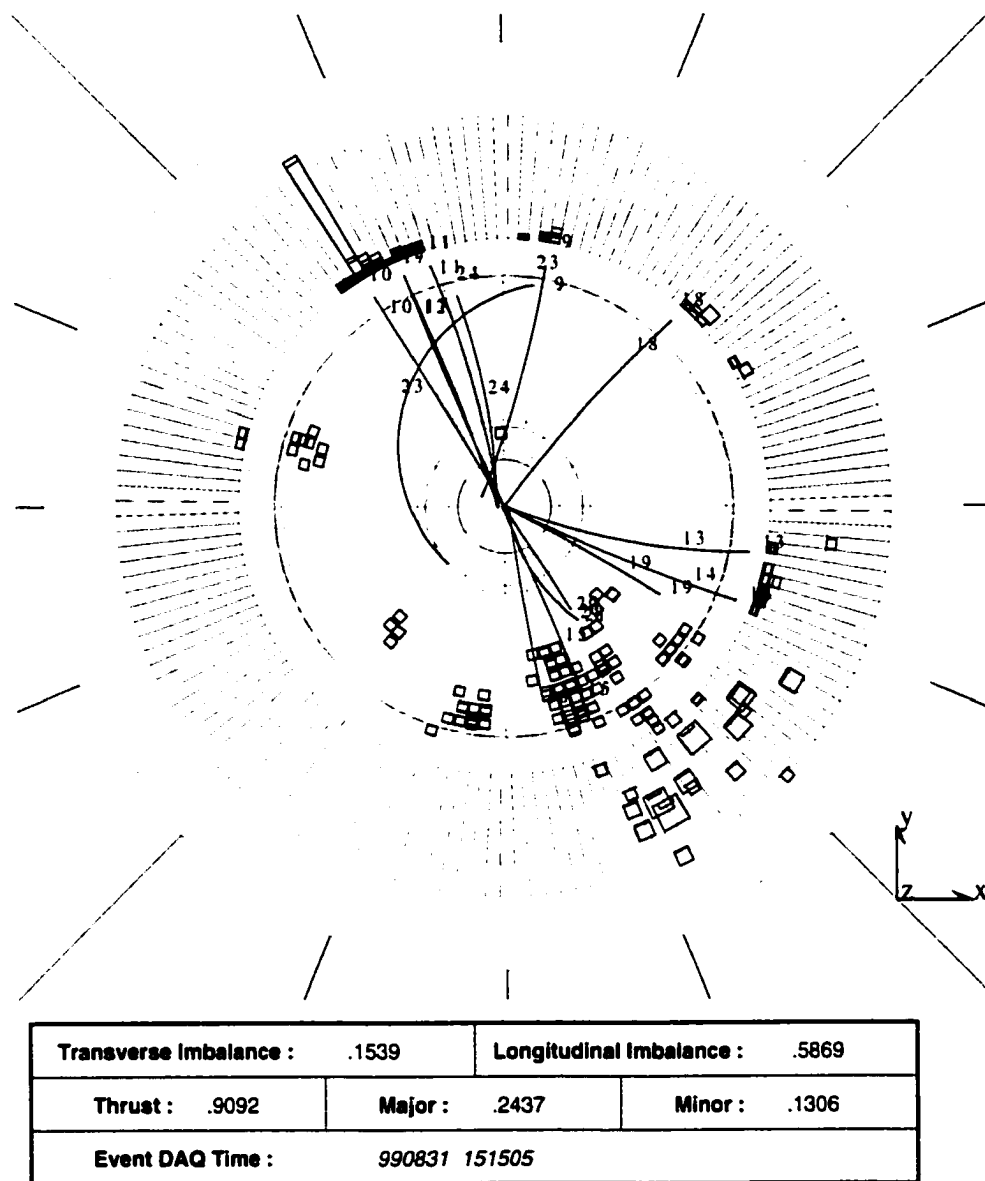


Figure 5.17: An event with an electron candidate viewed in the xy plane. The electron candidate is at $\phi = 120^\circ$.

Table 5.2: Cuts for the muon selection.

Variable	Cut
p	> 2.0 GeV
p	< 0.1 \sqrt{s}
$ \cos \theta $	< 0.8

muons that have a momentum greater than 2 GeV can satisfy this condition. Consequently, we require the muon candidates to have a momentum greater than 2 GeV.

A number of muons that reach the muon chambers are produced by pion and kaon decays in the calorimeters ($\pi^\pm \rightarrow \mu^\pm \nu_\mu$ and $K^\pm \rightarrow \mu^\pm \nu_\mu$). In order to reject these muons, we require the muon candidate in the muon chamber to be matched to a track in the TEC. This requirement will ensure that the muon is produced near the interaction point and therefore it will have the likelihood to be from a heavy flavor decay. Another source of background muons are the cosmic ray muons. These muons can be removed from the data sample by accepting events that have scintillator hits within ± 5 ns of the beam crossing time.

Muons from annihilation events are very energetic. Figure 5.18 shows that the fraction of these events increases at higher momentums. These background events can be suppressed by requiring the muon momentum to be less than $0.1\sqrt{s}$.

Muons are selected in the angular range $|\cos\theta| < 0.8$ since the resolution of the momentum measurement worsens for smaller polar angles. Figure 5.19 shows the cosine of the polar angle of the muon candidate for data and Monte

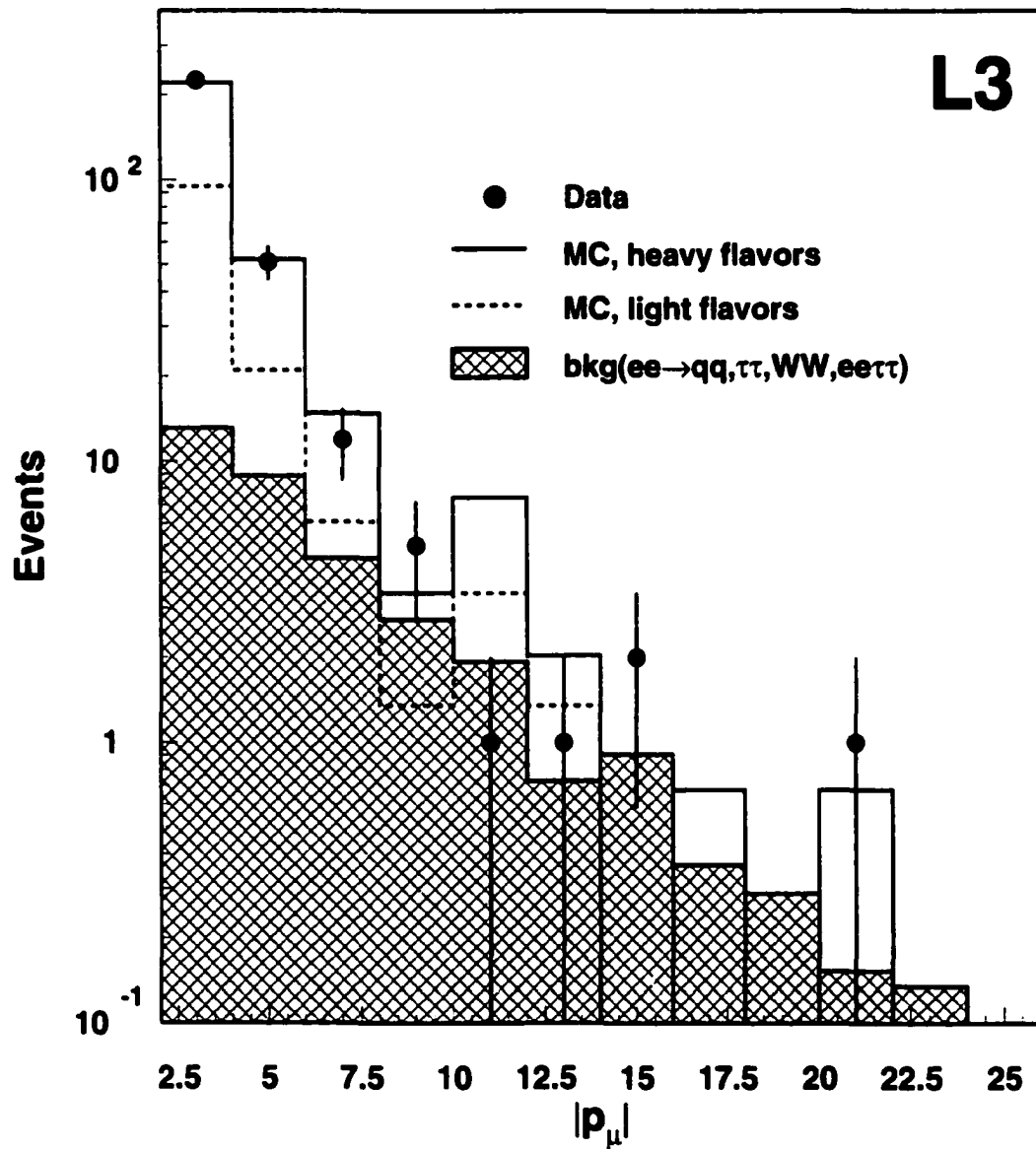


Figure 5.18: The momentum of the muon candidates. There is a good agreement between data and Monte Carlo.

Carlo. There is good agreement between data and Monte Carlo. In this plot, similar to the electron ones, the Monte Carlo is scaled to the same number of events in the data and the quark fractions are kept as in PYTHIA. The agreement between the data and Monte Carlo implies that the kinematic simulation of heavy flavor decay to muon by PYTHIA is well done.

After all cuts are applied, 298 events are selected containing at least one muon candidate. The estimated background from annihilation processes and two-photon production of tau pairs is 6.0%. Figures 5.20 and 5.21 show one of these candidate events in the xz and xy planes respectively. As can be seen from these figures, the muon candidate passes through the calorimeters. It should also be noted that the longitudinal imbalance is much larger than the transverse imbalance.

In the following chapter, these selected events will be utilized for the measurement of b quark production cross section in two-photon collisions.

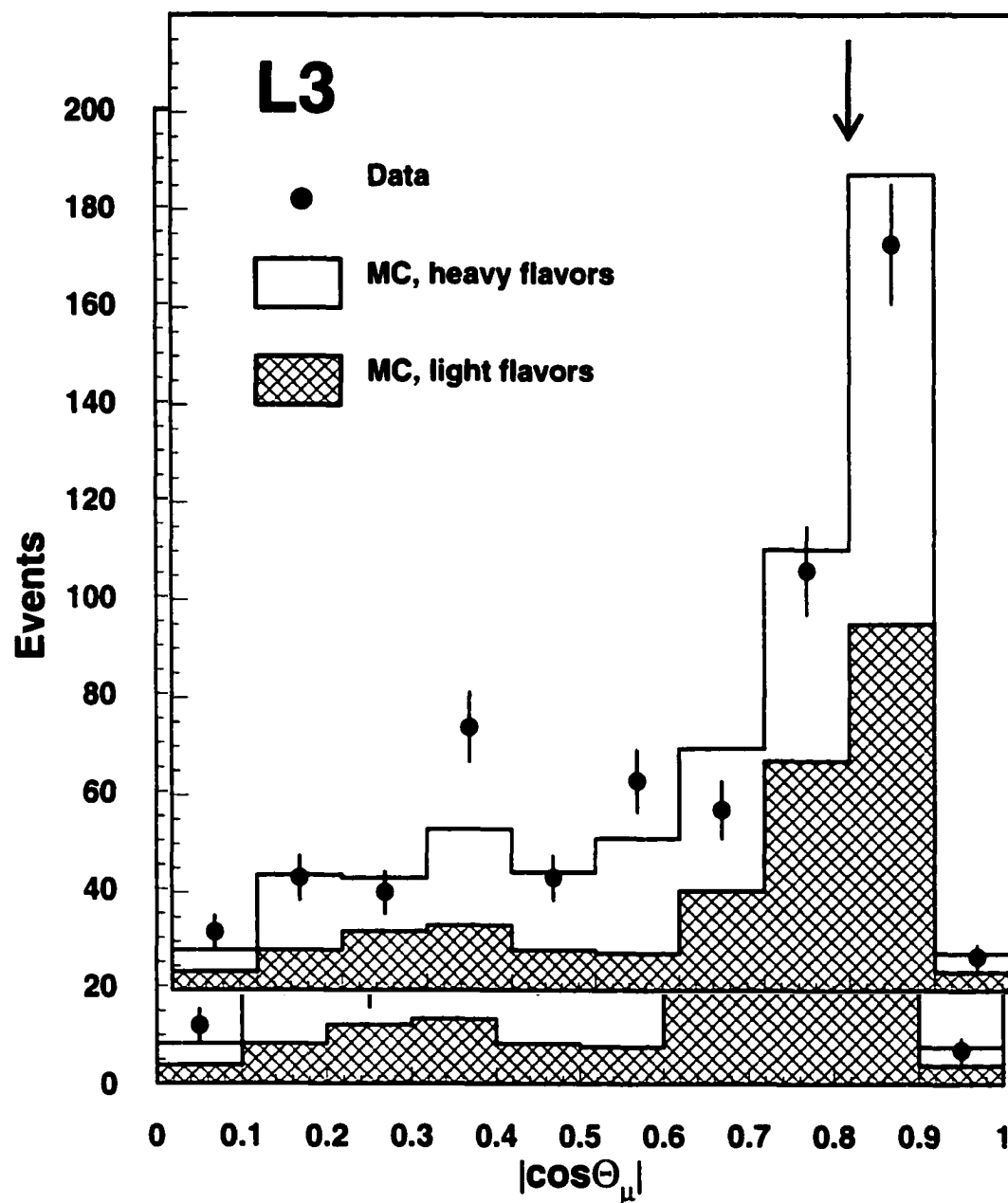
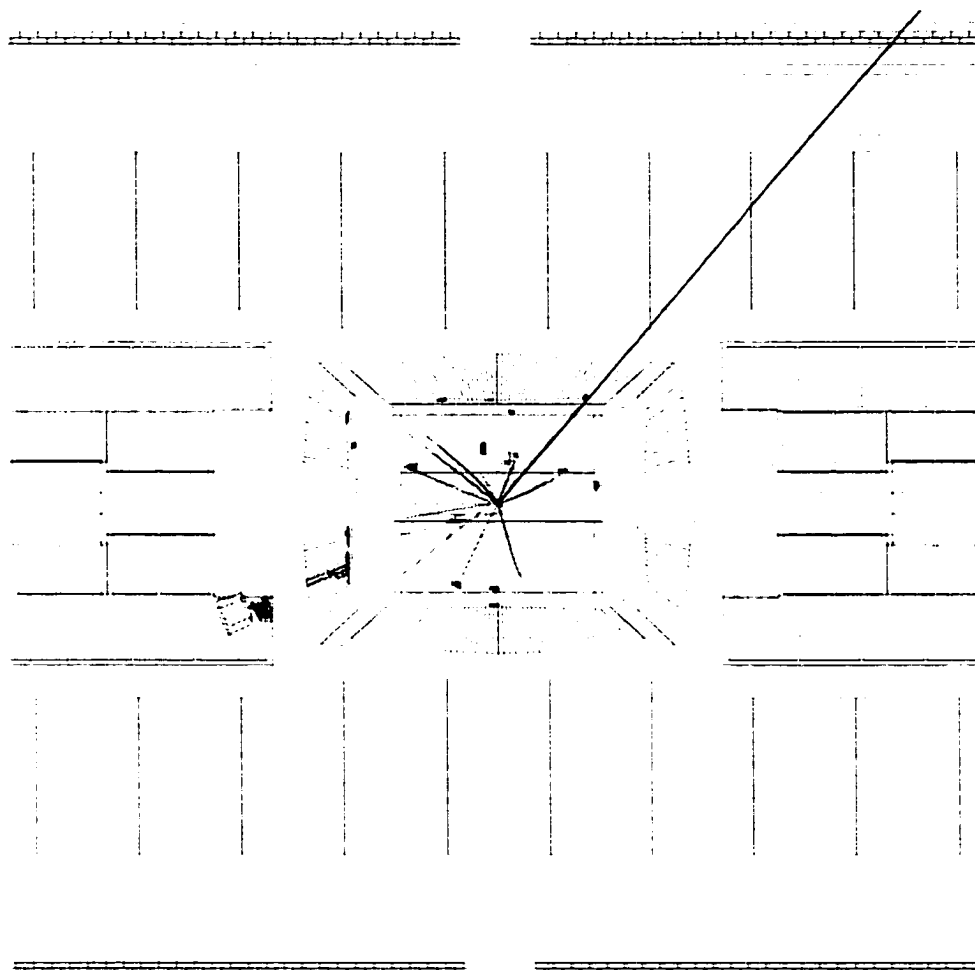


Figure 5.19: The comparison between the data and Monte Carlo for the angular distribution of the muon candidate.

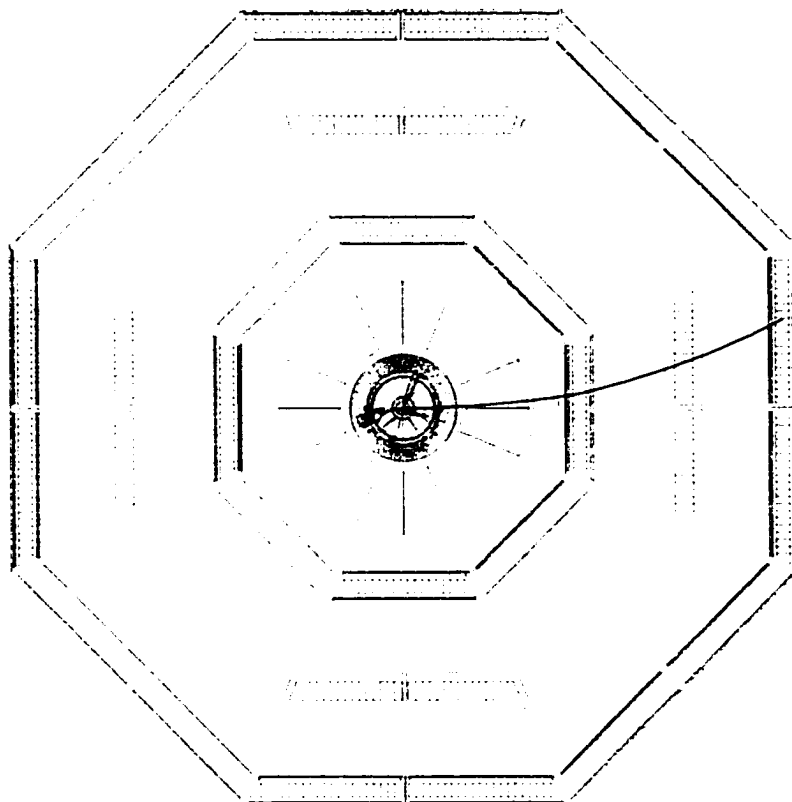
Run # 745905 Event # 3194 Total Energy : 15.65 GeV



Transverse imbalance :	.0654	Longitudinal imbalance :	.3831
Thrust :	.8569	Major :	.2820
		Minor :	.2502
Event DAQ Time :	990606 35122		

Figure 5.20: The xz view of an event with a muon candidate. The muon is seen moving through the detector toward the upper right.

Run # 745905 Event # 3194 Total Energy : 15.65 GeV



Transverse Imbalance :	.0654	Longitudinal Imbalance :	.3831		
Thrust :	.8569	Major :	.2820	Minor :	.2502
Event DAQ Time :	990606 35122				

Figure 5.21: The xy view of an event with a muon candidate. The muon has a ϕ angle near zero.

CHAPTER 6

CROSS SECTION MEASUREMENT

6.1 Jet Reconstruction

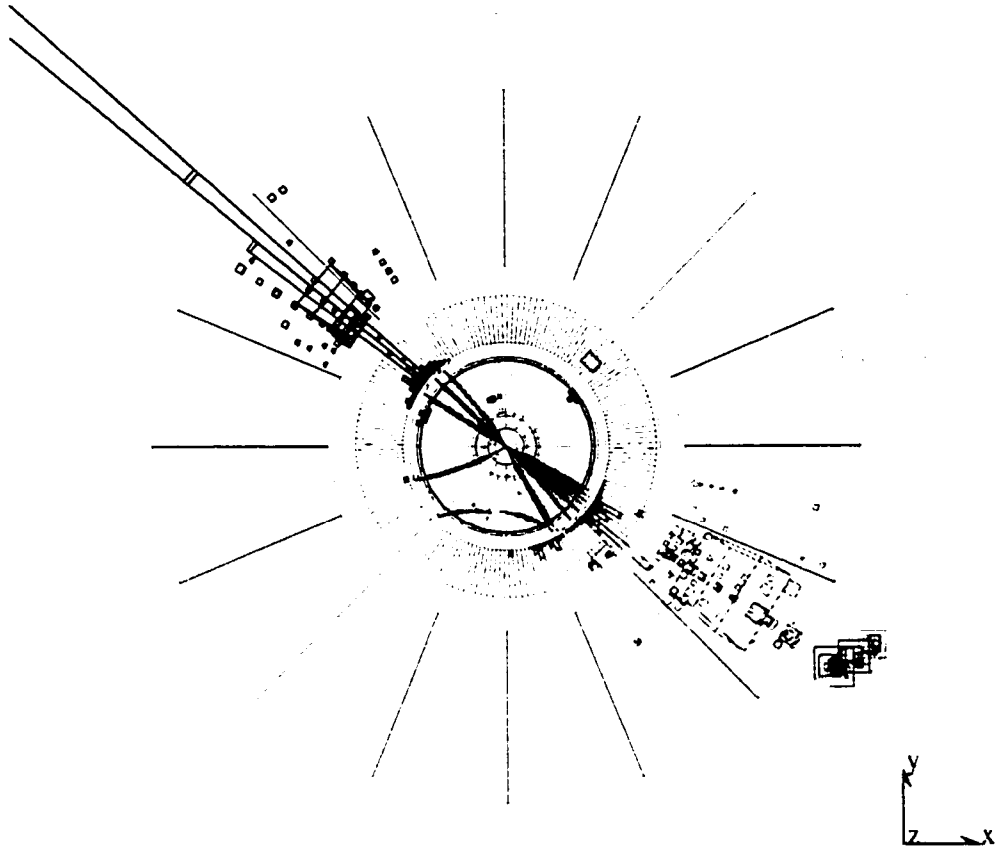
The previous chapter dealt with selecting electrons or muons which are produced in the semi-leptonic decay of a heavy quark. In this chapter we take the final sample and extract the cross section for bottom quark production. Figures 5.1 and 5.2 illustrate the event topology for semi-leptonic decays of b and c quarks. These figures show that a complete understanding of semi-leptonic decays of b and c quarks require a comprehensive definition of a jet.

There are couple different algorithms for jet definitions. As mentioned in chapter 5, jets are spray of secondary particles. These particles will produce tracks and clusters in the detector. Thus, the aim of any jet algorithm is how to group these quantities into a jet. Figure 6.1 shows a typical $e^+e^- \rightarrow q\bar{q}$ Monte Carlo event with two back to back jets. A spray of secondary particles are produced from the interaction point which in turn produce tracks and clusters. These objects can be grouped into two different jets which can be seen visually.

One of the most widely used jet algorithms is the JADE algorithm [33]. This algorithm was developed by the JADE collaboration at PETRA during 1980's. JADE jets are reconstructed by first calculating the scaled invariant mass squared of any pairs of particles (clusters) k and l in the event:

$$y_{kl} = M_{kl}^2/E_{vis}^2 \quad (6.1)$$

Run # 1860681 Event # 5004 Total Energy : 203.00 GeV



Transverse Imbalance :	.0202	Longitudinal Imbalance :	-.0345		
Thrust :	.9888	Major :	.0463	Minor :	.0543
Event DAQ Time :	800000	1			

Figure 6.1: A typical Monte Carlo $e^+e^- \rightarrow q\bar{q}$ event display. Two back to back jets are clearly visible.

where E_{vis} is the total visible energy of the event and M_{kl} is the invariant pair mass which can be calculated as:

$$M_{kl}^2 = 2E_k E_l (1 - \cos\theta_{kl}) \quad (6.2)$$

This process is repeated until all the pair masses exceed a certain threshold value, y_{cut} . The clusters that satisfy this condition are called a jet. Intuitively, y_{cut} is a parameter for defining resolvable partons. In this analysis a y_{cut} value of 0.1 is chosen. Figure 6.2 shows the comparison between data and Monte Carlo for the number of JADE jets with $y_{cut} = 0.1$. There is a good agreement between the two.

The angular distributions of the reconstructed JADE jets are depicted in Figure 6.3. This plot demonstrates that data and Monte Carlo have similar distributions for the angle of the jets.

6.2 Cross Section Calculation

6.2.1 Cut Based Method

The cross section (σ) of any particular interaction is a measure of the probability for the occurrence of that interaction. The relationship between the number of events, luminosity and the cross section is given by Eq. 3.2. This equation assumes:

- the detector is able to detect all the desired events,
- the selection procedure can select all the desired events
- and the data sample does not contain any other type of events.

For the experimental measurement of the cross section, Eq. 3.2 has to be

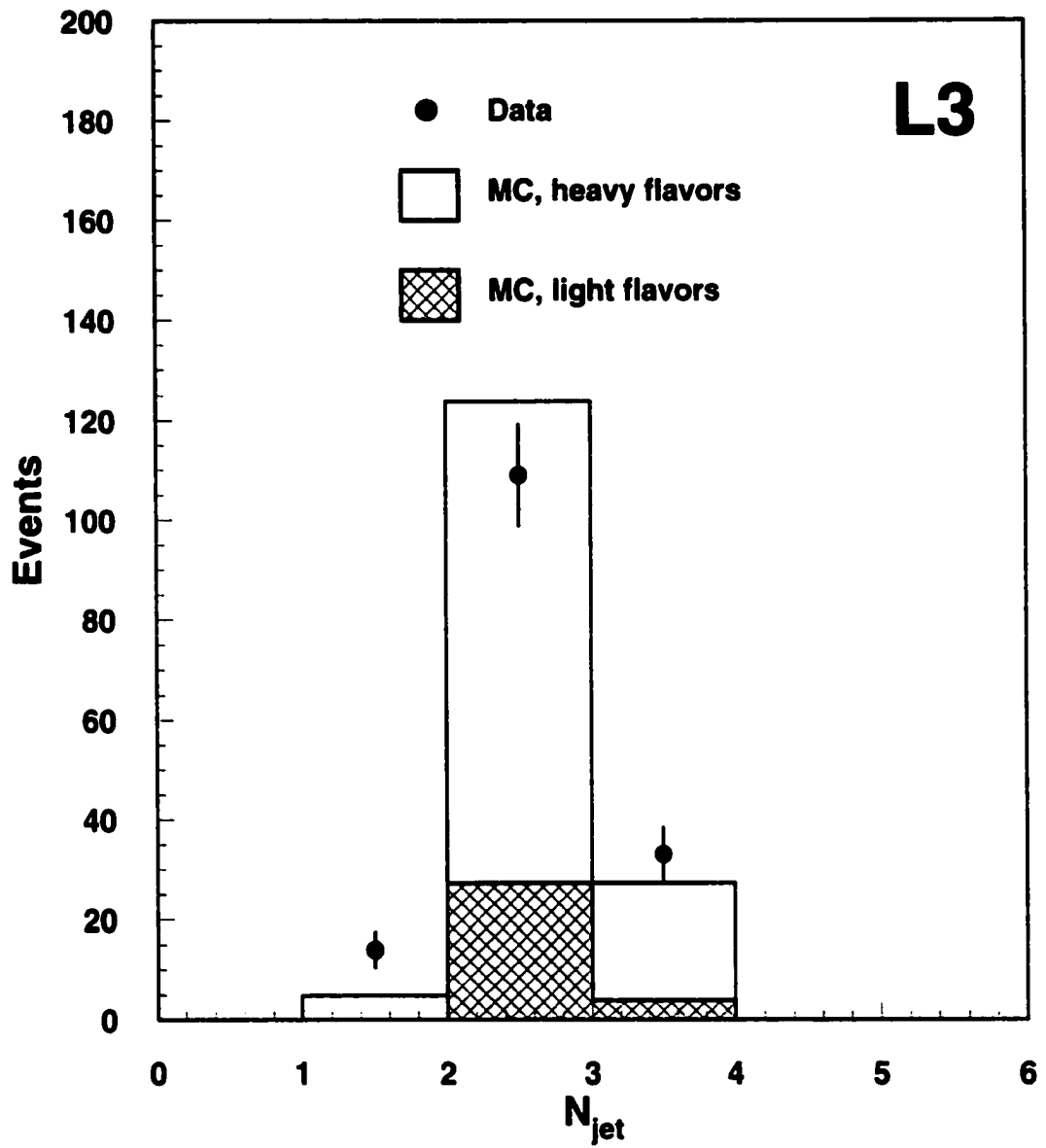


Figure 6.2: Comparison between data and Monte Carlo for the number of jets. There is a good agreement between data and Monte Carlo.

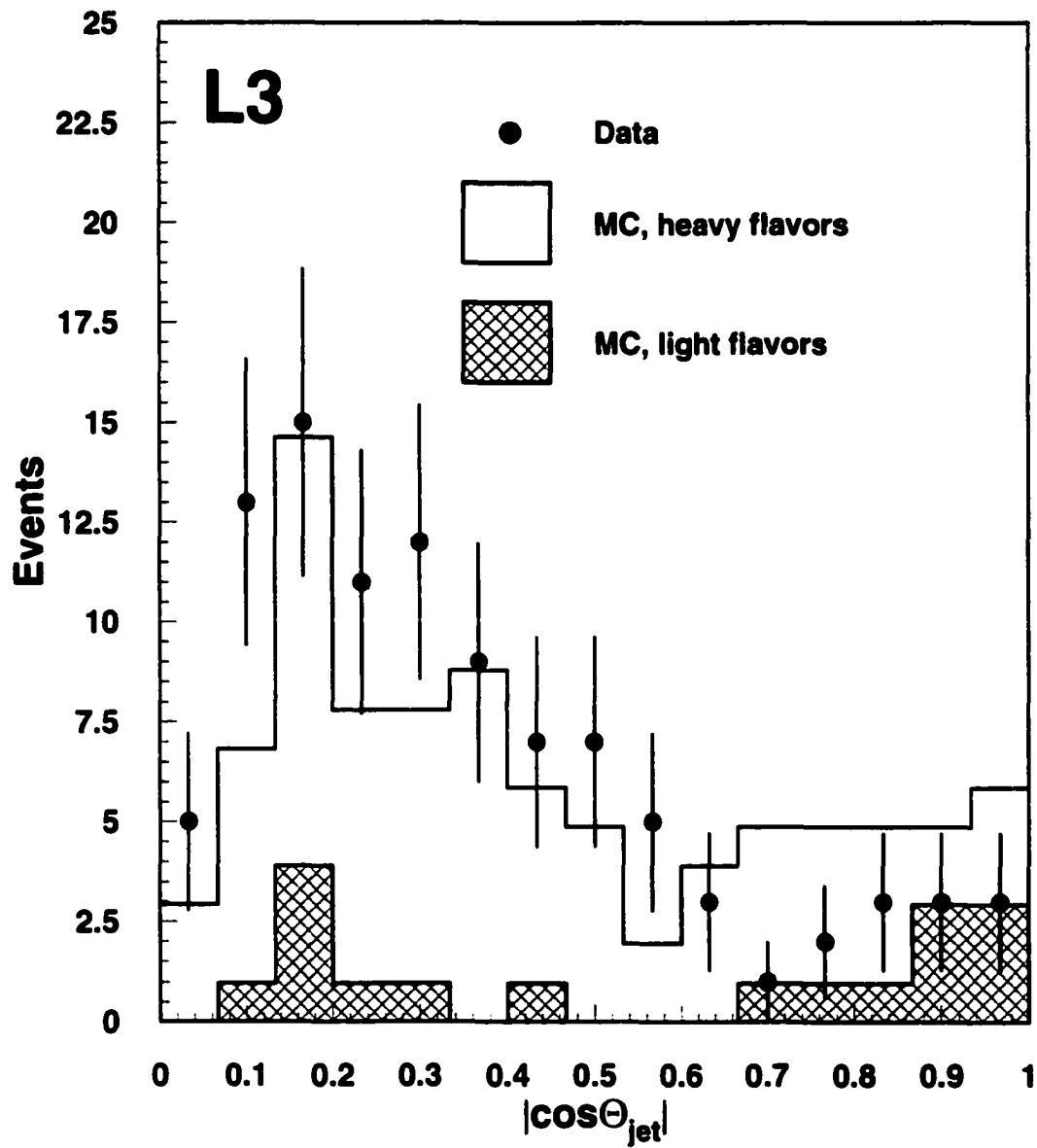


Figure 6.3: The angular distributions of jets for the data and Monte Carlo.

modified since these conditions are not met. The more precise equation for calculating the cross section is as follows:

$$\sigma = \frac{(N_{obs}^{cand} - N_{bkg}^{cand})\pi}{\mathcal{L}\epsilon_{trig}\epsilon_{sel}} \quad (6.3)$$

In this equation:

- N_{obs}^{cand} is the number of observed candidates. In this analysis N_{obs}^{cand} refers to the number of selected lepton candidates (N_{obs}^{lept}).
- N_{bkg}^{cand} is the number of background events which for this measurement is the total number of annihilation events and two-photon τ pair production events that pass the selection criteria (N_{bkg}^{lept}).
- π is a quantity called *purity*. For this analysis purity is the ratio of the selected b events to the total number of events.
- ϵ_{trig} is called the *trigger efficiency* and represents the fraction of the events that the detector is able to trigger on. The trigger efficiency for the selected data events is 94.4%. This number is determined from the data using the efficiency of each trigger level at the hadronic selection level. The level 1 trigger efficiency is derived using a set of independent triggers.
- ϵ_{sel} is referred to as the *selection efficiency* and corresponds to the fraction of the desired events which can pass through the selection criteria.

The selection efficiency, ϵ_{sel} , is the fraction of bottom events selected by the lepton tag analysis relative to the events generated in the full phase space.

This quantity is calculated directly from the Monte Carlo. The Monte Carlo sample is a mixture of direct and resolved events of $e^+e^- \rightarrow e^+e^-b\bar{b}X$. The ratio of the direct to the resolved fraction is 1:1.

The purity, π , is defined as:

$$\pi = \frac{N_b^{lept}}{N_b^{lept} + N_{nb}^{lept}}. \quad (6.4)$$

In order to be less dependent on the Monte Carlo flavor composition (bottom to non-bottom fraction), the purity can be rewritten as:

$$\pi = (1 - \frac{\epsilon_{nb}}{\epsilon_d}) / (1 - \frac{\epsilon_{nb}}{\epsilon_b}) \quad (6.5)$$

where the ϵ_b (ϵ_{nb}) is the fraction of bottom N_b^{lept} (non-bottom N_{nb}^{lept}) events, accepted by the final selection from the bottom (non-bottom) events obtained after the hadronic selection. The quantity ϵ_d is defined by the relation:

$$\epsilon_d = \frac{N_b^{lept} + N_{nb}^{lept}}{N_b^{had} + N_{nb}^{had}} = \frac{N_{obs}^{lept} - N_{bkg}^{lept}}{N_{obs}^{had} - N_{bkg}^{had}} \quad (6.6)$$

and can thus be determined directly from the data. Equation 6.5 is obtained by noticing that the total number of selected hadronic events $N_b^{had} + N_{nb}^{had}$ can be expressed as:

$$\frac{N_b^{lept} + N_{nb}^{lept}}{\epsilon_d} = \frac{N_b^{lept}}{\epsilon_b} + \frac{N_{nb}^{lept}}{\epsilon_{nb}}. \quad (6.7)$$

This method of deriving the purity is insensitive to the absolute normalization of the bottom and background Monte Carlo.

Once all the quantities in Eq. 6.3 are known, the cross section can be calculated. This method is often referred to as the cut based technique since a cut is applied on all the variables in the analysis. The cross section

measurement will have a *statistical* error associated with it. This is an error that is due to the inherent statistical fluctuations in counting random events. The statistical uncertainty in the case of the cut based method can be derived as follows:

$$\frac{\Delta\sigma_{stat}}{\sigma_{stat}} = \frac{\sqrt{N_{obs}^{lept}}}{\pi(N_{obs}^{lept} - N_{bkg}^{lept})(1 - \frac{\epsilon_{nb}}{\epsilon_b})} \approx \frac{1}{\pi\sqrt{N_{obs}^{lept}}} \quad (6.8)$$

6.2.2 Fit Based Method

An alternative to the cut based method is fitting. In this method the cross section is derived by using a statistical fit to a sensitive variable. In other words, in this type of analysis a cut will not be applied on at least one variable. Figures 5.1 and 5.2 reveal a similar topology for semi-leptonic decays of charm and bottom quarks. However, due to the much higher mass of the b quark, one would expect a greater transverse momentum of the leptons with respect to the jet in b decays. The transverse momentum of the lepton can then be utilized for a cross section measurement. In this analysis the transverse momentum of the lepton with respect to the closest jet, P_t , is chosen as a suitable fit variable. The algorithm for calculating P_t with respect to the closest jet assigns directions for both the jet and the lepton. If these directions point to opposite hemispheres, the value of P_t will be negative. These events are excluded from the fit. The number of such events in the electron and muon data samples are 19 and 29 respectively.

The goodness of a fit can be judged by the χ^2 of the fit. A smaller χ^2 is an indication of a better fit. Therefore, the best fit can be derived by minimizing the χ^2 . In this analysis a three parameter binned χ^2 fit is applied

to the data distribution. The data sample consists of b (N_b), c (N_c), uds (N_{uds}) and non two-photon background (N_{bkg}) events:

$$N_{data} = N_b + N_c + N_{uds} + N_{bkg} \quad (6.9)$$

Since the background events are well known standard model processes, their number can be directly obtained from Monte Carlo. The number of bottom quarks can be obtained by applying a three parameter fit where N_b , N_c and N_{uds} are free parameters and N_{bkg} is held fix. The fit uses the shape of the distributions of b, c and uds when the distributions are normalized to 1. In other words, the shape of the distributions are provided by Monte Carlo while the number of events (N_b , N_c and N_{uds}) are decided by the fit. In a bin of P_t , the χ^2 can be calculated as follows:

$$\chi_i^2 = \frac{(N_{data_i} - N_{b_i} - N_{c_i} - N_{uds_i} - N_{bkg_i})^2}{\sigma_i^2} \quad (6.10)$$

where $\sigma_i = \sqrt{N_{data_i}}$. The minimization process was performed by the MINUIT¹ package.

Besides the number of bottom quarks, N_b , the fit also provides the error on this number (δ_{N_b}). Similarly, δ_{N_c} and $\delta_{N_{uds}}$ are given by the fit. Once the number of different quark flavors and their errors are found, one can calculate the purity and cross section. The purity and its error can be calculated as follows:

$$\pi_b = \frac{N_b}{N_b + N_c + N_{uds}} \quad (6.11)$$

¹MINUIT is a software package dedicated to minimizing different functions (including a χ^2 function). It is widely used in the particle physics community.

$$\delta_{\pi_b} = \frac{\delta_{N_b}}{N_b + N_c + N_{uds}} \quad (6.12)$$

The cross section and its statistical error are given by:

$$\sigma(e^+e^- \rightarrow e^+e^-b\bar{b}X) = \frac{N_b}{\mathcal{L}\epsilon_{trig}\epsilon_{sel}} \quad (6.13)$$

$$\Delta\sigma(e^+e^- \rightarrow e^+e^-b\bar{b}X) = \frac{\delta_{N_b}}{\mathcal{L}\epsilon_{trig}\epsilon_{sel}} \quad (6.14)$$

where ϵ_{sel} is calculated the same way as in the cut based method.

The fitting method can be applied to both the electron and muon data samples in order to measure the cross section for each of these channels. Each of these samples corresponds to 410.1 pb^{-1} of data taken at center-of-mass energies from 189 GeV to 202 GeV. The luminosity averaged center-of-mass energy, $\langle \sqrt{s} \rangle$, is 194 GeV.

6.3 Cross Section Using Electron Fit

The P_t spectrum of the electron data sample contains 137 events. The b selection efficiency, ϵ_{sel} is 1.25%. The three parameter χ^2 fit is applied to this distribution. The fit has a χ^2 per degree of freedom of 10.1/6. The number of different flavors are given in Table 6.1:

Table 6.1: Fit results for the electron tag.

Fit parameter	Electron tag
N_{bkg}	2.9 (fixed)
N_b	52.5 ± 14.1
N_c	71.5 ± 14.8
N_{uds}	$0.0^{+7.4}_{-0.0}$

Based on these numbers the b fraction of the sample is $42.3 \pm 11.4(\text{stat})\%$.

The cross section for bottom production and its statistical error is:

$$\sigma(e^+e^- \rightarrow e^+e^-b\bar{b}X)_{\text{electrons}} = 10.9 \pm 2.9(\text{stat})\text{pb}$$

Figure 6.4 shows the P_t distribution of data and that of different quark flavors. The dashed histogram represents the total contributions of u, d, s, c and non two-photon background. The solid histogram is derived by including the b fraction (which consists of N_b events). It is quite obvious that the bottom fraction is needed in order to describe the data. If no bottom fraction is included in the fit, a confidence level of 1.2×10^{-3} is obtained.

6.4 Cross Section Using Muon Fit

The cross section measurement by muons follows the same procedure as for the electrons. The P_t spectrum of the muon sample has 269 events and the b selection efficiency is 2.20%. The three parameter χ^2 fit to the P_t distribution of muons yields a χ^2 per degree of freedom of 6.2/6. The result of the fit are given in Table 6.2:

Table 6.2: Fit results for the muon tag.

Fit parameter	Muon tag
N_{bkg}	16.2 (fixed)
N_b	126.7 ± 24.1
N_c	119.0 ± 24.0
N_{uds}	$0.0^{+33.0}_{-0.0}$

Based on these numbers the b fraction of the sample is $51.6 \pm 9.8(\text{stat})\%$.

The cross section for bottom production and its statistical error is:

$$\sigma(e^+e^- \rightarrow e^+e^-b\bar{b}X)_{\text{muons}} = 14.9 \pm 2.8(\text{stat})\text{pb}$$

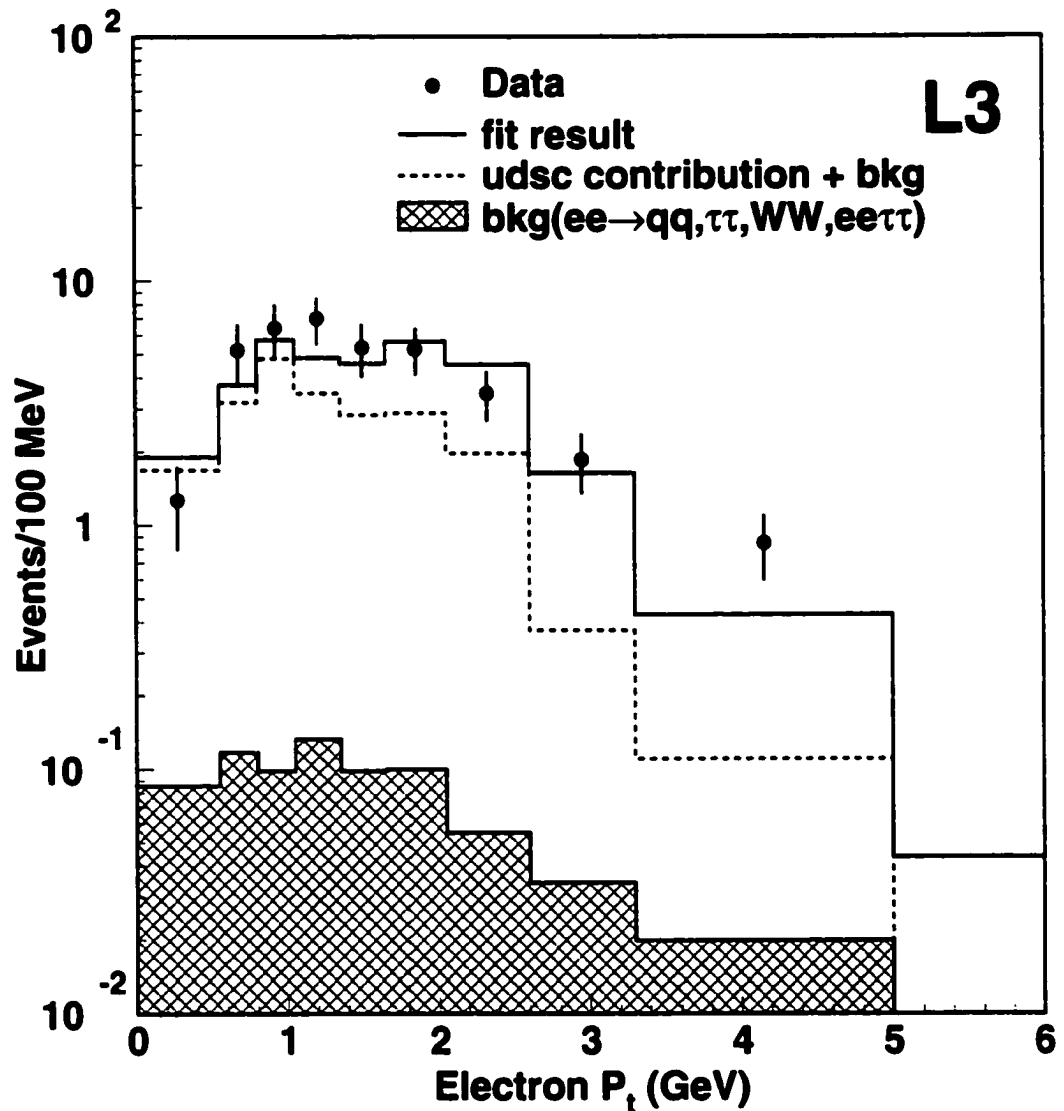


Figure 6.4: The distribution of the transverse momentum, P_t , of the electron candidate with respect to the closest jet. The solid histogram which contains N_b bottom events is in a much better agreement with the data than the dashed histogram.

Figure 6.5 shows the P_t distributions of data and different quark flavors. The dashed histogram is the total contributions of u, d, s, c and non two-photon background. The solid histogram includes the b fraction (with N_b events). It is evident that the bottom fraction is needed in order to describe the data. The exclusion of the bottom fraction will give a confidence level of 2.2×10^{-5} .

6.5 Systematic Errors

Besides statistical error, any physics measurement is accompanied by a *systematic* error. Generally, these are uncertainties in the bias of the data. Unlike statistical errors, the systematic errors can have many different sources. The understanding of possible sources of systematic errors and the extent of their contribution is a challenge in itself. Both the way the candidate events are selected and the method by which the cross section is measured introduce systematic errors.

In this analysis the systematic errors are as follows:

- **Event Selection.**

This type of systematic error is due to the cut variation. The final data sample is derived by applying different cuts on various variables. A slight change in these cuts may yield a different value for the cross section. This is because a change in the number of data events passing a different cut value may not be accompanied by a corresponding change in the efficiency for passing the cut. The efficiency is determined from Monte Carlo. Thus by imposing a specific set of cuts a systematic error is being introduced to the measurement. The value of this systematic

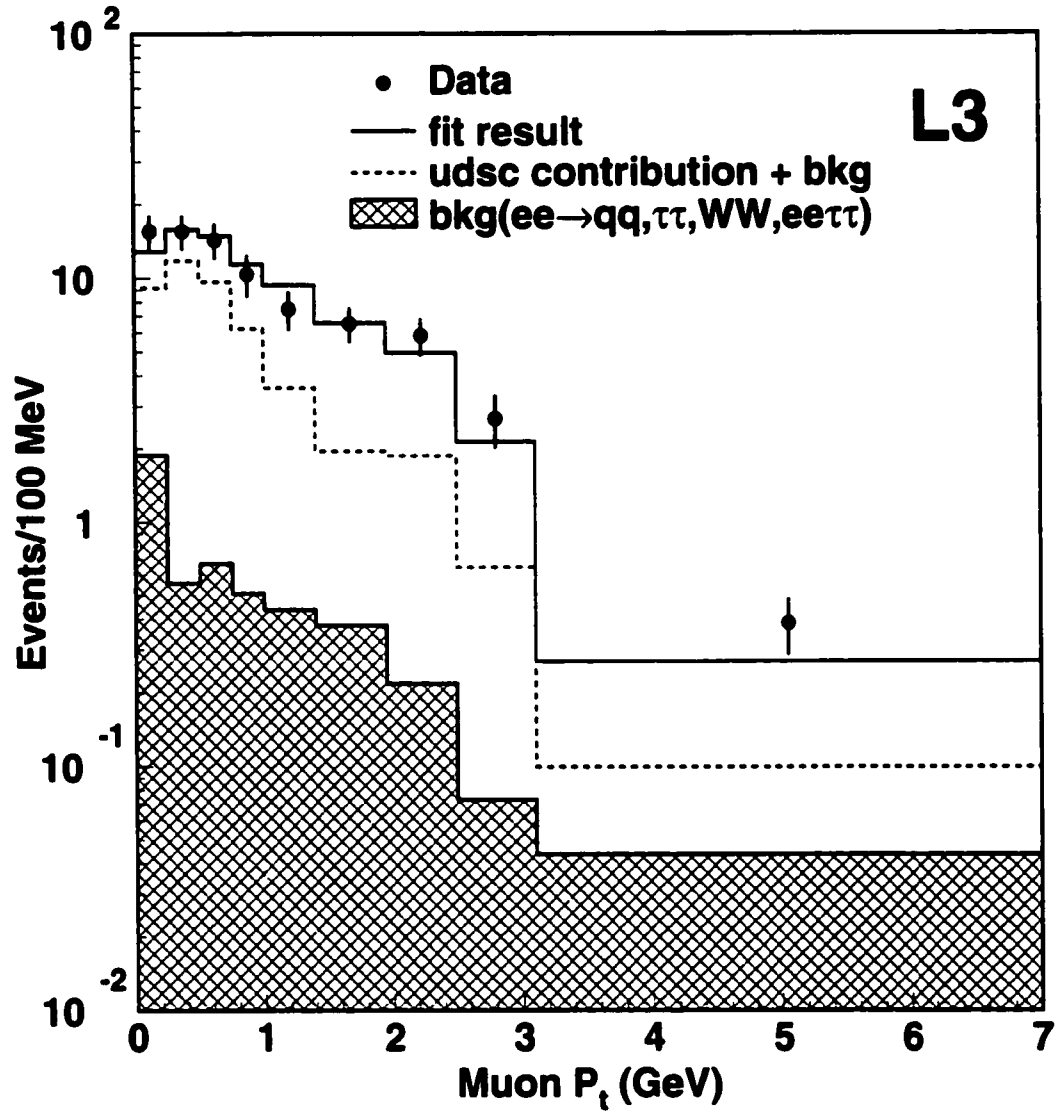


Figure 6.5: The distribution of the transverse momentum, P_t , of the muon candidate with respect to the closest jet. The solid histogram is derived by including N_b bottom events.

error can be calculated by changing each cut separately and recalculating the cross section with the new cut. The difference between the new cross section and the original one is considered the systematic error due to that cut. The cut variations should include detector resolution uncertainties. To estimate the systematic error due to cut variation, the cut variations should not result to a sizable change of statistics. In that case the errors of systematic nature will be entangled with those due to statistics.

- **Jet Reconstruction.**

The cross section is derived by fitting the spectrum of the transverse momentum of the lepton candidate with respect to the closest jet. This means that the value of the cross section is sensitive to the way a jet is reconstructed (y_{cut}). As a result, a systematic error is associated with the value of the y_{cut} . This error is derived by recalculating the cross section with a new y_{cut} of 0.15. A change of y_{cut} to 0.15 will change the distribution of the number of jets.

- **Massive or Massless Charm.**

As mentioned in Section 2.4, theoretical NLO QCD calculations can be carried out through massless or massive scenarios. The Monte Carlo event generation can implement any of these calculations. Due to the high mass of the bottom quark, massive method is used for generating $e^+e^- \rightarrow e^+e^-b\bar{b}X$ events while charm events are produced with the massless approach. The massless calculation for charm is a reasonable

approach since the mass of the charm quark is much smaller than that of bottom. However, the cross section is also calculated with the massive charm Monte Carlo. The difference of these two cross sections is considered a systematic error.

- **b Semi-leptonic Branching Ratio.**

The measured cross section assumes the semi-leptonic branching ratio of the b quark to be constant. This is not the case in reality. Despite the theoretical certainty on the semi-leptonic branching ratio of the b quark, there is an uncertainty on its experimental value. A change in the semi-leptonic branching ratio of the b quark will result in a different cross section. This effect has been taken into account as one of the sources of the systematic error.

- **Trigger efficiency.**

According to equations 6.3 and 6.13, the cross section measurement relies on the value of trigger efficiency. This quantity is measured itself and like other measured quantities is bound to have an associated error. Certainly an error on trigger efficiency leads to a systematic error on the cross section. The error on trigger efficiency is 3%.

- **Monte Carlo Statistics.**

Another component for cross section measurement is the selection efficiency. Similar to trigger efficiency, the error on selection efficiency is a source of systematic error. Since the calculation of the selection

efficiency relies on Monte Carlo, the source of its uncertainty can be attributed to the Monte Carlo Statistics.

- **Direct to Resolved Ratio.**

The cross section measurement is done by assuming the bottom fraction to consist of 50% direct and 50% resolved events. This assumption is legitimate on theoretical grounds. Nonetheless, there might be a slight deviation from this mixture in reality. This deviation is considered a source of systematic error. This error is estimated by changing the direct to resolved ratio from 1:1 to 1:2 or 2:1 and then getting the mean of the differences of the new cross sections from the original one.

The contribution from each of these sources are given in Table 6.3. The total systematic error for each channel (electron or muon) can be calculated by adding the systematic errors from different sources in quadrature as follows:

$$\sigma_{tot} = \sqrt{\sum \delta\sigma_i^2} \quad (6.15)$$

where $\delta\sigma_i$'s are the systematic errors of different sources. The total systematic error for electron and muon channels are 2.0 pb and 2.6 pb respectively.

$$\sigma(e^+e^- \rightarrow e^+e^-b\bar{b}X)_{\text{electrons}} = 10.9 \pm 2.9(\text{stat}) \pm 2.0(\text{sys})\text{pb}$$

$$\sigma(e^+e^- \rightarrow e^+e^-b\bar{b}X)_{\text{muons}} = 14.9 \pm 2.8(\text{stat}) \pm 2.6(\text{sys})\text{pb}$$

The results of electron and muon channels can be combined as well. The combined result is:

Table 6.3: Systematic uncertainties on $\sigma(e^+e^- \rightarrow e^+e^-b\bar{b}X)$ in percent.

Source of uncertainty	Muon tag	Electron tag
	$\Delta\sigma, \%$	$\Delta\sigma, \%$
Event selection	14.6	15.8
Jet reconstruction	8.2	8.2
Massive/massless charm	3.0	3.0
B($b \rightarrow e, \mu$)	2.0	2.0
Trigger efficiency	2.0	2.0
Monte Carlo statistics	1.4	1.8
Direct / resolved ratio	1.0	0.9
Total	17.3	18.4

$$\sigma(e^+e^- \rightarrow e^+e^-b\bar{b}X)_{\text{combined}} = 13.1 \pm 2.0(\text{stat}) \pm 2.4(\text{sys})\text{pb}$$

6.6 Cut Based Cross Section

The fit result for bottom production can be checked by the cut based method. This method is used to calculate the bottom production cross section by its semi-leptonic decay to electron. The cuts applied for electron candidate selection are similar to those in Table 5.1. In addition, a cut is applied to transverse momentum with respect to the closest jet, P_t . Figure 6.6 shows the distribution of this variable when all the other cuts are applied. In this Figure, the charm fraction is scaled to the measured cross section. There is an excess of data at higher values of transverse momentum. This is caused by the presence of bottom production in the data. In order to increase the bottom purity of the data sample, a cut of $P_t > 1.0$ GeV is applied.

After applying all cuts 106 electron candidates remain. The bottom selection efficiency, ϵ_{sel} , is 1.2%. The bottom purity is derived as it was explained in section 6.2.1. The bottom purity is 49.0%. There are 2.5 non two-photon

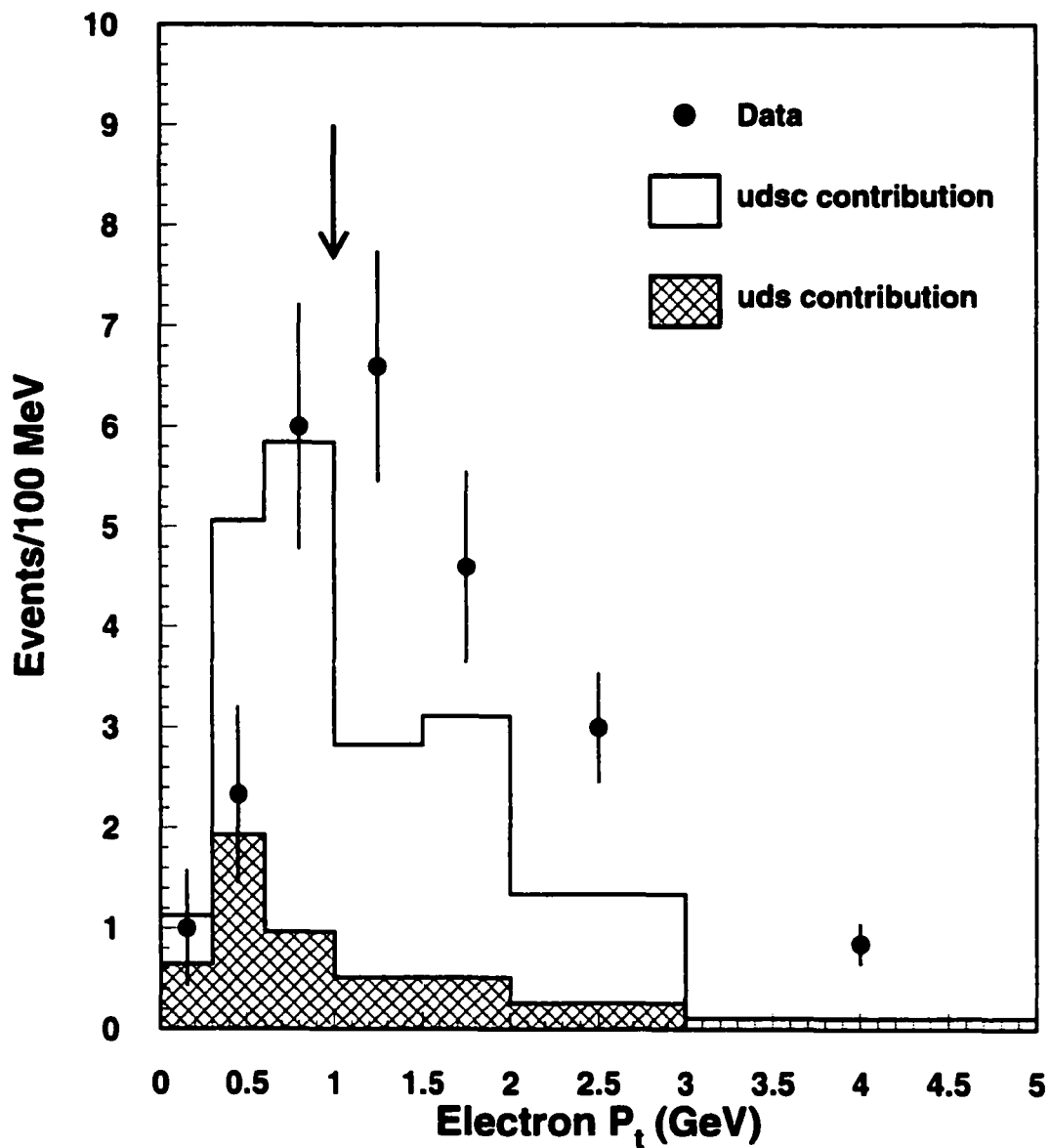


Figure 6.6: The distribution of the transverse momentum of the electron candidate with respect to the closest jet. The excess in data is due to the bottom fraction.

background events. These numbers will give the following cross section result which is in good agreement with that of the fit.

$$\sigma(e^+e^- \rightarrow e^+e^-b\bar{b}X)_{\text{electrons}} = 11.3 \pm 2.3(\text{stat})\text{pb}$$

6.7 Consistency With Charm

The fit provides the number of bottom and charm events simultaneously. This provides the opportunity for measuring the cross section of charm production in parallel to bottom. The charm cross section results that are derived this way, will have a larger statistical error than previous measurements. This is because the cuts for selecting lepton candidates are aimed at increasing the bottom fraction by reducing the number of charm events. Despite a higher statistical error, the charm cross sections from the fit are a good cross check for the validity of the fitting method. The charm selection efficiency for the electron and muon channels are 0.02% and 0.04% respectively. Tables 6.1 and 6.2 yield the following charm cross section results:

$$\sigma(e^+e^- \rightarrow e^+e^-c\bar{c}X)_{\text{electrons}} = 1092 \pm 226(\text{stat})\text{pb}$$

$$\sigma(e^+e^- \rightarrow e^+e^-c\bar{c}X)_{\text{muons}} = 814 \pm 164(\text{stat})\text{pb}$$

These numbers are compatible with each other and other charm measurements (see Figure 1.5).

6.8 Comparison With Theory

A crucial point for any physics measurement is to what extent it agrees with theoretical expectations. One is able to confirm or reject the theoretical models depending on whether the experimental result agrees or disagrees

with them. A good agreement between theory and experiment enhances our faith in the theory. In contrary, a disagreement between the two requires the underlying theory to be modified.

We have compared our result with the theoretical predictions of NLO QCD [6]. Figure 6.7 illustrates this comparison. In this plot the cross sections for both bottom and charm production² are compared with theory. The dashed lines correspond to the direct process and the solid lines show the sum of direct and resolved processes. The prediction for bottom production is calculated with a b quark mass of 4.5 GeV or 5.0 GeV and the threshold energy for bottom production is set to 10.6 GeV. The calculations for charm production are done for two different masses of 1.3 GeV or 1.7 GeV and the threshold energy is set to 3.8 GeV. The plot clearly demonstrates that the experimental results for charm production are in very good agreement with the theory while there is a disagreement for bottom production. The theoretical prediction for the bottom quark production at $\langle \sqrt{s} \rangle = 194$ GeV and a b quark mass of 4.5 GeV is 4.4 pb. Therefore the measured cross section is a factor of 3 and about 4 statistical uncertainty standard deviations higher than expected.

Figure 6.8 shows the distribution for the momentum of the electron candidates. This plot is made by adding a bottom fraction of 4.4 pb (theory prediction) to the udsc contribution. As can be seen after adding the bottom fraction, the data and Monte Carlo are still in disagreement. There is still some excess in data when the added bottom fraction is based on the

²In this plot only the charm results from the L3 collaboration are shown.

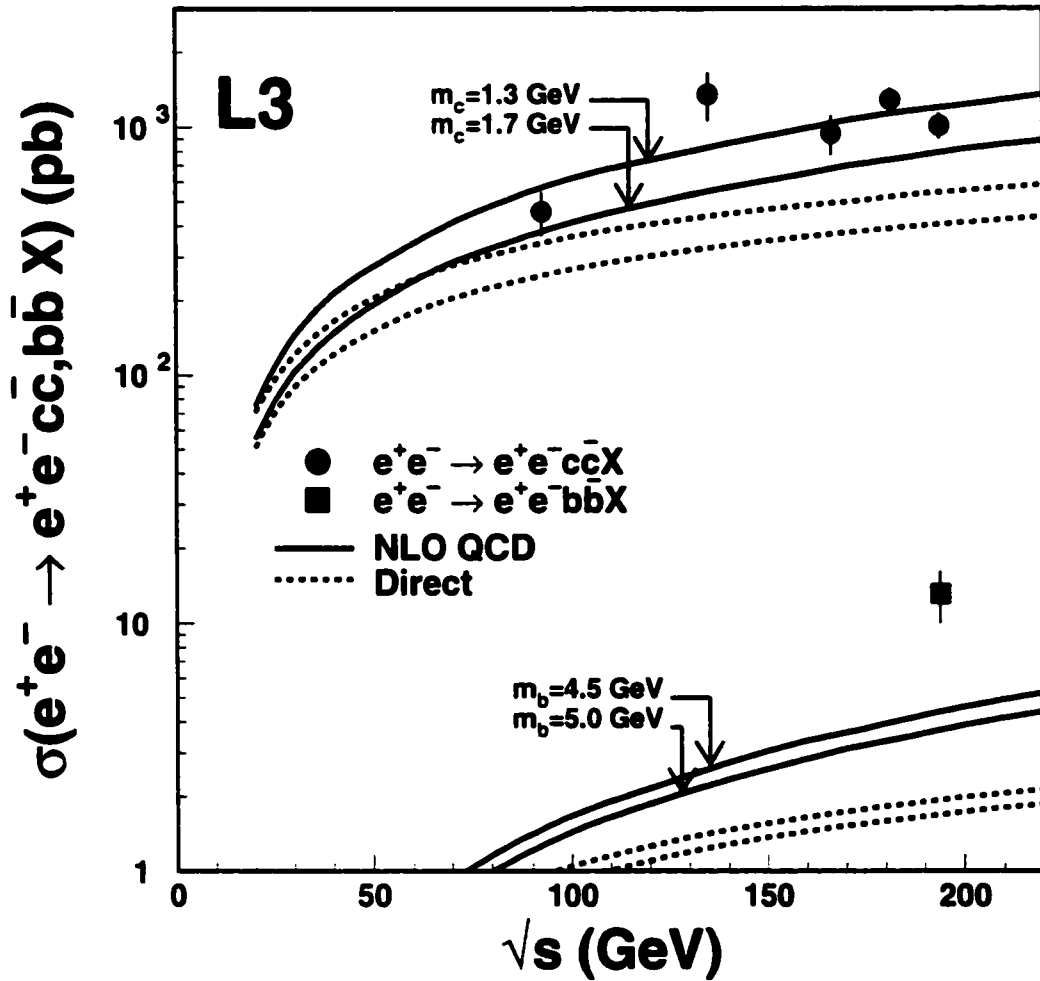


Figure 6.7: The comparison between theory and experiment for bottom and charm production in two-photon collisions. The cross section for bottom production is the combined results of the electron and muon channels. The errors are derived by adding the statistical and systematic uncertainties in quadrature.

theory expectation. This is an indication that the theoretical expectation for the cross section is lower than the real value. Figure 6.9 shows the same distribution when the added bottom fraction corresponds to the combined measured values in the electron and muon channels (13.1 pb). There is a perfect agreement between data and Monte Carlo on this plot. This agreement is a good confirmation of the validity of our measured cross section for bottom production.

6.9 Prospects For Other Experiments

The first preliminary results of this analysis were presented at PHOTON99 conference [34] on May of 1999 in Freiburg, Germany. The modified results were again presented at PHOTON2000 conference [35] on August of 2000 in Ambleside, England. Both results are published in the proceedings of these conferences. The final results were published in Physics Letters B in March of 2001 [36].

This analysis is the first measurement of $\sigma(e^+e^- \rightarrow e^+e^-b\bar{b}X)$ and our results are the only published values. Another LEP experiment, OPAL, has tried to make the same type of measurement as well. They have performed their measurement by tagging the b quark through its semi-leptonic decay to a muon. Their latest preliminary result was presented at PHOTON2001 conference on September of 2001 in Ascona, Switzerland. Their measurement confirms our results. OPAL's preliminary result is:

$$\sigma(e^+e^- \rightarrow e^+e^-b\bar{b}X)_{\text{OPAL}} = 14.2 \pm 2.5(\text{stat})_{-4.8}^{+5.3}(\text{sys})\text{pb}$$

The other two LEP experiments, ALEPH and DELPHI, have not yet presented any result for measurement of bottom quark production in two-

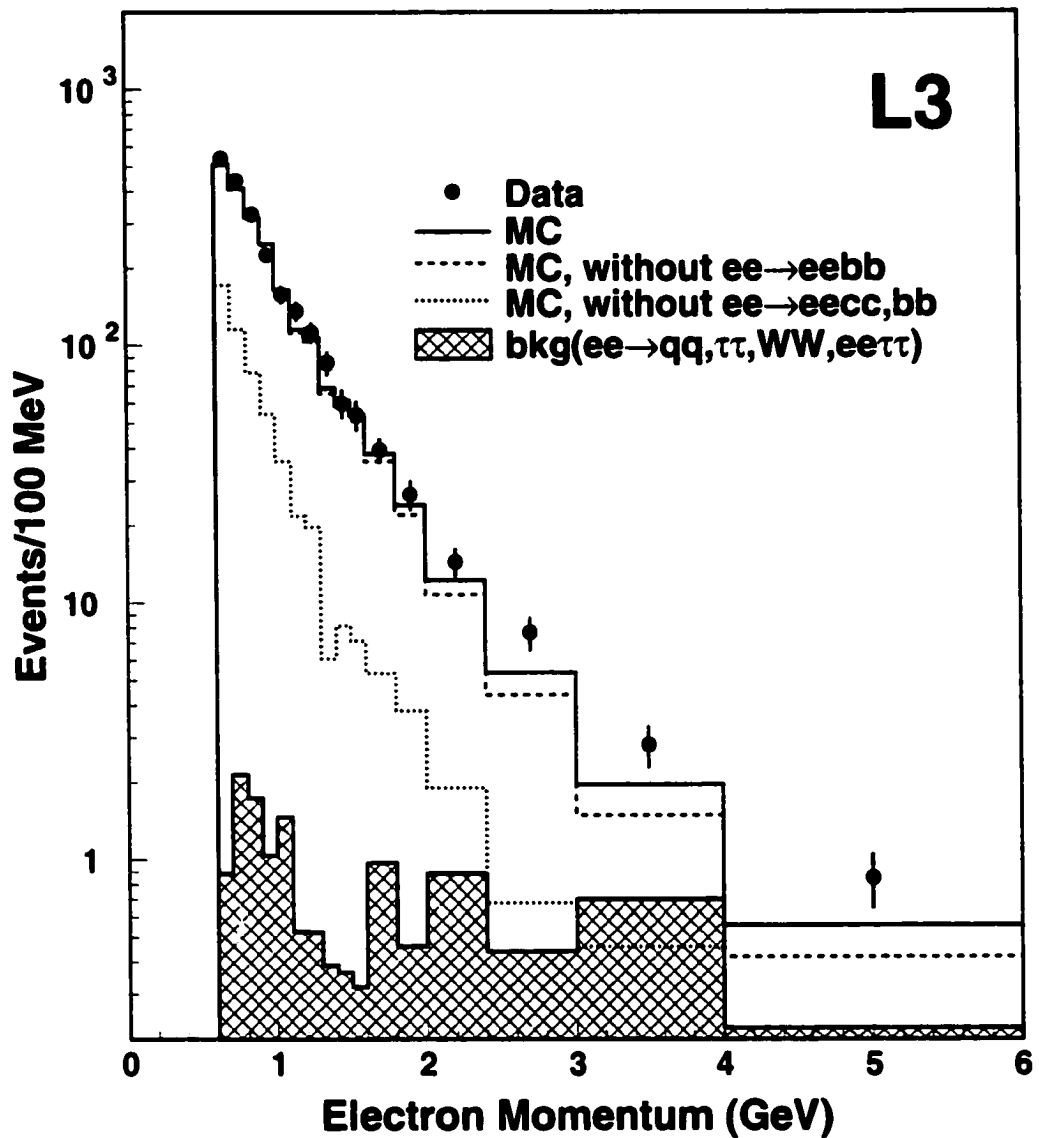


Figure 6.8: The distribution of the momentum of the electron candidate. The dotted, dashed and solid histograms are the contributions of uds , $udsc$ and $udscb$ quarks from the PYTHIA Monte Carlo. The c fraction of the Monte Carlo is scaled to the measured cross section and the b fraction corresponds to the theoretical prediction. There is still disagreement between the data and Monte Carlo.

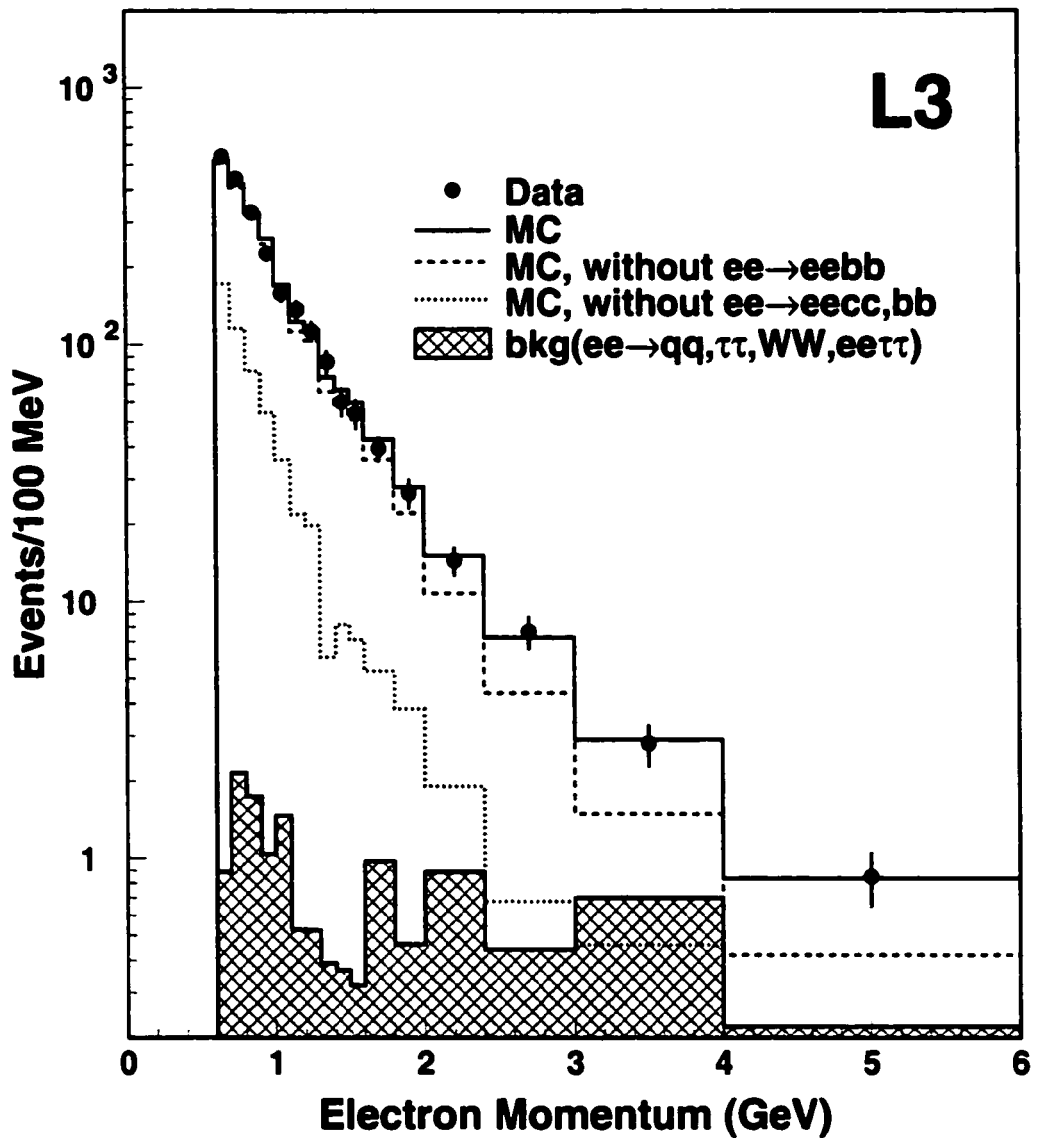


Figure 6.9: The distribution of the momentum of the electron candidate. The dotted, dashed and solid histograms are the contributions of uds , $udsc$ and $udscb$ quarks from the PYTHIA Monte Carlo. The c and b fractions of the Monte Carlo are scaled to the measured cross sections. There is a perfect agreement between the data and Monte Carlo.

photon collisions. Besides the LEP experiments, the most active experiment in two-photon physics is CLEO at CESR³. Despite the high luminosity of CESR, CLEO has not been able to measure bottom production in two-photon collisions. This is due to the low center of mass energy of CESR (around 10 GeV).

³CESR is an electron-positron collider located at Cornell university.

CHAPTER 7

CONCLUSION AND OUTLOOK

7.1 The First Measurement Of $e^+e^- \rightarrow e^+e^-b\bar{b}X$

Heavy flavor production in $\gamma\gamma$ physics has provided many reliable tests of QCD. Moreover, it has enhanced our knowledge of the structure and interaction of photon. Among the heavy flavor quarks, charm production has been studied by different experiments at various center of mass energies. A former LSU student, Alan Stone, did his thesis on charm production at LEP [37]. On the other hand, b quark production in $\gamma\gamma$ collisions was never measured since its cross section is suppressed by two orders of magnitude (compared to charm). The higher energy and luminosities of the LEP collider provided the opportunity to perform the first measurement of $e^+e^- \rightarrow e^+e^-b\bar{b}X$. In this analysis the b quarks are identified through their semi leptonic decay to an electron or muon.

Charm production measurements agree quite well with theoretical predictions over a wide range of center of mass energies [38, 39, 40, 41, 42, 43, 44] (Figure 1.5). The L3's charm measurements were done by detecting semi leptonic decays of c quarks or via D^* tag [32, 45]. Both results agree with each other and with that of other LEP experiments. The charm measurements at high energies require the existence of the resolved process which is an indication of the gluonic content of the photon.

Contrary to charm, the measured cross section for b production does not agree with theory (Figure 6.7). The L3's measurements in the electron and muon decay modes are compatible with each other and their combined value

is:

$$\sigma(e^+e^- \rightarrow e^+e^-b\bar{b}X)_{\text{combined}} = 13.1 \pm 2.0(\text{stat}) \pm 2.4(\text{syst})\text{pb} \quad (7.1)$$

Theory predicts this cross section to be 4.4 pb at the nominal value of $m_b = 4.5$ GeV. Therefore the measured cross section at this mass value is a factor of 3 and about 4 statistical uncertainty standard deviations higher than expected. The disagreement does not depend on the choice of QCD parameter μ (Figure 7.1 at $m_b = 4.5$ GeV). As Figure 7.1 shows, the theoretical and experimental results will disagree unless $m_b \leq 3.5$ GeV.

The same phenomenon has been observed in other types of hadron collisions. γp and $p\bar{p}$ experiments have observed a higher cross section for the b quark production [1, 2] (Figures 1.6 and 1.7). Their results are also higher by a factor of 2-3. Consequently, the discrepancy in the $\gamma\gamma$ physics is compatible with that of γp and $p\bar{p}$ and confirms their deviation.

The LEP collider was the highest energy e^+e^- collider and therefore the best facility for $\gamma\gamma$ physics at high center of mass energies. LEP collected 410 pb⁻¹ of data during 1998-1999 at center of mass energies of 189-202 GeV with a mean center of mass energy of $\langle \sqrt{s} \rangle = 194$ GeV. This data sample has been utilized for the b quark production measurement. The inclusion of around 220 pb⁻¹ data taken in the year 2000 will reduce the statistical uncertainty on this measurement. Nonetheless, the next major breakthrough in $\gamma\gamma$ physics will be achieved at future high energy e^+e^- colliders.

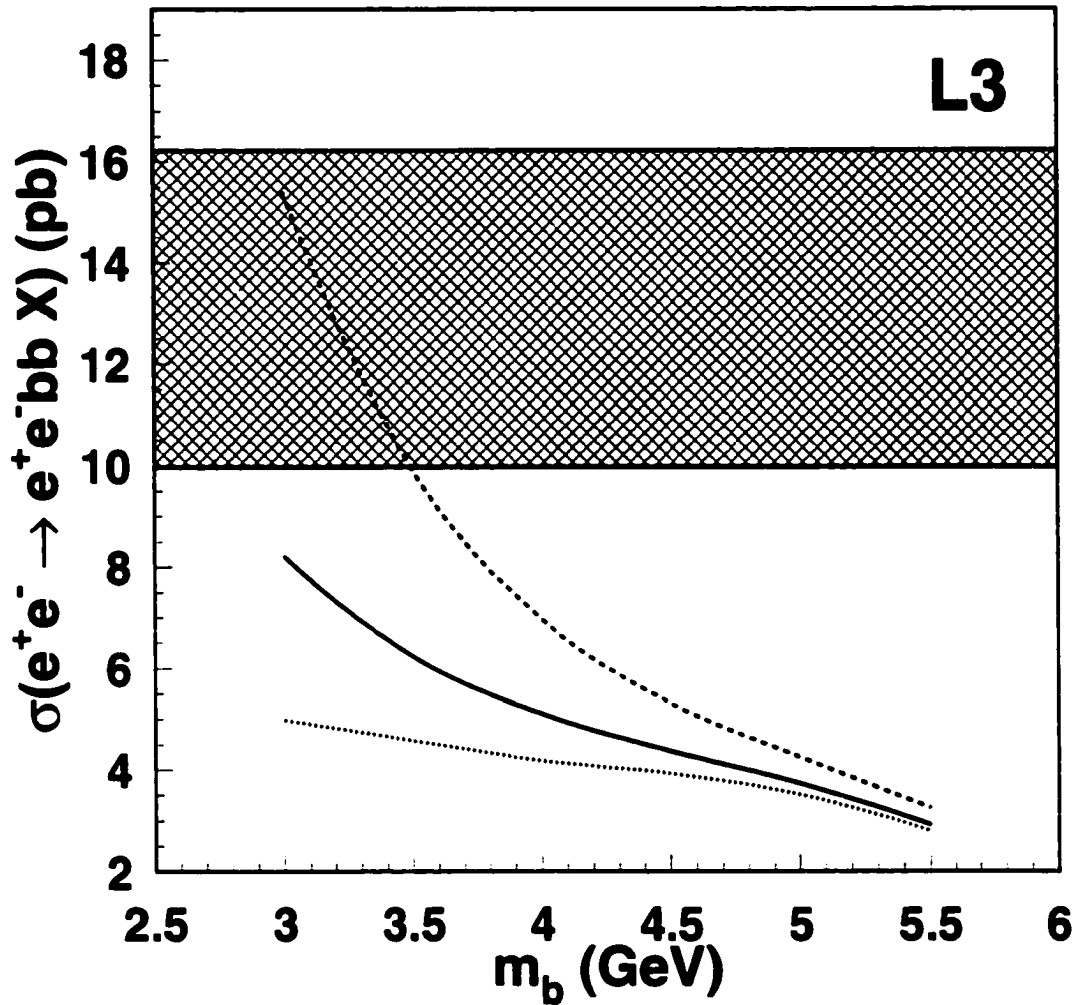


Figure 7.1: The comparison between the L3 measurement result and theoretical predictions for b quark production. The solid, dashed and dotted curves represent NLO QCD predictions for a renormalization scale value of $\mu = m_b, m_b/2$ and $2m_b$ respectively. The hatched area illustrates the combined measured value of the electron and muon channels with statistical and systematics uncertainties added in quadrature (Eq. 7.1).

7.2 Next Linear Collider

Search for new phenomena and discoveries require that particle physicists perform their research at even higher energies. In this respect the particle physics community is considering the construction of other e^+e^- colliders with higher energies. One of these proposals is the construction of the Next Linear Collider (NLC) [46]. This is an e^+e^- collider with a center of mass energy of 1 TeV. Due to the high rate of synchrotron radiation in storage rings, a 1 TeV e^+e^- accelerator has to be linear.

Unlike the case for storage rings, in a linear collider each beam is used only once. This feature makes it possible to convert electrons to high energy photons through backward Compton scattering and thus constructing a $\gamma\gamma$ collider. The NLC project could incorporate two detectors one of which might be dedicated to $\gamma\gamma$ physics (Figure 7.2). Two colliding γ 's can be produced when the two electron beams collide with focused laser beams at a distance about 0.1-1 cm from the interaction point. By choosing the appropriate laser parameters one can convert most of the electrons to high energy photons. These photons will have energies almost equal to that of the original electrons. The luminosity of the $\gamma\gamma$ collisions will also be at the same order of magnitude of the designed e^+e^- collider.

The high energy and luminosities of a $\gamma\gamma$ collider at NLC will bring many new insights into the nature of the photon. It would be very interesting to measure the b quark production cross section at these energies. Theory predicts a cross section of 33.21 pb at $W_{\gamma\gamma} = 1$ TeV. The extent of deviation from this theory prediction will provide another clue for the source of this disagreement. The b quark measurement at NLC will have a much smaller statistical uncertainty due to the higher energies and luminosities.

There exists the possibility of discovering new particles at TeV scales. In the case of a discovery, the nature of the new phenomenon will be better understood if studied in different interactions. A $\gamma\gamma$ collider can be the best place to bring more insight into these new phenomena.

7.3 Why Disagreement?

The first measurement of $e^+e^- \rightarrow e^+e^-b\bar{b}X$ is an achievement. The next achievement will be the explanation of the discrepancy between theory and experiment. Disagreements have always been the starting point for new investigations. Quite often these investigations have led to unexpected results or even discoveries. At the moment, there is no consensus as to the reason for high $\sigma(e^+e^- \rightarrow e^+e^-b\bar{b}X)$. Some of the possibilities include:

- **NNLO corections:** QCD calculations can be carried out at different level of corrections. The available theory calculations are at the NLO. The next level corrections are called Next to Next to Leading Order (NNLO) and are not yet calculated. It is possible that NNLO corrections might be large enough to explain the discrepancy. However, theorists doubt this scenario.
- **New PDF's:** The theory predictions require a set of PDF's. It maybe possible to reach an agreement between theory and experiment by changing the PDF's. This option seems remote since the disagreement is observed in both $\gamma\gamma$ and $p\bar{p}$ physics.
- **New Physics:** Another scenario for describing the discrepancy is the existence of some new and unknown phenomena. This possibility can

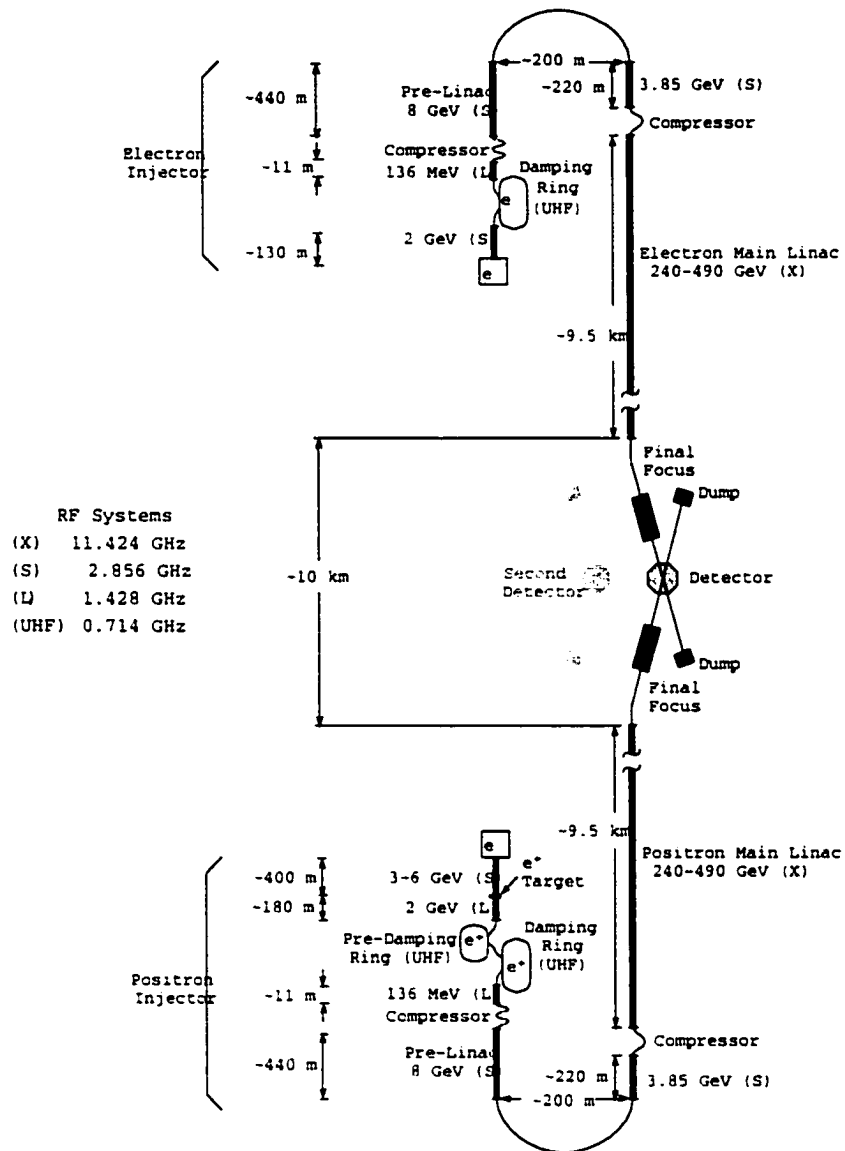


Figure 7.2: A scheme of the next linear e^+e^- collider. The proposal foresees two detectors. One of the detectors could be dedicated to $\gamma\gamma$ physics.

not be ruled out although there is no hint what this new phenomena might be. Therefore, this option deserves its due consideration as well.

It would be very exciting to see the final resolution to this dilemma. This task will rest on the shoulder of the theorists. Thus, $\gamma\gamma$ physics has proven to be a vital and dynamic branch of particle physics. This is all due to the less understood and mysterious nature of photon. Most assuredly the photon will continue to bring surprises for physicists in the future, as it has done in the past.

BIBLIOGRAPHY

- [1] H1 Collab., C. Adloff *et al.*, Eur. Phys. J. C **14**, (2000) 255.
- [2] DØ Collab., B. Abbott *et al.*, Phys. Lett. B **487**, (2000) 264.
- [3] G. Schuler, Improving the equivalent photon approximation in electron-positron collisions, CERN-TH/96-297.
- [4] G.A. Schuler and T. Sjöstrand, Phys. Lett. B **300**, (1993) 169;
G.A. Schuler and T. Sjöstrand, Nucl. Phys. B **407**, (1993) 539;
G.A. Schuler and T. Sjöstrand, Z. Phys. C **73**, (1997) 677.
- [5] G.A. Schuler and T. Sjöstrand, Z. Phys. C **68**, (1995) 607; Phys. Lett. B **376**, (1996) 193.
- [6] M. Drees, M. Krämer, J. Zunft and P.M. Zerwas, Phys. Lett. B **306**, (1993) 371.
- [7] M. Krämer, Proceedings on Two-Photon Collisions at PHOTON '95, Sheffield, England (1995), 111.
- [8] LEP design report, vol I, The LEP Injector Chain, CERN-LEP-TH/83-29 (1983);
LEP design report, vol II, The LEP Main Ring, CERN-LEP-TH/84-01 (1984);
I. Wilson and H. Henke, The LEP Main Ring Accelerating Structure, CERN/89-09, CERN, 1989.
- [9] D. DeCamp *et al.*, Nucl. Inst. and Meth. A **294** (1990) 127.
- [10] P. Aarnio *et al.*, Nucl. Inst. and Meth. A **303** (1991) 233.
- [11] B. Adeva *et al.*, Nucl. Inst. and Meth. A **289** (1990) 35;
O. Adriani *et al.*, Phys. Rep. **236** (1993) 1;
M. Acciari *et al.*, Nucl. Inst. and Meth. A **351** (1994) 300;
M. Acciari *et al.*, Nucl. Inst. and Meth. A **360** (1995) 103.
- [12] K. Ahmet *et al.*, Nucl. Inst. and Meth. A **305** (1991) 275.
- [13] H. Akbari *et al.*, Nucl. Inst. and Meth. A **315** (1992) 161;
G.M. Viertel *et al.*, Nucl. Inst. and Meth. A **323** (1992) 399;
F. Beissel *et al.*, Nucl. Inst. and Meth. A **332** (1993) 33.
- [14] A. Arefiev *et al.*, Nucl. Inst. and Meth. A **275** (1989) 71;
A. Arefiev *et al.*, Nucl. Inst. and Meth. A **285** (1989) 403;

- O. Adriani *et al.*, Nucl. Inst. and Meth. A **302** (1991) 53.
- [15] B. Adeva *et al.*, Nucl. Inst. and Meth. A **277** (1989) 187;
B. Adeva *et al.*, Nucl. Inst. and Meth. A **323** (1992) 109.
- [16] A. Adam *et al.*, Nucl. Inst. and Meth. A **383** (1996) 342.
- [17] I.C. Brock *et al.*, Nucl. Inst. and Meth. A **381** (1996) 236.
- [18] P. Bagnaia *et al.*, Nucl. Inst. and Meth. A **317** (1992) 463;
P. Bagnaia *et al.*, Nucl. Inst. and Meth. A **324** (1993) 101.
- [19] R. Bizzari *et al.*, Nucl. Inst. and Meth. A **283** (1989) 799;
P. Bagnaia *et al.*, Nucl. Inst. and Meth. A **324** (1993) 101;
P. Bagnaia *et al.*, Nucl. Inst. and Meth. A **344** (1994) 212.
- [20] G. Carlino *et al.*, L3 Internal Note **1951**, (1997).
- [21] P. Béné *et al.*, Nucl. Inst. and Meth. A **306** (1991) 150.
- [22] Y. Bertsch *et al.*, Nucl. Inst. and Meth. A **340** (1994) 309;
S.P. Beingsner *et al.*, Nucl. Inst. and Meth. A **340** (1994) 322.
- [23] C. Diobisi *et al.*, Nucl. Inst. and Meth. A **336** (1993) 78.
- [24] S. Banerjee and F. Bruyant, L3 Internal Note **748**, 1989.
- [25] T. Sjöstrand, Comput. Phys. Commun. **82**, (1994) 74.
- [26] V. M. Budnev *et al.*, Phys. Rep. **15** (1975) 181.
- [27] J.A.M. Vermaseren, Nucl. Phys. B **229**, (1983) 347.
- [28] S. Jadach, B.F.L. Ward and Z. Was, Comput. Phys. Commun. **79**,
(1994) 503.
- [29] M. Skrzypek, S. Jadach, W. Placzek and Z. Was, Comput. Phys.
Commun. **94**, (1996) 216.
- [30] R. Burn *et al.*, GEANT3 User Guide, CERN-DD-EE/84-1.
- [31] B. Adeva *et al.*, Nucl. Inst. and Meth. A **289** (1990) 35.
- [32] M. Acciarri *et al.*, Phys. Lett. B **453**, (1999) 83.
- [33] JADE Collab., B. Bethke *et al.*, Phys. Lett. B **213**, (1988) 235.

- [34] R. McNeil, PHOTON 99 - International Conference on the Structure and Interactions of the Photon, Freiburg, Germany, May 23-26 1999.
- [35] S. Saremi, PHOTON 2000 - International Conference on the Structure and Interactions of the Photon, Ambleside, England, August 26-31 2000.
- [36] L3 Collab., M. Acciarri *et al.*, Phys. Lett. B **503**, (2001) 10.
- [37] A. Stone, Measurement of inclusive charm production in two-photon collisions at LEP, Thesis submitted to Louisiana State University, 1999.
- [38] JADE Collab., W. Bartel *et al.*, Phys. Lett. B **184**, (1987) 288.
- [39] TPC/Two-Gamma Collab., M. Alston-Garnjost *et al.*, Phys. Lett. B **252**, (1990) 499.
- [40] TASSO Collab., W. Braunschweig *et al.*, Z. Phys. C **47**, (1990) 499.
- [41] TOPAZ Collab., R. Enomoto *et al.*, Phys. Lett. B **328**, (1994) 535, Phys. Rev. D **50**, (1994) 1879, Phys. Lett. B **341**, (1994) 99, Phys. Lett. B **341**, (1994) 238.
- [42] VENUS Collab., S. Uehara *et al.*, Z. Phys. C **63**, (1994) 213.
- [43] AMY Collab., T. Aso *et al.*, Phys. Lett. B **363**, (1995) 249, Phys. Lett. B **381**, (1996) 372.
- [44] ALEPH Collab., D. Buskulic *et al.*, Phys. Lett. B **255**, (1995) 595.
- [45] L3 Collab., M. Acciarri *et al.*, Phys. Lett. B **467**, (1999) 137.
- [46] International Study Group Progress Report On Linear Collider Development, SLAC-Report-559, (2000).
- [47] U. Uwer, L3 Internal Note **2003**, (1996).

APPENDIX A

ADDENDUM TO QCD

A.1 Altarelli-Parisi Equation

The Altarelli-Parisi equations allow us to calculate how the parton distributions inside a hadron, $q_i(x, Q^2)$ and $g(x, Q^2)$, change with Q^2 , if they are specified at some starting value $Q^2 = Q_0^2$ ($Q^2 \gg \Lambda_{\text{QCD}}^2$). In these equations, x denotes the momentum fraction of the hadron carried by the parton. The most general form of Altarelli-Parisi equation for quark distributions is:

$$\frac{\partial q_i(x, Q^2)}{\partial \ln Q^2} = \frac{\alpha_s(Q^2)}{2\pi} \int_x^1 \frac{dy}{y} [q_i(y, Q^2) P_{qq}\left(\frac{x}{y}\right) + g(y, Q^2) P_{qg}\left(\frac{x}{y}\right)] \quad (\text{A.1})$$

In this equation, the first term in the integrand corresponds to the case where a quark emits a gluon and becomes a quark with momentum reduced by a fraction x/y . The second term describes the possibility of quark production with momentum fraction x due to $q\bar{q}$ production by a parent gluon with momentum fraction y ($y > x$).

The Altarelli-Parisi equation for the gluon distribution can be expressed as follows:

$$\frac{\partial g(x, Q^2)}{\partial \ln Q^2} = \frac{\alpha_s(Q^2)}{2\pi} \int_x^1 \frac{dy}{y} \left[\sum_i^{2N_f} q_i(y, Q^2) P_{gq}\left(\frac{x}{y}\right) + g(y, Q^2) P_{gg}\left(\frac{x}{y}\right) \right] \quad (\text{A.2})$$

In this equation, the sum $i = 1, \dots, 2N_f$ runs over quark and antiquarks of all flavors. Equations A.1 and A.2 both use special functions P_{ij} (P_{qq}, P_{qg}, \dots), which represent the probabilities for $i \rightarrow j$ transitions. These are called splitting functions.

A.2 Splitting Functions

The splitting functions in terms of $z = x/y$ are defined as follows:

$$P_{qq}(z) = \frac{4}{3} \left(\frac{1+z^2}{1-z} \right) \quad (\text{A.3})$$

$$P_{qg}(z) = \frac{1}{2} [z^2 + (1-z)^2] \quad (\text{A.4})$$

$$P_{gq}(z) = \frac{4}{3} \frac{1 + (1-z)^2}{z} \quad (\text{A.5})$$

$$P_{gg}(z) = 6 \left(\frac{1-z}{z} + \frac{z}{1-z} + z(1-z) \right) \quad (\text{A.6})$$

In addition, the following properties can be attributed to the splitting functions due to charge conjugation:

$$P_{\bar{q}g}(z) = P_{qg}(z) \quad (\text{A.7})$$

$$P_{g\bar{q}}(z) = P_{gq}(z) \quad (\text{A.8})$$

Momentum conservation at the splitting vertex yields:

$$P_{qg}(z) = P_{qg}(1-z) \quad (\text{A.9})$$

$$P_{gg}(z) = P_{gg}(1-z) \quad (\text{A.10})$$

$$P_{gq}(z) = P_{gq}(1-z) \quad (\text{A.11})$$

A.3 $\{\}_+$ Functions

$\{\}_+$ or “+ functions” are distributions that are well behaved only when convoluted with a smooth function that vanishes sufficiently rapidly as $x \rightarrow 1$.

They have the following property:

$$\int_0^1 \{F(x)\}_+ dx = 0 \quad (\text{A.12})$$

Analytically these functions can be expressed as:

$$\{F(x)\}_+ = \lim_{\beta \rightarrow 0} \{F(x)\theta(1-x-\beta) - \delta(1-x-\beta) \int_0^{1-\beta} F(y)dy\} \quad (\text{A.13})$$

where

$$\theta(y) = 0 \text{ for } y \leq 0 \quad (\text{A.14})$$

$$\theta(y) = 1 \text{ for } y > 0 \quad (\text{A.15})$$

Two often used “+ functions” are:

$$\left\{\frac{1}{1-x}\right\}_+ \equiv \lim_{\beta \rightarrow 0} \left\{\frac{1}{1-x}\theta(1-x-\beta) + \log(\beta)\delta(1-x-\beta)\right\} \quad (\text{A.16})$$

$$\left\{\frac{\log(1-x)}{1-x}\right\}_+ \equiv \lim_{\beta \rightarrow 0} \left\{\frac{\log(1-x)}{1-x}\theta(1-x-\beta) + \frac{1}{2}\log^2(\beta)\delta(1-x-\beta)\right\} \quad (\text{A.17})$$

APPENDIX B

SCINTILLATORS

B.1 Introduction

The scintillation counter system [47] of the L3 detector is depicted in Figure 3.9. This subdetector is used mainly for timing and trigger purposes. The time is measured with respect to the beam crossing time. This subdetector is also used to reject cosmic ray muons.

Since 1995, Louisiana State University has been involved with monitoring and calibrating the scintillation counters. The task was first taken by Prof. Roger McNeil while he was at CERN. The responsibility was passed over to Alan Stone and later on to Sepehr Saremi. Experimentation at different energies and the aging of detector materials (or electronics), requires the detector to be calibrated at some time intervals. At L3, all the subdetectors are calibrated at the beginning of each run period¹. At the beginning of each run period the LEP collider provides 2.5 pb^{-1} of data taken at the Z^0 resonance. The high cross section for lepton pair and quark pair production at the Z^0 resonance make it possible to obtain a large sample of data in a short time (a week) to calibrate detectors. The four LEP experiment use this data to calibrate their different subdetectors.

B.2 Barrel and Endcap Counters

The scintillation counter system at L3 consists of a barrel and endcap region. The barrel system is made of 30 plastic scintillator paddles with a length of 2.9 m and a thickness of 1 cm. Both counter ends are connected by

¹The run periods refer to the year of the data taking.

a light-guide to a photo-multiplier tube (PMT). To allow high amplification inside the magnetic field of 0.5 T, Hamamatsu R2490 PMT's are used.

The barrel counters are located between the barrel part of BGO and HCAL. In the r - z plane the counters follow the shape of the HCAL. The counters have a radial distance from the beam axis of 885 mm for $|z| < 800$ mm and 979 mm for $|z| > 1000$ mm. The polar angle coverage of the barrel is $34^\circ < \theta < 146^\circ$ ($|\cos \theta| < 0.83$). In the $r - \phi$ plane, the barrel counters are grouped in pairs. They follow the 16-fold symmetry of the HCAL. Due to the horizontal support rails for the BGO, two counters, 17 and 32, are missing. In order to compensate for this loss, the adjacent counters, 18 and 31, are about 50% larger.

The endcap system consists of two sets of 16 counters located between the BGO and HCAL endcaps. Each counter is made out of 3 plates of 5 mm thick plastic scintillator. The light of each plate is collected by 10 wavelength shifting fibers. There are a total of 30 fibers from each counter that are fed into an optical connector. A flexible light guide connects the counters to PMT's, which are situated outside the HCAL. The counters have an inner (outer) radius of 230 (768) mm. They are screwed against the outer shielding of the BGO endcaps. The middle of the second scintillator plate is at a distance of $z = \pm 1132.5$ mm from the interaction point. The polar angle coverage of the endcap system is $11.5^\circ < \theta < 34.1^\circ$ ($0.83 < |\cos \theta| < 0.98$).

B.3 Calibration

B.3.1 Calibration Events

The calibration is performed by selecting two track events. These are

mostly Bhabha and di-muon events with back-to-back tracks. We select tracks that can penetrate through the BGO and make a scintillator hit. Therefore, the tracks are required to meet the following criteria:

- The track has to have at least 5 hits in the TEC. This loose cut will allow the low angle tracks to be included in the data sample. However, a track with less than five hits will have poorly measured momentum and position.
- The distance of closest approach of the track to the collision point in the r - ϕ plane (DCA) must be less than 2 mm. This cut will ensure that the track has originated in the interaction point and thus can reject cosmic ray muons.
- The charged particle should deposit at least 100 MeV in the BGO. A much lower energy can be attributed to noise in the BGO.
- The track should have $|p| > 300$ MeV. This is the least energy that a minimum ionizing particle (MIP) like muon should have in order to penetrate the BGO.
- The track in TEC and the cluster in BGO should be matched by requiring $|\Delta\phi_{matched}^{TEC-BGO}| < 50$ mrad.

For the calibration process we require the BGO cluster to have $|\cos\theta| < 0.83$ for the barrel and $|\cos\theta| > 0.83$ for the endcap.

B.3.2 Barrel

The signals from the scintillator PMT are input to Time-to-Digital Converters (TDC) and Analog-to-Digital Converters (ADC). The TDC recorded counts, N_{TDC} , can be transformed into time, t_{TDC} , by the following equation:

$$t_{TDC} = -C_{Conv}(N_{TDC} - N_{TDC}^0). \quad (\text{B.1})$$

where C_{Conv} and N_{TDC}^0 are the count-to-time conversion constant and the TDC offset respectively². Both are channel dependent calibration constants and may differ significantly for the different TDC channels. LEP operates in the two bunchlet mode while taking calibration data at the Z^0 resonance. Consequently, Equation B.1 can be applied to each bunchlet:

$$t_{TDC}^{(1)} = -C_{Conv}(N_{TDC}^{(1)} - N_{TDC}^0). \quad (\text{B.2})$$

$$t_{TDC}^{(2)} = -C_{Conv}(N_{TDC}^{(2)} - N_{TDC}^0). \quad (\text{B.3})$$

where the superscripts (1) and (2) refer to bunchlet 1 and bunchlet 2 for a given counter. After deriving the calibration constants, Equations B.2 and B.3 are used to calculate the time from the TDC counts. The timing resolution can be improved by correcting for the ADC pulse-height dependence (the time-slew effect):

$$t_{CTR} = t_{TDC} + \Delta t_{slew}. \quad (\text{B.4})$$

The time-slew correction depends on the recorded pulse-height, A , and is described by:

² C_{Conv} and N_{TDC}^0 are also called slope and offset respectively.

$$\Delta t_{slew} = a \left(\frac{A_0}{A-b} - 1 \right) \quad (\text{B.5})$$

where $a = 1.74$ ns, $A_0 = 1871$ ADC counts and $b = 629$ ADC counts. The two PMTs on both ends of each counter, are used to measure the time. These two values can be used to calculate the mean time:

$$t_{Ctr,mean} = \frac{(t_{Ctr}^P + t_{Ctr}^J)}{2} \quad (\text{B.6})$$

where P and J refer to PIT and JURA³. For a calibrated counter one expects $t_{Ctr,mean}$ measured for a muon generated by a beam interaction to be equal to the time-of-flight, t_{FL} . A corrected time can be defined by:

$$t_{Cor} = t_{Ctr,mean} - t_{FL} \quad (\text{B.7})$$

and should be distributed around $t_{Cor} = 0$ ns. The width of this distribution is the time resolution of the counter. The corrected time is calculated automatically during event reconstruction for both bunchlets. With the passage of time there may be a shift to the distribution of the corrected time (Figure B.1).

This shift can be corrected through calibration. The calibration process ensures that the mean value of the corrected time distribution of each counter is at zero. At the beginning of each run period, the calibration constants from the previous run period are used for making the corrected time distributions of each counter. The corrected time distribution of each counter is fitted with a Gaussian curve. The width of the fit corresponds to the resolution of

³These are names that indicate the positive and negative z sides of the interaction point respectively.

All Barrel Count. Before 2000 Z Calib.

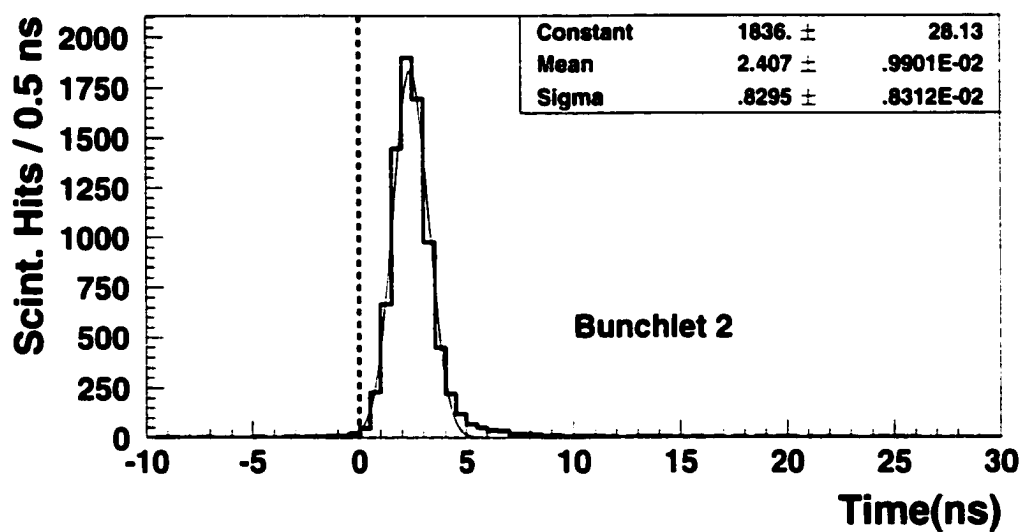
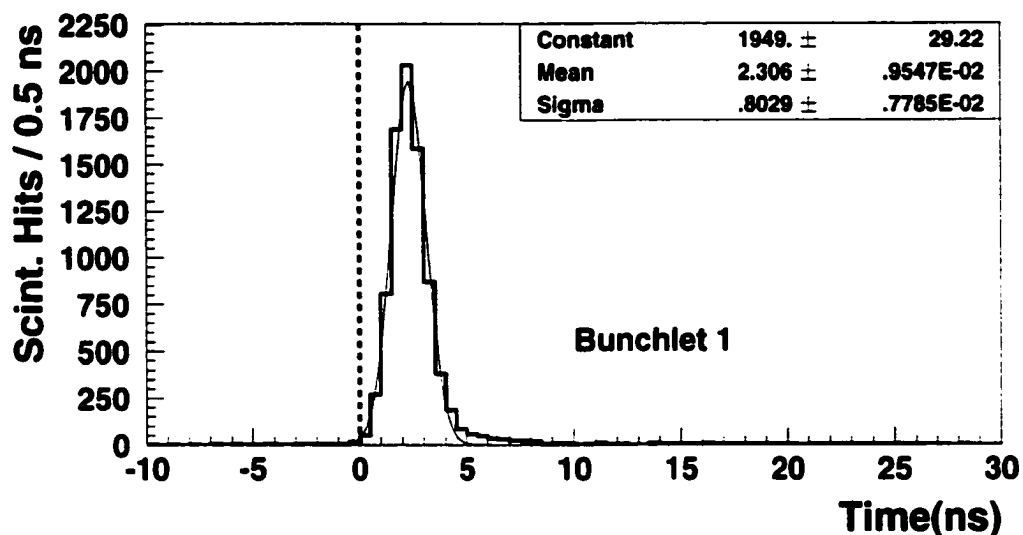


Figure B.1: The distribution of the corrected time for all the barrel counters before the calibration in year 2000. As can be seen the mean value of the distribution has clearly shifted from 0.

the counter. For each counter, the difference between the fitted mean and zero is considered the shift in the corrected time. By using these deviations and the measured TDC counts, $N_{TDC}^{(i)}$ (where i refers to bunchlet 1 or 2), a new set of calibration constants can be derived. These constants will be put in a temporary database. This new database will then be used to make new distributions for the corrected time. A new set of calibration constants can be extracted from these latest distributions. This process may be iterated for two or three times until a satisfactory set of distributions is obtained. At this point the calibration constants are put into the real database and will be used for the rest of the data taking period. Figure B.2 shows the distribution of the corrected time of all the barrel counters after the Z^0 calibration in year 2000. The time resolution of the barrel counters is around 800 ps.

B.3.3 Endcap

The time reconstruction for the endcap counters is done by using Equations B.2 and B.3. There is no time-slew correction for the endcap counters. Also there is no mean time calculation since each counter is connected to just one PMT.

The signal from an endcap counter has to pass through the wavelength shifter fibers and light guides before reaching the PMT. Consequently the signals from these counters are not as sharp in time as the ones from the barrel counters. The corrected time distribution for these counters has the shape of a Gaussian with a tail falling from the Gaussian curve. In order to calibrate the endcap counters their corrected time distribution has to be fitted with a convolution of a Gaussian and an exponential function. The

All Barrel Count. After 2000 Z Calib.

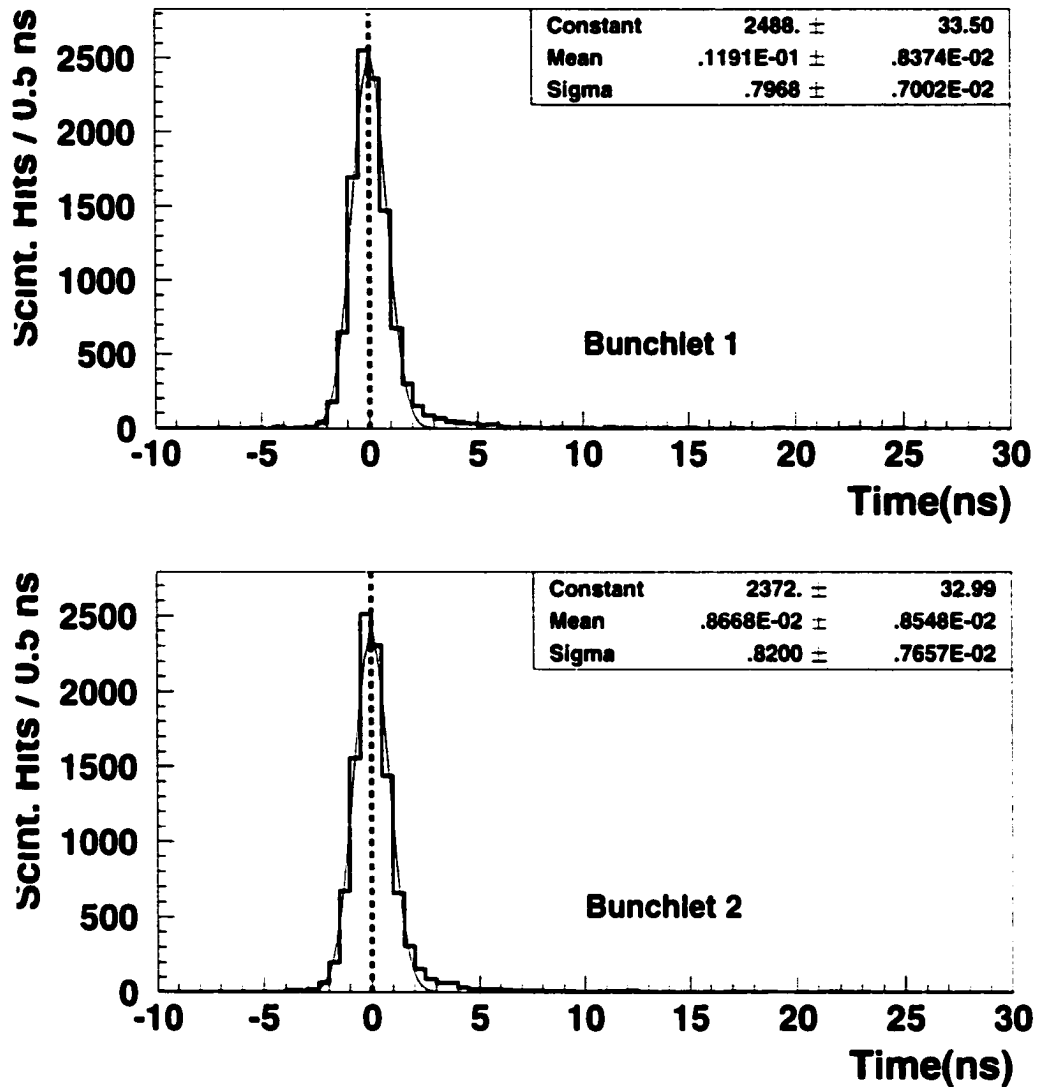


Figure B.2: The distribution of the corrected time for all the barrel counters after the calibration. After the calibration, the corrected time distribution is centered at 0.

new calibration constants will be derived as in the case of the barrel counters. Figures B.3 and B.4 depict the corrected time distribution of all the endcap counters before and after the year 2000 calibration respectively.

B.4 Efficiency

It is very important to keep track and monitor the efficiency of the scintillator counters throughout different run periods. In general, the efficiency of each counter represents the percentage of the charged tracks for which the counter will produce a signal. Thus, the efficiency of each counter can be calculated by knowing the numbers of charged tracks that have passed through that counter and the ones expected to pass. A possible approach is to look for di-muon events with a muon in the muon chamber. However, this restriction will reduce the data statistics. Another approach is to look for MIP's that have certainly passed through the counters. This can be done by requiring a minimum deposited energy in the HCAL. This is because scintillator counters lay between BGO and HCAL. In addition to the cuts in the previous section the following cuts can be made to select a data sample for the efficiency studies:

- $|p| > 1.0$ GeV. This is to ensure the particle is minimum ionizing and has enough momentum to penetrate through the BGO.
- $E_{bump} < 500$ MeV. A MIP will deposit an average of 250-300 MeV in the BGO. This cut rejects the electrons which almost never penetrate through BGO.
- $E_{hcal} > 100$ MeV. E_{hcal} is the energy deposit in HCAL within a 7° cone

All Endcap Count. Before 2000 Z Calib.

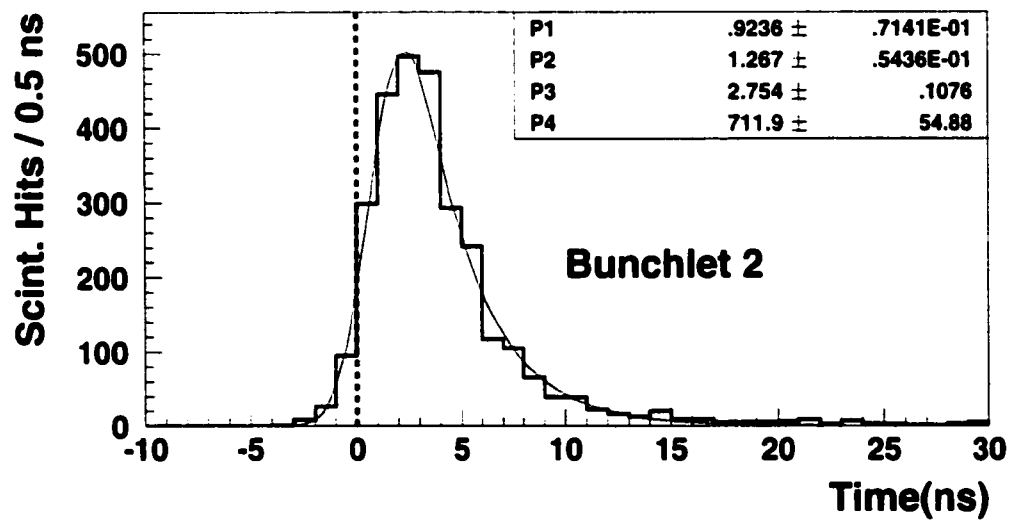
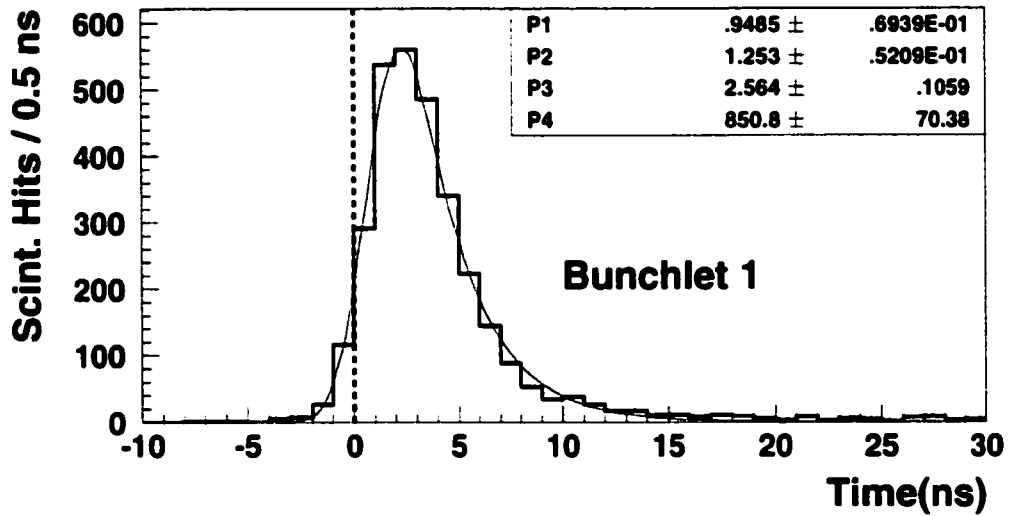


Figure B.3: The corrected time distribution of all the endcap counters before the year 2000 calibration. A time shift is clearly visible.

All Endcap Count. After 2000 Z Calib.

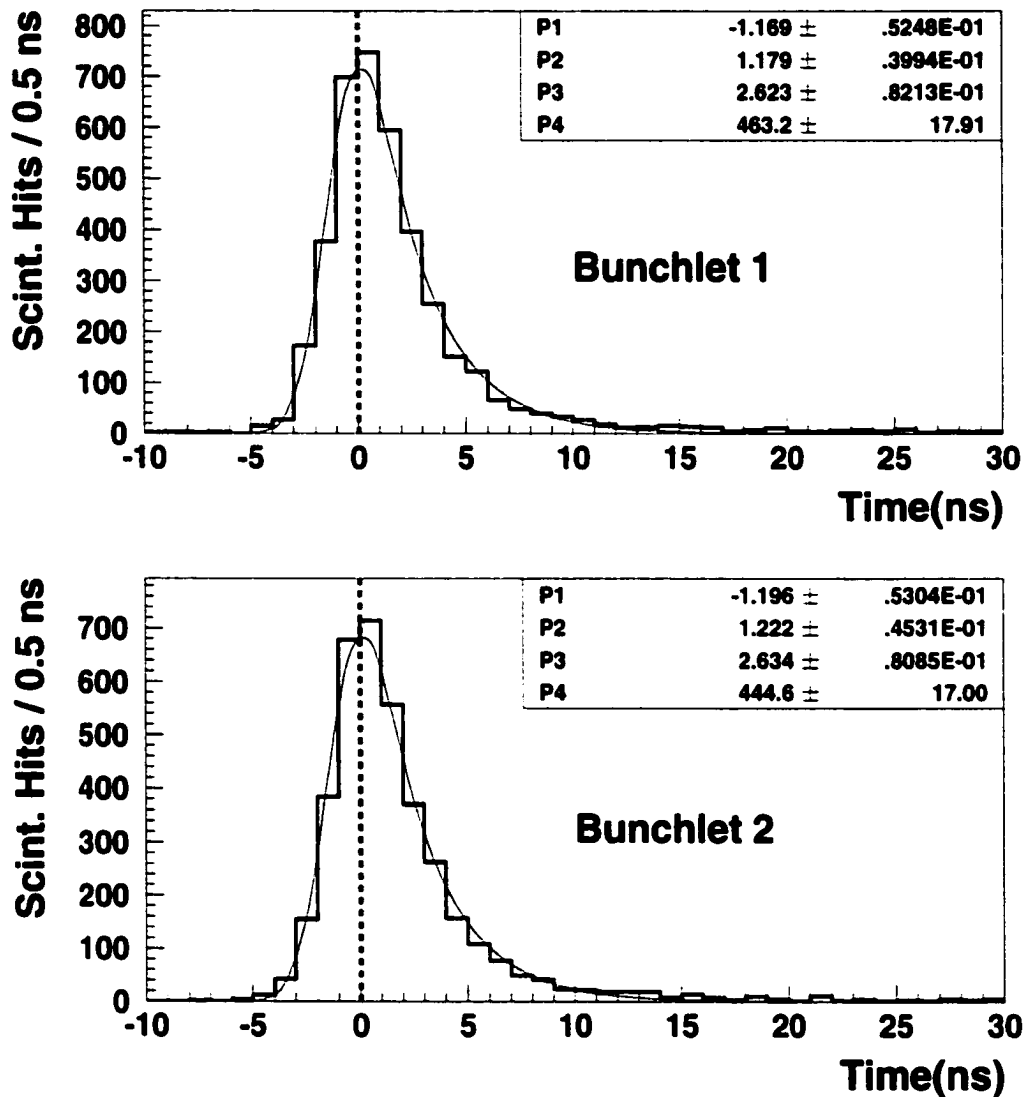


Figure B.4: This plot shows the corrected time distribution of all the endcap counters after the year 2000 calibration. The calibration has shifted the mean of the distribution around 0.

around the particle. This cut is imposed to exclude the noise in HCAL. Also, some energy needs to be detected to correct for some acceptance loss due to cracks between the counters.

The efficiency of each counter is the ratio of the number of hits detected in the counter to the number of BGO clusters matched to that counter. Figure B.5 shows the efficiencies of two typical barrel counters for different periods.

The efficiencies have remained almost constant throughout the length of the experiment. The only major change for efficiencies has happened for barrel counters 24 and 25. In 1991, there was a leak of the BGO cooling liquid. The silicon oil crept between the counter wrapping and the plastic scintillator and modified the reflection index of the surface. Figure B.6 shows the efficiencies for counters 24 and 25 for the period of 1995-2000.

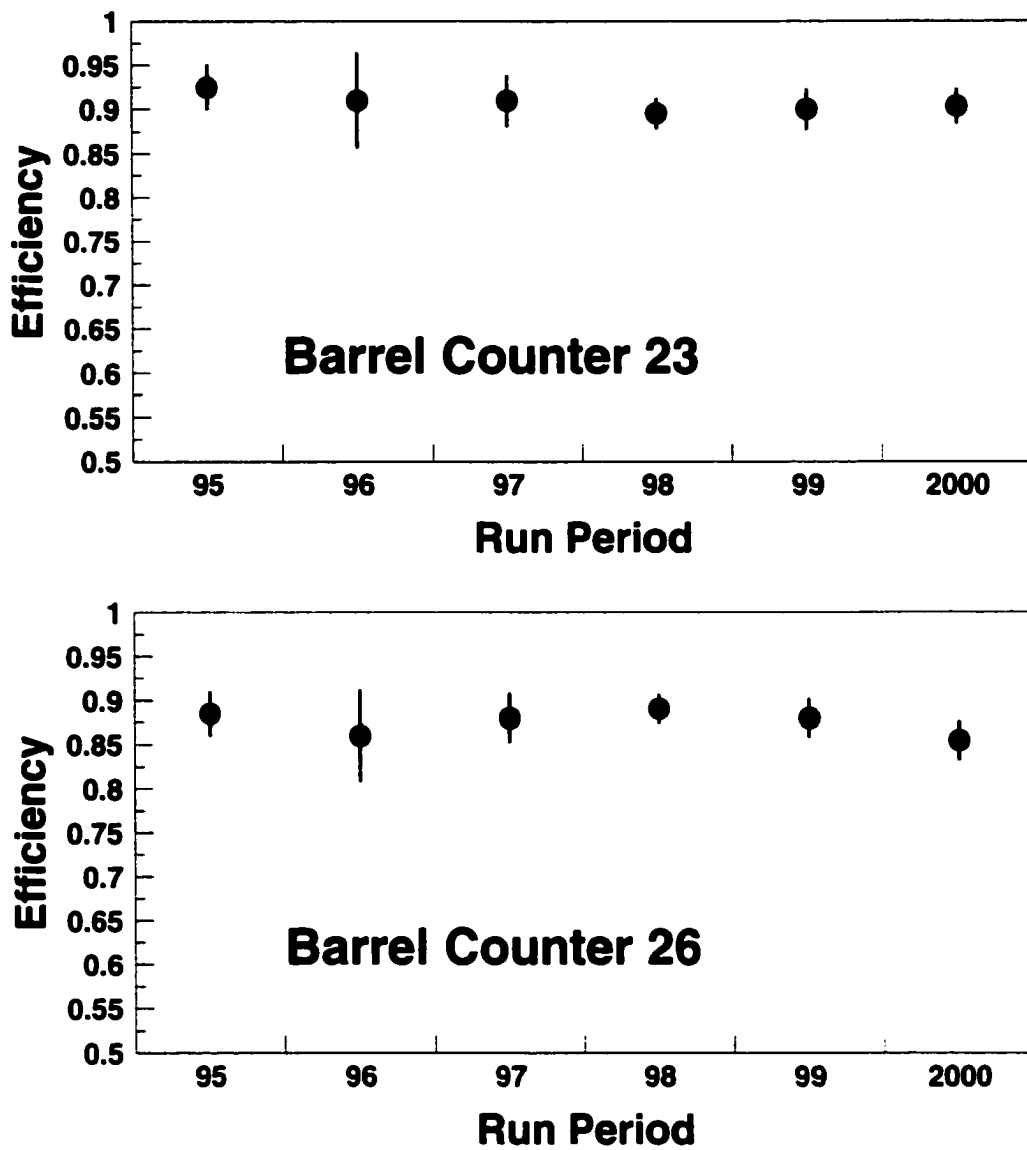


Figure B.5: Efficiencies of two typical barrel counters, 23 and 26.

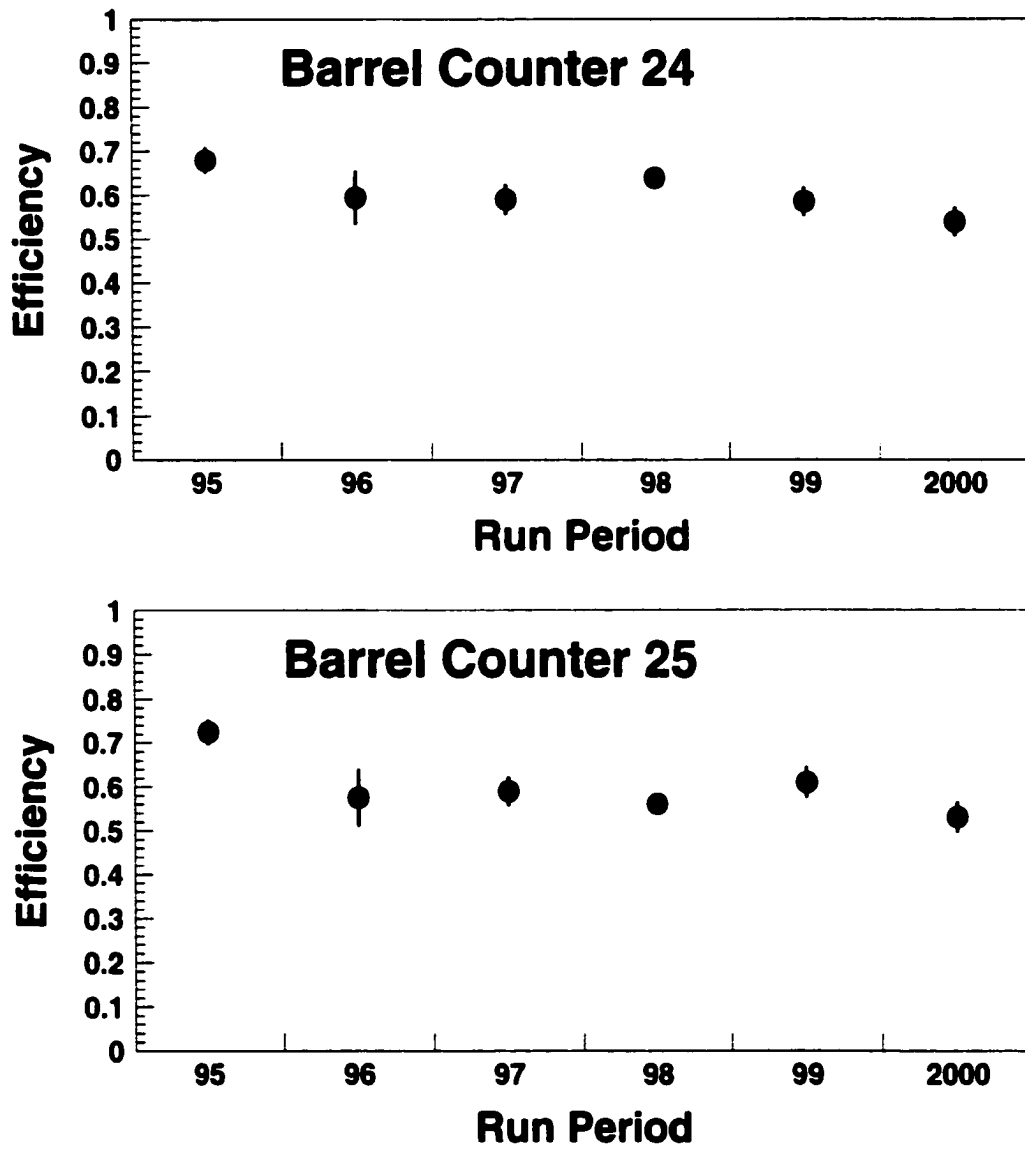


Figure B.6: Efficiencies of barrel counters 24 and 25 from 1995 to 2000.

THE L3 COLLABORATION

P.Achard,²⁰ O.Adriani,¹⁷ M.Aguilar-Benitez,²⁴ J.Alcaraz,^{24,18} G.Alemanni,²² J.Allaby,¹⁸ A.Aloisio,²⁸
 M.G.Alvigni,²⁸ H.Anderhub,⁴⁷ V.P.Andreev,^{6,33} F.Anselmo,⁹ A.Arefiev,²⁷ T.Azmoon,³ T.Aziz,^{10,18}
 P.Bagnaia,³⁸ A.Bajo,²⁴ G.Baksay,¹⁶ L.Baksay,²⁵ S.V.Baldew,² S.Banerjee,¹⁰ Sw.Banerjee,⁴
 A.Barczyk,^{47,45} R.Barillère,¹⁸ P.Bartalini,²² M.Basile,⁹ N.Batalova,⁴⁴ R.Battiston,³² A.Bay,²²
 F.Becattini,¹⁷ U.Becker,¹⁴ F.Behner,⁴⁷ L.Bellucci,¹⁷ R.Berbeco,³ J.Berdugo,²⁴ P.Berges,¹⁴
 B.Bertucci,³² B.L.Betev,⁴⁷ M.Biasini,³² M.Biglietti,²⁸ A.Biland,⁴⁷ J.J.Blaising,⁴ S.C.Blyth,³⁴
 G.J.Bobbink,² A.Böhm,¹ L.Boldizsar,¹³ B.Borgia,³⁸ S.Bottai,¹⁷ D.Bourilkov,⁴⁷ M.Bourquin,²⁰
 S.Braccini,²⁰ J.G.Branson,⁴⁰ F.Brochu,⁴ A.Buijs,⁴³ J.D.Burger,¹⁴ W.J.Burger,³² X.D.Cai,¹⁴
 M.Capell,¹⁴ G.Cara Romeo,⁹ G.Carlino,²⁸ A.Cartacci,¹⁷ J.Casaus,²⁴ F.Cavallari,³⁸ N.Cavallo,³⁵
 C.Cecchi,³² M.Cerrada,²⁴ M.Chamizo,²⁰ Y.H.Chang,⁴⁹ M.Chemarin,²³ A.Chen,⁴⁹ G.Chen,⁷
 G.M.Chen,⁷ H.F.Chen,²¹ H.S.Chen,⁷ G.Chiefari,²⁸ L.Cifarelli,³⁹ F.Cindolo,⁹ I.Clare,¹⁴ R.Clare,³⁷
 G.Coignet,⁴ N.Colino,²⁴ S.Costantini,³⁸ B.de la Cruz,²⁴ S.Cucciarelli,³² J.A.van Dalen,³⁰
 R.de Asmundis,²⁸ P.Déglon,²⁰ J.Debreczeni,¹³ A.Degré,⁴ K.Deiters,⁴⁵ D.della Volpe,²⁸ E.Delmeire,²⁰
 P.Denes,³⁶ F.DeNotaristefani,³⁸ A.De Salvo,⁴⁷ M.Diemoz,³⁸ M.Dierckxsens,² D.van Dierendonck,²
 C.Dionisi,³⁸ M.Dittmar,^{47,18} A.Doria,²⁸ M.T.Dova,^{11,5} D.Duchesneau,¹ P.Duiniker,² B.Echenard,²⁰
 A.Eline,¹⁸ H.El Mamouni,²³ A.Engler,³⁴ F.J.Eppling,¹⁴ A.Ewers,¹ P.Extermann,²⁰ M.A.Falagan,²⁴
 S.Falciano,³⁸ A.Favara,³¹ J.Fay,²³ O.Fedin,³³ M.Felcini,⁴⁷ T.Ferguson,³⁴ H.Fesefeldt,¹ E.Fiandrini,³²
 J.H.Field,²⁰ F.Filthaut,³⁰ P.H.Fisher,¹⁴ W.Fisher,³⁶ I.Fisk,⁴⁰ G.Forconi,¹⁴ K.Freudenreich,⁴⁷
 C.Furetta,²⁶ Yu.Galaktionov,^{27,14} S.N.Ganguli,¹⁰ P.Garcia-Abia,^{5,18} M.Gataullin,³¹ S.Gentile,³⁸
 S.Giagu,³⁸ Z.F.Gong,²¹ G.Grenier,²³ O.Grimm,⁴⁷ M.W.Gruenewald,^{8,1} M.Guida,³⁹ R.van Gulik,²
 V.K.Gupta,³⁶ A.Gurtu,¹⁰ L.J.Gutay,⁴⁴ D.Haas,⁵ D.Hatzifotiadou,⁹ T.Hebbeker,^{8,1} A.Hervé,¹⁸
 J.Hirschfelder,³⁴ H.Hofer,⁴⁷ M.Hohlmann,²⁵ G.Holzner,⁴⁷ S.R.Hou,⁴⁹ Y.Hu,³⁰ B.N.Jin,⁷ L.W.Jones,³
 P.de Jong,² I.Josa-Mutuberría,²⁴ D.Käfer,¹ M.Kaur,¹⁵ M.N.Kienzle-Focacci,²⁰ J.K.Kim,⁴² J.Kirkby,¹⁸
 W.Kittel,³⁰ A.Klimentov,^{14,27} A.C.König,³⁰ M.Kopal,⁴⁴ V.Koutsenko,^{14,27} M.Kräber,⁴⁷
 R.W.Kraemer,³⁴ W.Krenz,¹ A.Krüger,⁴⁶ A.Kunin,¹⁴ P.Ladron de Guevara,²⁴ I.Laktineh,²³ G.Landi,¹⁷
 M.Lebeau,¹⁸ A.Lebedev,¹⁴ P.Lebrun,²³ P.Lecomte,⁴⁷ P.Lecoq,¹⁸ P.Le Coultre,⁴⁷ H.J.Lee,⁸
 J.M.Le Goff,¹⁵ R.Leiste,⁴⁶ P.Levtchenko,³³ C.Li,²¹ S.Likhoded,⁴⁶ C.H.Lin,⁴⁹ W.T.Lin,⁴⁹ F.L.Linde,²
 L.Lista,²⁸ Z.A.Liu,⁷ W.Lohmann,⁴⁶ E.Longo,³⁸ Y.S.Lu,⁷ K.Lübelsmeyer,¹ C.Luci,³⁸ L.Luminari,³⁸
 W.Lustermann,⁴⁷ W.G.Ma,²¹ L.Malgeri,²⁰ A.Malinin,⁷ C.Maña,²⁴ D.Mangeol,³⁰ J.Mans,³⁶
 J.P.Martin,²³ F.Marzano,³⁸ K.Mazumdar,¹⁰ R.R.McNeil,⁶ S.Mele,^{18,28} L.Merola,²⁸ M.Meschini,¹⁷
 W.J.Metzger,³⁰ A.Mihul,¹² H.Milcent,¹⁸ G.Mirabelli,³⁸ J.Mnich,¹ G.B.Mohanty,¹⁰ G.S.Muanza,²³
 A.J.M.Muijs,² B.Musicar,⁴⁰ M.Musy,³⁸ S.Nagy,¹⁶ S.Natale,²⁰ M.Napolitano,²⁸ F.Nessi-Tedaldi,⁴⁷
 H.Newman,³¹ T.Niessen,¹ A.Nisati,³⁸ H.Nowak,⁴⁶ R.Ofierzynski,⁴⁷ G.Organtini,³⁸ C.Palomares,¹⁸
 D.Pandoulas,¹ P.Paolucci,²⁸ R.Paramatti,³⁸ G.Passaleva,¹⁷ S.Patricelli,²⁸ T.Paul,¹¹ M.Pauluzzi,³²
 C.Paus,¹⁴ F.Pauss,⁴⁷ M.Pedace,³⁸ S.Pensotti,²⁶ D.Perret-Gallix,⁴ B.Petersen,³⁰ D.Piccolo,²⁸
 F.Pierella,⁹ M.Pioppi,³² P.A.Piroué,³⁶ E.Pistoiesi,²⁶ V.Plyaskin,²⁷ M.Pohl,²⁰ V.Pojidaev,¹⁷ J.Pothier,¹⁸
 D.O.Prokofiev,⁴⁴ D.Prokofiev,³³ J.Quartieri,³⁹ G.Rahal-Callot,⁴⁷ M.A.Rahaman,¹⁰ P.Raics,¹⁶
 N.Raja,¹⁰ R.Ramelli,⁴⁷ P.G.Rancoita,²⁶ R.Ranieri,¹⁷ A.Raspereza,⁴⁶ P.Razis,²⁹ D.Ren,⁴⁷ M.Rescigno,³⁸
 S.Reucroft,¹¹ S.Riemann,⁴⁶ K.Riles,³ B.P.Roe,³ L.Romero,²⁴ A.Rosca,⁸ S.Rosier-Lees,⁴ S.Roth,¹
 C.Rosenbleck,¹ B.Roux,³⁰ J.A.Rubio,¹⁸ G.Ruggiero,¹⁷ H.Rykaczewski,⁴⁷ A.Sakharov,⁴⁷ S.Saremi,⁶
 S.Sarkar,³⁸ J.Salicio,¹⁸ E.Sanchez,²⁴ M.P.Sanders,³⁰ C.Schäfer,¹⁸ V.Schegelsky,³³ S.Schmidt-Kaerst,¹
 D.Schmitz,¹ H.Schopper,⁴⁸ D.J.Schotanus,³⁰ G.Schwering,¹ C.Sciacca,²⁸ L.Servoli,³² S.Shevchenko,³¹
 N.Shivarov,⁴¹ V.Shoutko,¹⁴ E.Shumilov,²⁷ A.Shvorob,³¹ T.Siedenburger,¹ D.Son,⁴² P.Spillantini,¹⁷
 M.Steuer,¹⁴ D.P.Stickland,³⁶ B.Stoyanov,⁴¹ A.Straessner,¹⁸ K.Sudhakar,¹⁰ G.Sultanov,³¹ L.Z.Sun,²¹
 S.Sushkov,⁸ H.Suter,⁴⁷ J.D.Swain,¹¹ Z.Szillasi,^{25,4} X.W.Tang,⁷ P.Tarjan,¹⁶ L.Tauscher,⁵ L.Taylor,¹¹
 B.Tellili,²³ D.Teyssier,²³ C.Timmermans,³⁰ Samuel C.C.Ting,¹⁴ S.M.Ting,¹⁴ S.C.Tonwar,^{10,18}
 J.Tóth,¹³ C.Tully,³⁶ K.L.Tung,⁷ J.Ulbricht,⁴⁷ E.Valente,³⁸ R.T.Van de Walle,³⁰ V.Veszpremi,²⁵
 G.Vesztergombi,¹³ I.Vetlitsky,²⁷ D.Vicinanza,³⁹ G.Viertel,⁴⁷ S.Villa,³⁷ M.Vivargent,⁴ S.Vlachos,⁵
 I.Vodopianov,³³ H.Vogel,³⁴ H.Vogt,⁴⁶ I.Vorobiev,^{34,27} A.A.Vorobyov,³³ M.Wadhwa,⁵ W.Wallraff,¹
 X.L.Wang,²¹ Z.M.Wang,²¹ M.Weber,¹ P.Wienemann,¹ H.Wilkens,³⁰ S.Wynhoff,³⁶ L.Xia,³¹ Z.Z.Xu,²¹
 J.Yamamoto,³ B.Z.Yang,²¹ C.G.Yang,⁷ H.J.Yang,³ M.Yang,⁷ S.C.Yeh,⁵⁰ An.Zalite,³³ Yu.Zalite,³³
 Z.P.Zhang,²¹ J.Zhao,²¹ G.Y.Zhu,⁷ R.Y.Zhu,³¹ H.L.Zhuang,⁷ A.Zichichi,^{9,18,19} G.Zilizi,^{25,4}

B.Zimmermann,⁴⁷ M.Zöller¹

- 1 I. Physikalisches Institut, RWTH, D-52056 Aachen, FRG⁵
- III. Physikalisches Institut, RWTH, D-52056 Aachen, FRG⁵
- 2 National Institute for High Energy Physics, NIKHEF, and University of Amsterdam, NL-1009 DB Amsterdam, The Netherlands
- 3 University of Michigan, Ann Arbor, MI 48109, USA
- 4 Laboratoire d'Annecy-le-Vieux de Physique des Particules, LAPP, IN2P3-CNRS, BP 110, F-74941 Annecy-le-Vieux CEDEX, France
- 5 Institute of Physics, University of Basel, CH-4056 Basel, Switzerland
- 6 Louisiana State University, Baton Rouge, LA 70803, USA
- 7 Institute of High Energy Physics, IHEP, 100039 Beijing, China^Δ
- 8 Humboldt University, D-10099 Berlin, FRG⁵
- 9 University of Bologna and INFN-Sezione di Bologna, I-40126 Bologna, Italy
- 10 Tata Institute of Fundamental Research, Mumbai (Bombay) 400 005, India
- 11 Northeastern University, Boston, MA 02115, USA
- 12 Institute of Atomic Physics and University of Bucharest, R-76900 Bucharest, Romania
- 13 Central Research Institute for Physics of the Hungarian Academy of Sciences, H-1525 Budapest 114, Hungary[†]
- 14 Massachusetts Institute of Technology, Cambridge, MA 02139, USA
- 15 Panjab University, Chandigarh 160 014, India.
- 16 KLTE-ATOMKI, H-4010 Debrecen, Hungary[†]
- 17 INFN Sezione di Firenze and University of Florence, I-50125 Florence, Italy
- 18 European Laboratory for Particle Physics, CERN, CH-1211 Geneva 23, Switzerland
- 19 World Laboratory, FBLJA Project, CH-1211 Geneva 23, Switzerland
- 20 University of Geneva, CH-1211 Geneva 4, Switzerland
- 21 Chinese University of Science and Technology, USTC, Hefei, Anhui 230 029, China^Δ
- 22 University of Lausanne, CH-1015 Lausanne, Switzerland
- 23 Institut de Physique Nucléaire de Lyon, IN2P3-CNRS, Université Claude Bernard, F-69622 Villeurbanne, France
- 24 Centro de Investigaciones Energéticas, Medioambientales y Tecnológicas, CIEMAT, E-28040 Madrid, Spain[‡]
- 25 Florida Institute of Technology, Melbourne, FL 32901, USA
- 26 INFN-Sezione di Milano, I-20133 Milan, Italy
- 27 Institute of Theoretical and Experimental Physics, ITEP, Moscow, Russia
- 28 INFN-Sezione di Napoli and University of Naples, I-80125 Naples, Italy
- 29 Department of Physics, University of Cyprus, Nicosia, Cyprus
- 30 University of Nijmegen and NIKHEF, NL-6525 ED Nijmegen, The Netherlands
- 31 California Institute of Technology, Pasadena, CA 91125, USA
- 32 INFN-Sezione di Perugia and Università Degli Studi di Perugia, I-06100 Perugia, Italy
- 33 Nuclear Physics Institute, St. Petersburg, Russia
- 34 Carnegie Mellon University, Pittsburgh, PA 15213, USA
- 35 INFN-Sezione di Napoli and University of Potenza, I-85100 Potenza, Italy
- 36 Princeton University, Princeton, NJ 08544, USA
- 37 University of California, Riverside, CA 92521, USA
- 38 INFN-Sezione di Roma and University of Rome, "La Sapienza", I-00185 Rome, Italy
- 39 University and INFN, Salerno, I-84100 Salerno, Italy
- 40 University of California, San Diego, CA 92093, USA
- 41 Bulgarian Academy of Sciences, Central Lab. of Mechatronics and Instrumentation, BU-1113 Sofia, Bulgaria
- 42 The Center for High Energy Physics, Kyungpook National University, 702-701 Taegu, Republic of Korea
- 43 Utrecht University and NIKHEF, NL-3584 CB Utrecht, The Netherlands
- 44 Purdue University, West Lafayette, IN 47907, USA

- 45 Paul Scherrer Institut, PSI, CH-5232 Villigen, Switzerland
- 46 DESY, D-15738 Zeuthen, FRG
- 47 Eidgenössische Technische Hochschule, ETH Zürich, CH-8093 Zürich, Switzerland
- 48 University of Hamburg, D-22761 Hamburg, FRG
- 49 National Central University, Chung-Li, Taiwan, China
- 50 Department of Physics, National Tsing Hua University, Taiwan, China
- § Supported by the German Bundesministerium für Bildung, Wissenschaft, Forschung und Technologie
- ‡ Supported by the Hungarian OTKA fund under contract numbers T019181, F023259 and T024011.
- ¶ Also supported by the Hungarian OTKA fund under contract number T026178.
- › Supported also by the Comisión Interministerial de Ciencia y Tecnología.
- ‡ Also supported by CONICET and Universidad Nacional de La Plata, CC 67, 1900 La Plata, Argentina.
- △ Supported by the National Natural Science Foundation of China.

PUBLICATIONS

1. Measurement of triple gauge couplings of the W boson at LEP.
M. Acciarri *et al.* (L3 Collab.), Phys. Lett. B **467**, 171 (1999).
2. Single and multiphoton events with missing energy in e^+e^- collisions at $\sqrt{s}=189$ GeV.
M. Acciarri *et al.* (L3 Collab.), Phys. Lett. B **470**, 268 (1999).
3. Search for extra dimensions in boson and fermion pair production in e^+e^- interactions at LEP.
M. Acciarri *et al.* (L3 Collab.), Phys. Lett. B **470**, 281 (1999).
4. Search for scalar leptons in e^+e^- collisions at $\sqrt{s}=189$ GeV.
M. Acciarri *et al.* (L3 Collab.), Phys. Lett. B **471**, 280 (1999).
5. Search for scalar quarks in e^+e^- interactions at $\sqrt{s}=189$ GeV.
M. Acciarri *et al.* (L3 Collab.), Phys. Lett. B **471**, 308 (1999).
6. Search for neutral Higgs bosons of the minimal supersymmetric standard model in e^+e^- interactions at $\sqrt{s}=189$ GeV.
M. Acciarri *et al.* (L3 Collab.), Phys. Lett. B **471**, 321 (1999).
7. Search for charginos and neutralinos in e^+e^- collisions at $\sqrt{s}=189$ GeV.
M. Acciarri *et al.* (L3 Collab.), Phys. Lett. B **472**, 420 (2000).
8. Search for excited leptons at $\sqrt{s}=189$ GeV.
M. Acciarri *et al.* (L3 Collab.), Phys. Lett. B **473**, 177 (2000).
9. Direct observations of longitudinally polarized W^\pm bosons.
M. Acciarri *et al.* (L3 Collab.), Phys. Lett. B **474**, 194 (2000).
10. Hard photon production and tests of QED at LEP.
M. Acciarri *et al.* (L3 Collab.), Phys. Lett. B **475**, 198 (2000).
11. The $K_s^0 K_s^0$ final state in two photon collisions and glueball searches.
S. Saremi, Nucl. Phys. Proc. Suppl. **82**, 344 (2000).
12. Measurement of the running of the fine structure constant.
M. Acciarri *et al.* (L3 Collab.), Phys. Lett. B **476**, 40 (2000).
13. Measurement of the probability of gluon splitting into charmed quarks in hadronic Z decays.
M. Acciarri *et al.* (L3 Collab.), Phys. Lett. B **476**, 243 (2000).
14. Measurement of the $e^+e^- \rightarrow Z\gamma\gamma$ cross section and determination of quartic gauge boson couplings at LEP.

- M. Acciarri *et al.* (L3 Collab.), Phys. Lett. B **478**, 39 (2000).
15. Measurement of the lifetime of the τ lepton.
M. Acciarri *et al.* (L3 Collab.), Phys. Lett. B **479**, 67 (2000).
 16. Inclusive Σ^+ and Σ^0 production in hadronic Z decays.
M. Acciarri *et al.* (L3 Collab.), Phys. Lett. B **479**, 79 (2000).
 17. Measurement of hadron and lepton pair production at $130 < \sqrt{s} < 189$ GeV at LEP.
M. Acciarri *et al.* (L3 Collab.), Phys. Lett. B **479**, 101 (2000).
 18. Search for charginos with a small mass difference with the lightest supersymmetric particle at $\sqrt{s}=189$ GeV.
M. Acciarri *et al.* (L3 Collab.), Phys. Lett. B **482**, 31 (2000).
 19. Measurements of cross sections and forward backward asymmetries at the Z resonance and determination of electroweak parameters.
M. Acciarri *et al.* (L3 Collab.), Eur. Phys. J. C **16**, 1 (2000).
 20. Measurement of the photon structure function at high Q^2 at LEP.
M. Acciarri *et al.* (L3 Collab.), Phys. Lett. B **483**, 373 (2000).
 21. Measurements of the $B - \bar{B}$ production cross section and forward backward asymmetry at center of mass energies above the Z pole at LEP.
M. Acciarri *et al.* (L3 Collab.), Phys. Lett. B **485**, 71 (2000).
 22. Search for an invisibly decaying Higgs boson in e^+e^- collisions at $\sqrt{s}=183-189$ GeV.
M. Acciarri *et al.* (L3 Collab.), Phys. Lett. B **485**, 85 (2000).
 23. Production of single W bosons at $\sqrt{s}=189$ GeV and measurement of $WW\gamma$ gauge couplings.
M. Acciarri *et al.* (L3 Collab.), Phys. Lett. B **487**, 229 (2000).
 24. Search for anomalous $ZZ\gamma$ and $Z\gamma\gamma$ couplings in the process $e^+e^- \rightarrow Z\gamma$ at LEP.
M. Acciarri *et al.* (L3 Collab.), Phys. Lett. B **489**, 55 (2000).
 25. QCD studies in e^+e^- annihilation from 30 GeV to 189 GeV.
M. Acciarri *et al.* (L3 Collab.), Phys. Lett. B **489**, 65 (2000).
 26. Search for manifestations of new physics in fermion pair production at LEP.
M. Acciarri *et al.* (L3 Collab.), Phys. Lett. B **489**, 81 (2000).
 27. Determination of γ/Z interference in e^+e^- annihilation at LEP.

- M. Acciarri *et al.* (L3 Collab.), Phys. Lett. B **489**, 93 (2000).
28. Search for anomalous couplings in the Higgs sector at LEP.
M. Acciarri *et al.* (L3 Collab.), Phys. Lett. B **489**, 102 (2000).
29. Search for a Higgs boson decaying into two photons in e^+e^- -interactions at $\sqrt{s}=189$ GeV.
M. Acciarri *et al.* (L3 Collab.), Phys. Lett. B **489**, 115 (2000).
30. Measurement of the $W^+W^-\gamma$ cross section and direct limits on anomalous quartic gauge boson couplings at LEP.
M. Acciarri *et al.* (L3 Collab.), Phys. Lett. B **490**, 187 (2000).
31. Measurement of Bose-Einstein correlations in $e^+e^- \rightarrow W^+W^-$ at $\sqrt{s}=189$ GeV.
M. Acciarri *et al.* (L3 Collab.), Phys. Lett. B **493**, 233 (2000).
32. Higgs candidates in e^+e^- -interactions at $\sqrt{s}=206.6$ GeV.
M. Acciarri *et al.* (L3 Collab.), Phys. Lett. B **495**, 18 (2000).
33. Measurement of the W pair production cross section and W decay branching fractions in e^+e^- -interactions at $\sqrt{s}=189$ GeV.
M. Acciarri *et al.* (L3 Collab.), Phys. Lett. B **496**, 19 (2000).
34. Search for charged Higgs bosons in e^+e^- -collisions at center of mass energies up to 202 GeV.
M. Acciarri *et al.* (L3 Collab.), Phys. Lett. B **496**, 34 (2000).
35. Study of Z boson pair production in e^+e^- -interactions at $\sqrt{s}=192$ -202 GeV.
M. Acciarri *et al.* (L3 Collab.), Phys. Lett. B **497**, 23 (2001).
36. Light resonances in $K_s^0 K^\pm \pi^\mp$ and $\eta \pi^+ \pi^-$ final states in $\gamma\gamma$ collisions at LEP.
M. Acciarri *et al.* (L3 Collab.), Phys. Lett. B **501**, 1 (2001).
37. Search for R-parity violating decays of supersymmetric particles in e^+e^- -collisions at $\sqrt{s}=189$ GeV.
M. Acciarri *et al.* (L3 Collab.), Eur. Phys. J. C **19**, 397 (2001).
38. $K_s^0 K_s^0$ final state in two photon collisions and implications for glueballs.
M. Acciarri *et al.* (L3 Collab.), Phys. Lett. B **501**, 173 (2001).
39. Search for excited leptons in e^+e^- -interactions at $\sqrt{s}=192$ GeV to 202 GeV.
M. Acciarri *et al.* (L3 Collab.), Phys. Lett. B **502**, 37 (2001).

40. Measurements of the cross sections for open charm and beauty production in $\gamma\gamma$ collisions at $\sqrt{s}=189\text{-}202$ GeV.
M. Acciarri *et al.* (L3 Collab.), Phys. Lett. B **503**, 10 (2001).
41. Search for neutral Higgs bosons of the minimal supersymmetric standard model in e^+e^- -interactions at $\sqrt{s}=192\text{-}202$ GeV.
M. Acciarri *et al.* (L3 Collab.), Phys. Lett. B **503**, 21 (2001).
42. Study of the $e^+e^- \rightarrow Z\gamma\gamma \rightarrow Q\bar{Q}\gamma\gamma$ process at LEP.
M. Acciarri *et al.* (L3 Collab.), Phys. Lett. B **505**, 47 (2001).
43. Measurement of the τ branching fractions into leptons.
M. Acciarri *et al.* (L3 Collab.), Phys. Lett. B **507**, 47 (2001).

VITA

Sepehr Saremi was born on August 26th, 1971 in Tehran, Iran. Sepehr started his primary school in Maryland where his father was a graduate student. After his father obtained his masters degree, Sepehr and his family moved back to Iran in 1979. Sepehr started his higher education at Tehran University majoring in electrical engineering. After completing two years of studies at Tehran University, Sepehr moved to the United States as a transfer student. He received a bachelor of science degree in physics from Louisiana State University in 1995.

Sepehr started his graduate studies in physics at Louisiana State University in 1995. He got a masters degree in physics in 1997. At that time he joined the experimental high energy physics group. He spent the summer of 1997 working in Los Alamos national laboratory. Afterwards, he started to work under the direction of Professor Roger McNeil. In summer of 1998, Sepehr moved to Switzerland to work on the L3 experiment at CERN (European Center for Nuclear and Particle Physics). Sepehr returned to Louisiana on January of 2001. He was awarded the degree of doctor of philosophy in physics in December of 2001.


DOCTORAL EXAMINATION AND DISSERTATION REPORT

Candidate: Sepehr Saremi

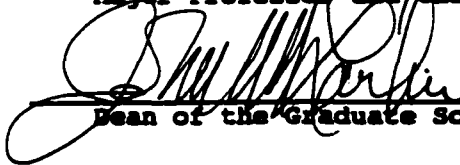
Major Field: Physics

Title of Dissertation: Measurement of Bottom Quark Production in Two-Photon Collisions

Approved:

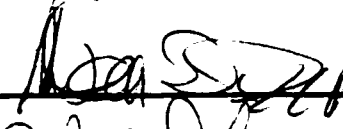


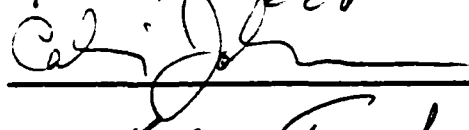
Major Professor and Chairman

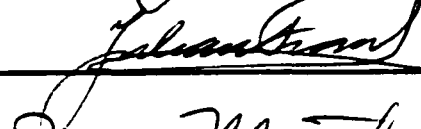


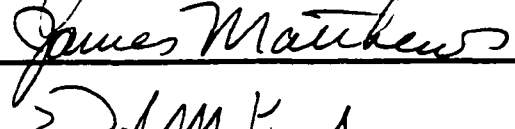
Dean of the Graduate School

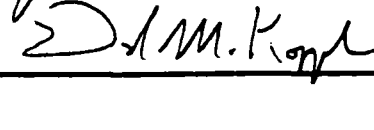
EXAMINING COMMITTEE:











Date of Examination:

October 30, 2001